CHEMICAL AND PHYSICAL PROPERTIES OF NANOMATERIALS FOR MODEL CATALYTIC SYSTEMS AND SMART POLYMER MEMBRANES

A Dissertation

by

STEPHANIE L. SKILES

Submitted to the Office of Graduate and Professional Studies of
Texas A&M University
in partial fulfillment of the requirements for the degree of

DOCTOR OF PHILOSOPHY

Chair of Committee,	James D. Batteas
Committee Members,	David E. Bergbreiter
	Christian Hilty
	Jaime C. Grunlan
Head of Department,	Francois Gabbai

December 2014

Major Subject: Chemistry

ABSTRACT

The increased development of surface science in the last half century has opened up new fields for exploration. Surfaces from the pristine to the complex can now be studied with relative ease. These developments along with the industrial society's desire for improvement have led to the study of smart materials and model systems.

Smart materials are designed to have a significant property change in response to a stimulus. Smart polymers can be synthesized that respond to a variety of stimuli including temperature, pH or light. The polymer responds to the stimulus by undergoing a transition that can affect its color, conductivity, shape, etc. Even slight changes in environment can induce large changes in the polymer. This work focuses on covalent layer-by-layer assembly grafts of the thermoresponsive polymer poly(*N*-isopropylacrylamide) and silica nanoparticles. When grafted to a surface, the system response to external stimuli inducing changes in topography and wettability. Utilizing nanoindentation the polymer graft's switching elastic modulus was probed as it was exposed to varying external stimuli. It was found that the modulus of the polymer graft changed an order of magnitude based on the polymer's history and current environment. Covalent layer-by-layer assembly additionally was used to functionalize porous substrates. The polymer's conformational change was leveraged in the development of an oil and water separation membrane capable of demulsification. The polymer's

transition to a non-soluble configuration blocked pore passageways, preventing the oil from permeating the substrate leading to a pure water filtrate.

Advances in surface science have pushed ahead the development of cheaper and better performing catalyst systems. These systems can be developed and tested using model catalyst systems. Herein, two model systems were investigated: a supported cobalt nanoparticle catalyst and a bimetallic palladium-copper system. In the cobalt system, the smallest particles are oxidized and deactivated during the Fischer-Tropsch reaction. In the bimetallic system, the electronic effect of metal alloying was investigated using X-ray photoelectron spectroscopy. The stable alloy was surface enriched with copper. The promotion effect of copper on palladium for the acetylene hydrogenation reaction was investigated. These model systems allow for the study of fundamental phenomena on a controlled surface.

DEDICATION

This is dedicated to my mom, dad, brother, family and friends for all of their love and support through the years.

A special dedication of Chapter VII is made to the late Dr. D. Wayne Goodman, my first graduate advisor.

ACKNOWLEDGEMENTS

I would like to acknowledge and thank my two graduate advisors, Dr. D. Wayne Goodman and Dr. James D. Batteas, for all the support and help they have given me during my years in graduate school at Texas A&M University. I would also like to take my past and present committee members: Dr. David E. Bergbreiter, Dr. Christian Hilty, Dr. Jaime C. Grunlan, Dr. Paul S. Cremer, and Dr. Daniel Shantz.

I joined the research group of Dr. D. Wayne Goodman upon entering graduate school in the Fall of 2009 until his untimely departure from this world. Dr. Goodman's enthusiasm and passion for science and life was evident and a constant driving force for improvement. I would like to thank my mentors and group members for helping me up the steep learning curve allowing me to be successful during my time in the Goodman labs. A special thanks is owed to Dr. Zhoujun (Joe) Wang, Dr. Qinlin Guo, Dr. Matthew Lundwall, Dr. Zhen Yan, and Dr. Ming-Shu Chen. Additionally, I would like to thank Amy Liu, the group's administrative assistant, for all hard work that made the group run smoothly.

I first worked for Dr. Batteas as an undergraduate research fellow with the National Science Foundation Research Experience for Undergraduates in the summer of 2008. I was welcomed back into the Batteas Research Labs in the summer of 2011, when circumstances required finding a new research home. A special thanks is owed to two

group member in particular, Brad Ewers and Carrie (Carpenter) Werke. Brad has been a continual source of ideas and advice, not to mention fabulous technical support. I count Carrie as great friend, who for the past three years has been my desk neighbor; therefore, putting up with my chattiness, happy dances, and grad school meltdowns. A great round of thanks is due to all of the Batteas group members I have over lapped with including: Dr. Arika Pravitasari, Dr. Chi-Yuan Chang, Captain Ainsley Allen, Dr. Ryan Jones, Dr. Albert Wan, Dr. Yang-Hsiang Chan, Dr. Jixin Chen, Dr. Amanda Schuckman, Dr. Agustin Diaz, Dr. Ayelet Vilan, Jessica Spear, Alison Pawlicki, Jiagang Ren, Cody Chalker, Megan Elinski, and Jennifer Belcik (administrative assistant).

A special thanks is due to my collaborator, Dr. David E. Bergbreiter. While I am not a member of his research group, he has opened up his lab for me to work in and office door for questions. I would like to thank the Bergbreiter group for helping this analytical chemist survive in an organic chemist's world. This group has adopted me in and been an unmeasurable help to my success, especially Dr. Kristine Tan, Dr. Tatyana Khamatnurova, Chih-Gang Chao, Peerada Samunual, Jakkrit Suriboot, and Mary Layne Harrell.

There are several members of the TAMU community that have been instrumental in my successes that have not been mentioned thus far. Thanks for the friendship over the years Keturah Odoi and Mavreen Rose. Thanks for the teaching opportunities and support of the members of the First Year Program: Dr. Amber Schaefer, Dr. Joanna Pellois, Veronica Ramirez, and Traci Zaragoza. Last and certainly not least is Sandy Manning who, during my whole time here, has been there for the ups and downs. Sandy has truly

gone beyond the call of duty in supporting graduate student during their time at Texas A&M University.

My scientific career did not begin the day I walked into graduate school. To Doug Ogletree, my high school science teacher, thank you for the encouragement and belief I could achieve my goals. To my Wayland comrades, Dr. Lori Ann Pretzer and Dr. Philip Carlson, thank you for your guidance. Thank you to my first research advisor Dr. Joel Boyd, I am ever grateful to count you as a dear friend and mentor.

To my family, my unwavering cheering squad, there are not enough words I could write on this page to express my deep love and gratitude to each and every one of you. From the oldest, my grandfather Gayland the ultimate Aggie fan, to the youngest, my nephew Zade, I owe an insurmountable debt of gratitude. My parents, Kerry and Connie Skiles, have always given me support no matter what goal I set for myself throughout my life and believe in me even when I did not believe in myself. I know that without such amazing parents, who were willing to sacrifice so much for me, I would not be where I am today.

Finally, I thank God for his endless love and blessing.

TABLE OF CONTENTS

Page

LIST OF FIGURES

Page

LIST OF SCHEMES

Page

CHAPTER I

INTRODUCTION TO SURFACE SCIENCE

Due to its importance in chemical and energy conversion technologies the development of surface science has come to the forefront of intellectual pursuits. Surfaces are encountered every day in life. The phenomenon's of adhesion, bonding, friction, *etc*. that are leveraged daily for practical purposes have their foundations in the behavior of surfaces and their interactions. Surface science has a long history with surface phenomenon being described in ancient times, with extensive growth over the last half century.[1]

Condensed matter by definition has a surface or interface. An interface exists when two systems meet or between matter and a vacuum. The surface is commonly defined as the outer most layer of atoms at an interface or as several of the outer most layers.[1, 2] The definition utilized depends largely on the phenomenon in question and the analysis technique employed.

The development of surface sensitive techniques has boomed since the 1960s allowing for an ever increasing number of studies at the molecular level.[1] Surface sensitive techniques now exist, in numbers that could seem like an alphabet soup of acronyms, for studying the morphology, chemical, and physical properties of surfaces. Surface analysis techniques can generally be divided into two classes: spectroscopy and

scanning probe. Spectroscopic analysis studies the interaction of energy or a probe species with the surface. The second and newer class utilizes a physical probe to scan the surface and the movement of the probe is monitored. This litany of techniques is needed since no one technique can give all the needed information about the surface.

With the newly developed and improved surface characterization techniques over the last several decades, many surface based phenomena which were thought to be well understood have gone through and reexamination process increasing the knowledge of the field. Surface studies can be used to uncover new phenomenon on a small scale and help to develop new insights. These studies can lead to improvements in existing and creating new technologies. Already the knowledge gained by surface science is driving the technological revolution forward with new materials have been developed, such as carbon fiber composites and increasingly smaller electronic devices.[2]

Surface science studies can range from the pristine atomically controlled surfaces to increasingly complex systems. Pristine surfaces are studied under ultra-high vacuum conditions, and while giving valuable insight, are a far cry from the surfaces encountered in daily life. This dissertation will focus on two system types that covering both ends of the complexity spectrum. A complex layered polymer system is discussed in detail in Chapters II-VI. This investigation will study the physical and mechanical properties of a polymer surface. Chapter VII, discusses surfaces which are carefully prepared to known specifications in an ultra-high vacuum environment. This study investigates core phenomena to aide in the development of new and improved catalysis systems.

CHAPTER II

AN INTRODUCTION TO SMART POLYMERS

Polymers have become a near essential part of modern life, starting with the vulcanization of natural rubber in the early 1840s.[3] At the turn of the 20th century, the first fully synthetic polymer, Bakelite, was used in a variety of items, including electronics, toys, radios, and jewelry.[3] In today's modern world there is rarely an area in which polymer materials do not play a role from the mundane (packaging, toys, fabric, *etc*.) to the highly specialized (medical implants, bulletproof plastics, *etc*.). Polymers are continually being used in place of classic materials such as metal, wood, and glass. As polymers are replacing classic materials high demand is placed on their performance, durability, cost, and controlled functionality. To meet some of these demands there has been increasing interest towards "smart" polymers.

A smart or stimulus responsive polymer can respond to a myriad of stimuli, including solvents, temperature, electrical current, pH, and mechanical pressure resulting in a useful change in polymers physical structure or chemical state.[4-6] Smart polymers are designed such that a small change in the external environment can produce large changes in the chemical and physical properties of the polymer. Because of their responsive nature, smart polymers currently have applications in many areas, including microfluidics, surface functionalization coatings, cell cultures, and drug delivery.[7-9] Many of these smart polymers are currently being heavily researched because they have biomedical

applications owing to their tunable functionalities and biological compatibility. The ability of polymers to control delivery of drugs to specific targets within the body and facilitate the delivery of non-aqueous compatible drugs is a continuous growing field of study.[8, 10-14] One commonly used methodology for drug delivery is encapsulation of the drug in a copolymer that has at least one responsive moiety and has a mixture of hydrophilic and hydrophobic functionalities.[15-19] This type of copolymer will form micelles upon mixing in an aqueous solution, with the hydrophobic groups forming the inner core and sequestering the drug of choice as a guest molecule until release. When the responsive polymer is triggered by an external stimuli, such as temperature or pH, the micelle undergoes a phase change. The phase change can cause one of several results; the micelle can swell, it can collapse upon itself or it can disintegrate, each of these will lead to the release of the sequestered guest drug molecule. For biological applications it is important that the polymer be soluble in aqueous environments and for the polymer to be controlled in a precise mannor.[13] To accomplish these goals the in-depth study of responsive polymers mechanisms, behavior, and properties must continue.

A majority of smart polymers are classified as thermoresponsive polymers, which are temperature responsive polymers that show a drastic and discontinuous change of their physical properties with temperature.[4, 16-18, 20-22] Temperature responsive polymers have a tunable response to changes in temperature, but are also known to respond to changes is solvent composition, pressure, or electrical current. A thermoresponsive polymer with much research being dedicate to it is poly(*N*-isopropylacrylamide) (PNIPAM). It is

considered a thermoresponsive polymer due to its lower critical solution temperature (LCST) at 32°C in aqueous solutions. The LCST is the temperature at which the polymer undergoes a phase change, such that it is no longer soluble in solution. The phase transition occurs when the polymer chains' hydration decreases leading to a change from a highly solvated random coil to a less solvated tighter globular conformation. The LCST phenomenon has been reported for thermoresponsive polymers dissolved in water and organic solvents. A few polymer-solvent systems that exhibit a LCST are PNIPAM in water,[23] poly(vinylcaprolactame) in water,[24] polyvinyl methyl ether in water,[25] polypropylene in n-hexane,[26] polystyrene in butylacetate,[27] and polydimethylsiloxane in butane.[28] While polymers can show LCST behavior in non-aqueous solvents, the remainder of this text will focus on LCST behavior in aqueous environments.

Thermoresponsive polymers display a miscibility gap in their temperature-composition diagram.[20] If the miscibility gap is found at high temperature the polymer is said to have an upper critical solution temperature where as if the miscibility gap is found at low temperatures the polymer has a lower critical solution temperature. When the polymer that exhibits LCST behavior is solvated, in maintains an extended coil conformation at lower temperatures; however, as the solution temperature increases the polymer changes to a globular conformation which is no longer soluble in solution. An oversimplified but useful way to describe the LCST phenomenon is to use the Gibbs free energy equation and the contributions of enthalpy (H) and entropy (S) on the polymer-solvent system.[20]

$$\Delta G = \Delta H - T\Delta S$$

Hydration of PNIPAM in this argument enthalpically favored but disfavored entropically because of the requirement that solvation organizes up to three water molecules per monomer unit. The enthalpic advantage for the system is due to the polymer containing hydrophilic groups which are solvated by hydrogen bonding with the solvent. However, because it is necessary for water to order along the polymer to form hydrogen bonding there is less favorable entropy of solution. The polymer conformation transition is driven by an increasingly unfavorable change in entropy that is induced by the increase in temperature. As the temperature increases, the enthalpic advantage of the system from salvation is overwhelmed. At the critical temperature the enthalpic (ΔH) and entropic (TΔS) terms of the Gibbs equation are equal in magnitude and opposite in sign. The polymer eventually crosses from a negative to a positive value for the Gibbs free energy (G) leading to the phase transition.[20] To counteract the change in G, the extended coil polymer conformation collapses to a more entropically favored globular conformation. The globular conformation is insoluble and will phase separate from the solvent (Figure 2.1).

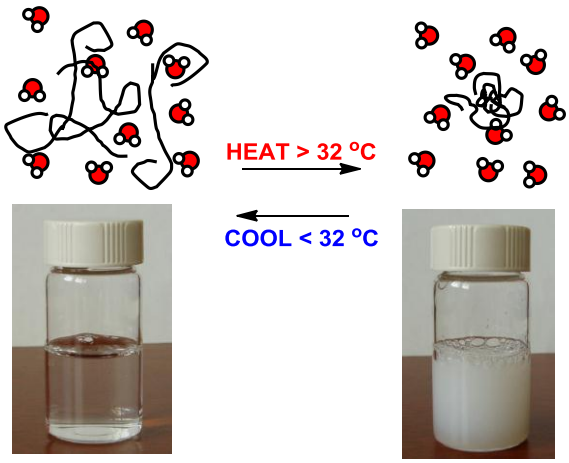

Figure 2.1. The effect of temperature on the solubility of PNIPAM.

The LCST of smart polymers can be experimentally determined by several methods, including light scattering, atomic force microscopy (AFM), quartz crystal microbalance, light spectroscopy, differential scanning calorimetry, Fourier transform infrared spectroscopy (FT-IR), and fluorescent labeling.[24, 29-35] Each of these methods tracks the polymers conformation by using either scattered light or changes in physical properties. The LCST can be determined for a polymer using AFM by imaging either a single polymer chain's conformation on the surface or tracking the change in height of a polymer film with changing temperature.[36, 37] Figure 2.2 shows the determination of the LCST of a PNIPAM film that has been grafted to an epoxide-functionalized silicon substrate.[37] The image is slowly collected as the temperature of the system is increased. At the LCST there is a dramatic shift in the height and surface structure of the polymer

film. While this method is effective for determination of the LCST, there are arguably simpler methods that can be utilized.

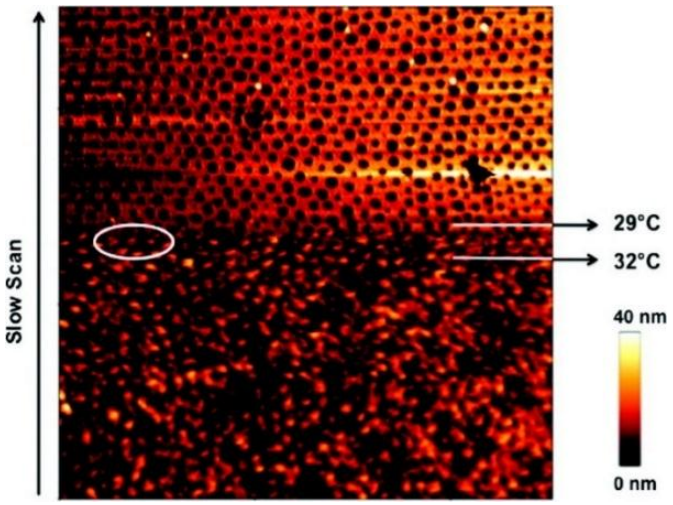

Figure 2.2. LCST determination of PNIPAM by temperature gradient AFM. Reprinted with permission from Popa, A. M.; Angeloni, S.; Bürgi, T.; Hubbell, J. A.; Heinzelmann, H.; Pugin, R. l. Langmuir 2010, 26, 15356. Copyright (2010) American Chemical Society.[37]

Since the phase transition of the polymer changes the size and solubility of the polymer either of these characteristics can be used to determine the critical temperature. The dynamic light scattering method makes use of the change in size of the polymer in solution. In a dynamic light scattering experiment a dilute solution of polymer is placed in the path of a laser light beam, the magnitude of the light scattered gives information of

the hydrodynamic radius of the polymer chain. As the temperature is scanned the radius of the polymer will have a disconnect around the critical temperature.[38] The change in conformation of the polymer at the critical temperature causes the polymer to become insoluble leading to a turbid solution, therefore scattering light. A temperature controlled UV-Vis spectroscopy experiment can track this turbidity change, but the downfall of this method is the need for a large volume of concentrated solution. Traditional light spectroscopy methods can be time consuming and the large sample volume can blur the onset due to inhomogeneity in the sample temperature. To circumvent these issues the research groups of Bergbreiter and Cremer developed a method in which the clouding point is measured as a function of position along a temperature gradient as opposed to a function of time.[39] For this high through put method, capillary tubes filled with the thermoresponsive polymer solution were placed on a stage of a dark field microscope. The stage's temperature was controlled by flowing heated or cooled liquid underneath the stage on opposing end creating a temperature gradient across the surface of the stage. The change in turbidity of the thermoresponsive polymer solution was monitored as a function of position on stage. This method allows for determination of the LCST within 1ºC without requiring a large sample size or narrow polydispersity. Based on many of the same principles used above, the LCST of a polymer can be determined by using an automated melting point apparatus.[40] In this method the thermoresponsive polymer solution increases in turbidity as the temperature is increased. This will yield a sigmoidal curve of scattering intensity versus temperature (Figure 2.3). To avoid convolution of the data with the base line, the LCST is typically reported at 10% scattering intensity.

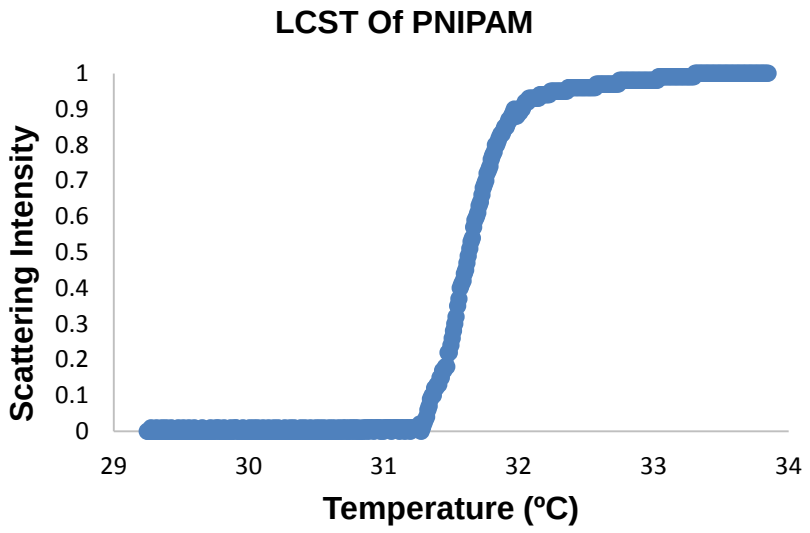

Figure 2.3. A graph of scattering intensity versus temperature used to determine the LCST of a PNIPAM solution. The LCST is taken at 10% scattering intensity.

LCST behavior is known for several polymers, many of which belong to the class of poly(acrylamides). Small changes in the chemical composition or chemical structure can lead to a wide range of the LCSTs. The LCST for PNIPAM occurs around 32°C, a physiologically relevant temperature which allows for its usefulness in biomedical applications.[11, 12, 34, 41] Below the LCST, the polymer is solvated and is in an extended coil configuration. Above the LCST, the polymer becomes hydrophobic; therefore, it transitions into a globular conformation. In the extended coil conformation it is energetically favorable for the hydrophilic amide and alkane groups of PNIPAM to be solvated, but this energetic favorability is lost above the LCST driving the conformation

change to the globular conformation at high temperatures. Structurally similar to PNIPAM, poly(*N*-ethyl-*N*-methyl acrylamide) has a LCST of 74ºC.[42] Poly(methyl vinyl ether) has a transition temperature at 37°C.[43] Poly(*N*-cyclopropylacrylamide) and poly(diethyl acrylamide) respectively have LCSTs of 30°C and 53°C.[39, 44] Depending on the molecular weight the LCST of polyethylene oxide can range from 100ºC to 180ºC.[45] If the hydrophilic and hydrophobic residues are well balanced, polypeptides can show LCST behavior. Composed of glycine (G), valine (V), proline (P), and isoleucine (I); the polypeptide P(GVGVP) exhibits a phase transition at 30ºC.[14] This transition is due to hydrophobic folding and assembly of the peptide.[46]

The mechanism driving the extended coil to globular transition has and continues to receive much research and debate. The coil to globular transition upon heating and the reverse globular to coil transition with cooling are complex transitions evolving through several stages.[47-49] This transition is considered a simplified analog to processes in biological system such as protein folding and DNA packing; therefore it is of great interest to understand the LCST mechanism to further the understanding in biological systems.[50, 51] Many of the techniques used to measure the LCST have also been used to gather information to determine how the transition is triggered and why.[47] Wu and Wang used static and dynamic laser light scattering to study the coil to globular transition in PNIPAM.[34] They found that during the transition the polymer transitions through four distinctly different morphologies. In this study the hydrodynamic radius and the radius of gyration for a single polymer chain in solution were compared to divide the transition into

four phases. The phases progress with heating from the extended coil to the crumpled coil to the molten globule and finally the globule. The hysteresis between heating and cooling is indicative of the polymer chain forming intrachain hydrogen bonds that hinder the melting of the globular structure upon cooling. Although research on the swelling/shrinking behavior of responsive polymers is well documented, the kinetics of the transition and relationship to the internal structure are not well understood.[34]

The LCST of a polymer can be affected by several internal and external factors, such as, molecular weight, end group structure, copolymerization, and salts in solution.[23, 52-55] Copolymers can be synthesized with a combination of the desired polymers to tailor the LCST.[52-54] Increasing the number of hydrophilic groups in the copolymer tends to lower the Gibbs free energy resulting in a higher LCST. The effect on the LCST is dependent upon the balance of the hydrophilic and hydrophobic groups as well as the distribution pattern of the monomers within the copolymer. When NIPAM is copolymerized with N-(4-vinylbenzyl)-N, N-diethylamine in an ABA triblock geometry the polymer chain exhibits two distinct LCSTs, with each segment of the polymer retaining the LCST of its homopolymer counterpart. The triblock polymer can transition between morphologies including polymer chains, flowerlike micelles, and micellar aggregates depending on which one or both of the polymer sections has undergone a phase transition.[21] Whereas, when NIPAM is randomly copolymerized with methyl methacrylate in one to one stoichiometric amounts, the LCST of the copolymer is now 58ºC, compared to the PNIPAM homopolymer LCST of 32ºC.[56]

An example of an external factor changing effecting the LCST is by the addition of salts to the aqueous polymer solution. In 1888, Franz Hofmeister used a series of salts to precipitate proteins from egg whites.[23] He found that the effectiveness was based on the salt identity. He ordered the salts based on their ability to denature proteins; this series is commonly referred to as the Hofmeister anion series and has the following order: [23]

$$CO_3^{-2} > SO_4^{-2} > H_2PO_4^- > F^- > Cl^- > Br^- \approx NO_3^- > I^- > ClO_4^- > SCN^-$$

It was originally thought that the kosmotropes, to the left of Cl^-, and chaotropes, to the right of Cl^-, changed the bulk structure of water. Kosmotropes were believed to be capable of introducing water structure; therefore, having a "salting-out" effect on the proteins. Chaotropes break up the water structure leading to a "salting-in" of the protein. Using femtosecond two-color pump-probe spectroscopy, it has been found that anions do not alter the hydrogen bonding network of bulk water beyond the hydration shell encapsulating the ion.[57] As such, the theory of salts effecting the bulk structure of water to effect the LCST has since been replaced with evidence of interaction of the polymer with the ions and the adjacent hydration shell.[58]

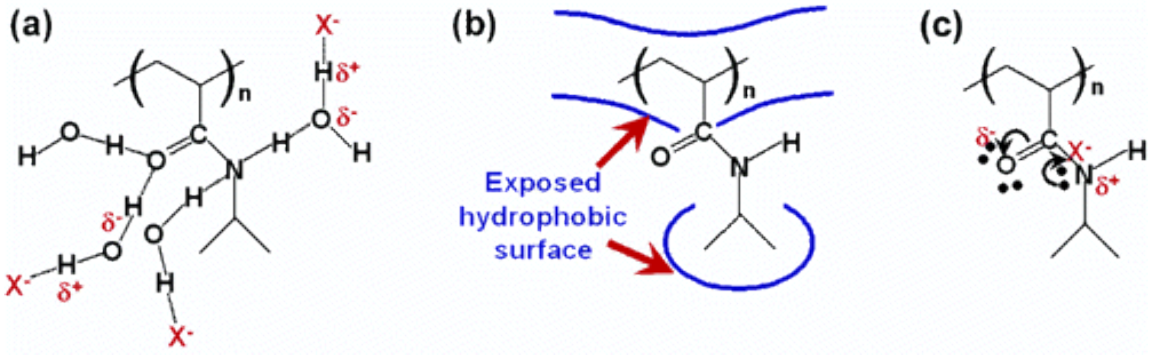

Figure 2.4. Interaction of Hofmeister anion with PNIPAM. (a) Water molecules polarized by the anion (X-) destabilize the hydrogen bonding of the amide. (b) Hydrophobic regions in which the surface tension is increased. (c) Direct binding of the anion to the amide. Reprinted with permission from Zhang, Y.; Cremer, P. S. Curr. Opin. Chem. Biol. 2006, 10, 658. Copyright (2006) Elsevier Ltd.[58]

The Hofmeister series has shown salting-in or -out behavior for many systems, including polymers and proteins.[36, 59-61] As reported by the Cremer group, the Hofmeister effect on PNIPAM was found to come from three basic interactions between the polymer, the anions and the water molecules of the hydration shell as shown in Figure 2.4.[32, 62] Kosmotropic anions act by polarizing the bound waters hydrating the amide group (Figure 2.4a). Both kosmotrophic and chaotropic anions raise the surface tension at the polymer and water interface increasing the entropic cost of hydrophobic hydration (Figure 2.4b). Thirdly, the chaotropes can directly bind to the amide side chains (Figure 2.4c). The first two of these interactions led to the salting out of the polymer which is manifested with a lower LCST. Additionally these two interactions are linearly concentration dependent. A

salting in effect is seen with the third interaction. This effect has a simple saturation behavior and a small increase of the LCST can be seen.

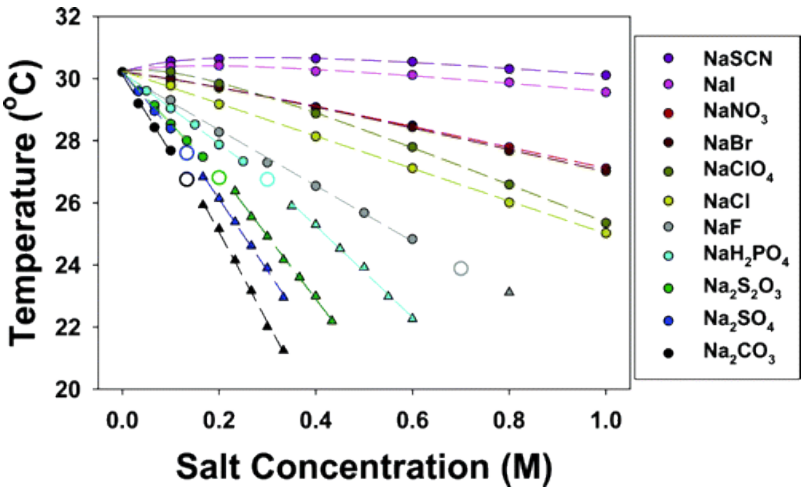

Figure 2.5. LCST temperature for aqueous PNIPAM in various sodium salt solutions. Transition to the second collapse phase is marked with an open circle. Reprinted with permission from Zhang, Y.; Furyk, S.; Bergbreiter, D. E.; Cremer, P. S. J. Am. Chem. Soc. 2005, 127, 14505. Copyright (2005) American Chemical Society.[62]

The effect of a salt on the LCST is dependent upon the identity and concentration of the salt in solution, as seen in Figure 2.5.[62] Chaotropic anions lead to a slight salting in effect. Adding kosmotropes to solution leads to the depression of the LCST. This is seen to the largest extent with the carbonate ion, which is on the extreme end of the Hofmeister series. The five kosmotrophic ions show a linear dependence on salt concentration.

Above a certain concentration, a two-step phase transition can be observed for the kosmotrophic ions. This two-step transition is attributed to the salting out of the amide group followed by the dehydration of the polymers' hydrophobic portions. The result from the Cremer lab lead to the conclusion that the kosmotropes and chaotropes work by separate mechanisms instead of one continuous mechanism.[62]

While most of the discussions thus far have regarded dissolved polymer chains, smart polymers can be synthesized in many shapes and forms, such as hydrogels, colloids, micelles and attached to surfaces.[63] Hydrogel and colloidal particle smart polymer morphologies are receiving considerable interest for applications in a variety of fields, including drug delivery.[14] While there is a great deal of interest and applications of smart polymers in solution phase, the remainder of this dissertation will focus on properties and applications of polymers grafted to a surface. Confinement to a surface allows for the same phase transitions of the polymer, but it is restricted to two dimensions. This confinement can effect changes the physical properties of the polymer. Responsive polymer surface applications can include: biological compatible drug release implants, chemical sensors, flow rate control, self-cleaning, and controlled wettability.[37, 64-66] Of interest in this dissertation is the attachment of a thermoresponsive polymer with a hydrophobic to hydrophilic transition. When anchored to the surface the polymer undergoes the same transition, resulting in a surface that switched hydrophobicity with temperature. This leads to a surface with reversible switchable wetting properties from a hydrophilic to hydrophobic surface.

Several types of surfaces may be referred to as responsive surfaces including hydrogels, self-assembled monolayers, and electrostatically or covalently bound polymer surfaces.[63, 67, 68] Polymers can be coated to many different surface types such as metals, oxides, and other polymers. Many approaches for attaching polymers to substrates have been used, but generally fall into two major categories, "grafting to" and "grafting from" the substrate.[22, 41, 69, 70] The "grafting from" approach uses surface initiators to grow the polymer out from the surface, creating a polymer brush structure. In the "grafting to" method, the polymer is first synthesized in solution and then attached to the surface. The "grafting to" approach allows for the polymer to be synthesized and characterized before attachment to the surface.

The "grafting from" approach is commonly used to generate polymer surface coatings. The method involves a polymerization reaction that begins with an initiator attached to the surface and the polymer chain grows out away from the surface. This method forms a polymer brush surface where one end of the chain is grafted to the surface and one end is free. The grafting density of this method is controlled by the initiator density on the surface and steric hindrance during brush growth.[22] The phase transition of the polymer can be diminished by the lack of space preventing physical transformations in the surface. A simple method for synthesizing a brush structure is through controlled radical polymerization.[71] Using atom transfer radical polymerization (ATRP) the surface is modified with a radical initiator which under goes radical polymerization. The method is applicable to a wide set of functional monomers.[72] ATRP generates a polymer brush

with a low polydispersity and a linear growth mechanism up to several hundreds of nanometers. Surface initiated polymer growth can also go through ring opening metathesis polymerization (ROMP).[71] This mechanism is limited to certain monomer classes and generates thin films without additional free initiators. Two additional growth mechanisms, anionic and cationic polymerization, are very sensitive to reaction conditions; therefore, are limited in use.[73] Grafting from methods can be used to functionalize non-planar substrates such as particles.[74] These "hairy particles" are of great interest for medical or industrial applications.

The second general class of surface modification is known as "grafting to". In this approach the polymer is first synthesized in solution, then, by one of various methods, is attached to the surface.[10, 75, 76] One benefit of this surface modification method is the polymer can be characterized by tradition methods (NMR, gel permeation chromatography, FT-IR, *etc*.) prior to surface functionalization. The grafting to process relies on attachment of the polymer to the surface by formation of electrostatic interaction, hydrogen bonding, or covalent bonding. For example, a polymer can be spin coated onto the surface and cross-linked to the substrate material through reactive crosslinking groups.[77] Polymer networks known as hydrogels can be cross-linked to the surface, maintaining their swelling and de-swelling capabilities.[78] The grafting to method used within this dissertation is layer-by-layer (LbL) assembly.

A method for attaching polymers to a substrate is the layer-by-layer assembly method, a process method to build a robust surface by adding successive layers to the

surface. LbL assembly is beneficial due to its adaptability. The assembly process can be achieved using electrostatic interactions, hydrogen bonding, and covalent bonding for assembly.[10] Substrates with wide ranging surface chemistry, sizes and shapes can all be modified with nano-thin multilayers using LbL assembly. The first known example of LbL assembly was seen with the ancient Chinese in the Qing Dynasty.[79] The sap from lacquer trees was repeatedly applied to the surface; while drying the phenolic lipids underwent polymerization forming a glossy finish. Recently, the LbL assembly process has been oriented toward building surfaces through ionic and hydrogen bonding.[80-82] Covalent LbL assembly produces surfaces that are more robust and more chemically stable from dissolution in solutions of extreme pH or ionic strength.[83]

For successful LbL assembly a set of experimental conditions must be met.[83] First, the polymers and/or materials used must have functional groups capable of electrostatic interaction or bond formation. Second, side products formed during the reaction should be removable or non-damaging to the surface. The third and less stringent condition is for feasibility the reactions should proceed under ambient conditions in aqueous or organic solvents. These conditions allow for a large variety of surface formation types. LbL assembly can be used to functionalize a variety of shapes and size. For example, Ogawa and coworkers utilized LbL assembly to functionalize electrospun nanofibrous membranes.[84] The individual fibers of the membrane increased in diameter as successive layers of negatively charged poly(acrylic acid) and positively charged titania nanoparticles were added.[84] This one example highlights two important benefits of LbL

assembly, first it is conformal to surfaces of complex geometry and second the layers can be composed of any chemical species that meet the above conditions. In LbL assembly applications of a bilayer system the layers can be exchanged for non-polymeric components such as graphene flakes, nanoparticles, clays, *etc*.[10, 75, 83, 85, 86] Besides the affordability of a variety of layer components, LbL assembly process can be adapted to application by dip coating or spray coating.[87-91]

Electrostatically driven LbL assembly is one of the most commonly used techniques. For ionic LbL assembly a surface is submerged (or sprayed) in an anionic polyelectrolyte solution followed by rinsing.[92] The anionic surface in then treated with a cationic solution. Repeating this cyclical process allows for the continual buildup of the surface based on the alternations in the polyelectrolytes charge. The reverse order is also possible. Ionic assembly methods benefit over covalent processes with their increased speed and cost effectiveness.[93] A second non-covalent assembly method is based on hydrogen bond formation. Alternating layers of hydrogen bond donors and acceptors can be grafted on a surface.[94, 95] Hydrogen bond LbL surfaces have been form with poly(allylamine hydrochloride) and 50 nm silica nanoparticles.[96] In this example the superhydrophobic behavior of the lotus leaf structure was mimicked by the creation of a honeycomb-like polyelectrolyte multilayer surface.[96] For covalent LbL assembly the process relies on alternating layers of electrophilic and nucleophilic layers. Successful fabrication of the surface with responsive polymers can be confirmed with a variety of analytical techniques including FT-IR, AFM, and contact angle analysis. If the surface

exhibits responsive wettability, such as the hydrogen bond LbL surface discussed, contact angle analysis would prove to be especially useful.

The work, presented in this dissertation, utilizes the Hofmeister anion responsive LbL surfaces. A detailed synthetic procedure for creating these polymer surfaces on glass, silicon wafers and porous frits has been previously published.[30, 65, 97] The surface is synthesized with covalent bonds between alternating electrophilic, N-acryloxysuccinimide groups found in the copolymer used PNIPAM-*c*-poly(*N*-acryloxysuccinimide) (PNASI) , and nucleophilic species, polyethylenimine (PEI) or aminated silica particles. Detailed studies regarding the films synthesis, wetting, and topography have already been reported. [30, 65, 97] One aim of this research is to determine the tunability of the mechanical properties of stimulus responsive polymers grafted to surfaces and its switching mechanism. If these surfaces are to be used for biocompatible surfaces the mechanical behavior is influential for bacteria growth and tissue attachment.[98-100] The second goal is to develop a method using these polymer grafted films for an environmentally stable and reusable separations membrane. Here in, we will discuss the mechanical properties of controlled wetting surfaces and the use of responsive films for oil/water separations. For these applications surfaces functionalization with PNIPAM have been utilized.

PNIPAM was first synthesized in 1956 and within a year PNIPAM had found its first application as a rodent repellent.[101] The polymer can be synthesized by free radical initiation of organic solutions, redox initiation in aqueous media, ionic initiators or

substitution of functional groups.[101-104] The first mention of PNIPAMs inverse temperature solubility were reported by American Cyanamid Company in 1963, although they noted a gradual decrease in solubility with increasing temperature.[101] More detailed reports of PNIPAMs LCST behavior came from Scarpa, Mueller, and Klotz in 1967 and Heskins and Guillet in 1968.[105, 106] While the first reports of its unique thermal properties were first reported in the 1960s; it was not until the 1980s that PNIPAM saw an explosion of interest with the realization of its potential applications. Initial interest in PNIPAM was almost all on solution phase or hydrogels, however, PNIPAM has a unique transition when bound to a surface. When PNIPAM is grafted to a surface and the LCST is exceeded, the polymer undergoes a transition from a hydrophilic to a hydrophobic surface. This transition allows for a surface with switchable wetting properties.

When PNIPAM is bound to a surface, the surface is responsive for the same reason the free polymer chain changes conformation in solution. This conformation change is restricted on the surface through the covalent bonds formed along the chain. When below the LCST the polymer is hydrated and the contact angle is below 90º, indicating a hydrophilic surface. When the LCST is exceeded the polymer chain dehydrates and becomes hydrophobic. Of interest is how the restricted conformation change and dehydration of the polymer effects the mechanical properties of the surface.

Much of the research on responsive surfaces has focused on creating a responsive wetting surface. Controlled wetting surfaces can be achieved through surfaces with complex topographic geometries on metals and polymer surfaces.[107-113] One integral

aspect for superhydrophobic surfaces is that there is a need for surface roughness. This can be accomplished by roughening the surface, patterning the surface with lasers or etchants or by incorporating roughness in the deposited film. The choice to incorporate silica nanoparticles in the PNIPAM LbL films was made in part to accomplish this task. The nanoparticles also serve as a layer component in the assembly process.

Switching mechanical properties of the responsive films has generated some interest as sensors and anti-biological surface coatings.[69, 114-117] When a responsive polymer is bound to a surface, it still undergoes a conformation change, although it is strained by linkages. This conformation change can yield changes in the mechanical properties of the film. Melzak and coworkers investigated the mechanical properties of the thermoresponsive hydrogel prepared from N-isopropylacrylamide and acrylic acid with benzophenonemethacrylate as a photoreactive cross-linker comonomer.[116] The properties were evaluated using an atomic force microscope in aqueous solution. It was found that the surface forces of the polymer remained constant as the temperature was increase to above the LCST, but the mechanical response indicated that the sample had been heated above the LCST and restructured.[116] This surface effect was attributed to segregation of acrylic acid polymer segment at the surface which do not change their attractive forces with temperature. However the bulk of the polymer hydrogel becomes dehydrated above the LCST leading to an increase in stiffness of the gel.

Responsive polymers can be grafted to a variety of architectures from flat surfaces, nanofibers, particles, and porous surfaces.[65, 84, 118, 119] An unique opportunity is afforded

when the responsive polymer is grafted onto a porous or mesh surface; it can be utilized as a flow regulator or separation membrane.[65, 120, 121] These applications take advantage of the restructuring properties of the polymer to either block the pore or the wetting properties of the film to prevent passage of undesirable compounds.

The synthesis of the PNIPAM LbL grafts will be discussed in Chapter III along with the experimental methodology background. The mechanical properties of the responsive grafts on silicon wafers with the goal of generating a surface with properties that can be controlled using an external stimuli is explored in Chapter IV. While in Chapter V, the responsive polymer graft formed on porous silica filters will be used for oil/water separations. The chapter focus on the development of a quick and environmentally friendly separation technique and its characterization. Both of these goals rely on a responsive polymer surface.

CHAPTER III

EXPERIMENTAL METHODS AND METHOD BACKGROUNDS

Overview

This chapter focuses on utilizing the specific properties of the thermoresponsive polymer poly(*N*-isopropylacrylamide) (PNIPAM) by grafting the polymer using layer-by-layer assembly onto silicon wafers and porous silica filters. The grafted film is composed of primarily the responsive polymer PNIPAM and silica nanoparticles. This chapter outlines the synthesis of covalent layer-by-layer polymer grafts on silicon wafers and on porous silica filters. In addition, the experimental methodologies and background used in later chapters are explored.

Responsive Polymer Surfaces

Surfaces that respond to a stimulus such as temperature, pH, ionic strength, or electrical fields are classified as responsive surfaces. One of the most common methods to generate a responsive surface is to functionalize the surface with a polymer. This can be accomplished by growing the polymer out from the surface creating a polymer brush. This method is commonly termed the "grafting from" approach. This approach was used by Svetushkina and coworkers to make smooth and rough surfaces functionalized with poly(oligo(ethylene glycol)) methyl ether methacrylate-*c*-2-(2-methoxyethoxy)ethyl methacrylate).[122] These surfaces were shown to have controllable wetting and adhesion

properties based on the temperature and the magnitude of the change was controlled by the surface roughness. Functionalization of a surface with a polymer film can also be accomplished utilizing the "grafting to" approach. In this method a previously synthesized polymer is attached to a surface via electrostatic or covalent linkages. This is accomplished using a polyvalent polymer that can attach to the surface at several points along the polymer chain. This method can be extended to a layer-by-layer (LbL) assembly process. For LbL assembly the polyvalent species in one layer must have opposite charge as opposed to the second layer, if using electrostatic assembly. If utilizing covalent LbL, the two opposing species must have functional groups that can readily form covalent linkages.

This chapter discusses the synthesis of thin PNIPAM/SiO_2 films. The films were deposited on silicon wafers to allow for study of the mechanical properties of the film before and after restructuring (Chapter IV). The films were deposited on porous silica filters to study their application as an oil and water separation membrane (Chapter V). The film formation is a modification of the original work in the Bergbreiter group functionalizing polyethylene substrates.[97]

Synthesis of Starting Polymers and Materials

The LbL assembly process is dependent on the polymers being synthesized ex situ. For the alternating layers reactive polyvalent reagents are needed. In the formation of the PNIPAM/SiO_2 grafts covalent assembly dictated the need for electrophilic and nucleophilic reagents. Two electrophilic polymers were used in this assembly process;

poly(*N*-acryloxysuccinimide) (PNASI) and the copolymer PNIPAM-*c*-PNASI. The nucleophilic species incorporated were either polyethylemine (PEI) or 10 and 100 nm silica nanoparticles functionalized with 3-aminopropyltriethoxysilane (APTES).

The NASI monomer was first synthesized from the precursors N-hydroxysuccinimide and acryloyl chloride (Scheme 3.1). Using free radical polymerization the PNASI polymer was synthesized as shown in Scheme 1 using 2, 2'-azobisisobutyronitrile (AIBN) as the radical source. The synthesized polymer was characterized by nuclear magnetic resonance (NMR) spectroscopy and compared to known chemical shifts (See Appendix). The second electrophilic polyvalent polymer used for the LbL assembly process was PNIPAM-*c*-PNASI. This copolymer was synthesized by free radical polymerization as shown in Scheme 3.2. This copolymer was characterized by NMR. Integration of the peaks characteristic of each monomer (4.00 ppm for NIPAM and 2.89 ppm for NASI) allowed for determination of the copolymer molar ratio. A 9:1 PNIPAM to PNASI ratio was obtained and utilized throughout all experiments. The final precursor material needed for the covalent LbL assembly was the nucleophilic silica nanoparticles. To be used as a nucleophilic component of the system the nanoparticles needed an amine terminal group. The 10 and 100 nm silica nanoparticles were initially cleaned in a 5% (v/v) HCl solution. The cleaned nanoparticles were functionalized using 3-aminopropyltriethoxysilane (APTES) to form a self-assembled monolayer on the particle providing many points for covalent linkages (Scheme 3.3). The amine terminal group on the particle can react with NASI groups to form an amide bond. The surface

amine loading was determined by treating 0.1 g of the nanoparticles with excess standardized HCl. After the nanoparticles reacted with the acid an aliquot of the acid was titrated with standardized sodium hydroxide.

Priming the Silicon Surface for Layer-by-Layer Assembly

Double side polished silicon wafers were used as the supporting substrate for the LbL synthesis. A cleaned silicon wafer was terminated with hydroxyl groups and was thus hydrophilic. This resulting surface did not have sufficient attachment points for the electrophilic polymers attachment, therefore the surface was reacted with APTES to create a nucleophilic surface (Scheme 3.4).[123] Treatment with APTES yielded a surface terminated with primary amines. To ensure complete reaction of the triethoxysilyl groups with the surface hydroxyls the wafer was heated after removal from the APTES solution. Due to amine groups having an affinity for the surface and water catalyzing the binding of silane molecules in a polymeric fashion, the treatment of the surface with APTES likely formed multilayers opposed to a self-assembled monolayer.[123, 124] The formation of a multilayer instead of a monolayer is irrelevant for the continuation of the LbL assembly. The formation of an amine terminated surface can be tentatively confirmed by the increase in contact angle of the surface.

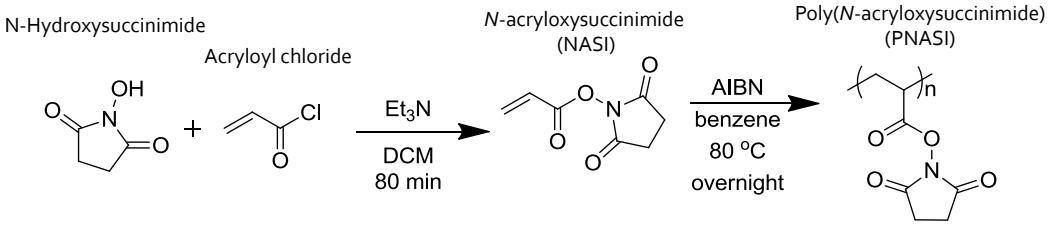

Scheme 3.1. Synthesis of NASI from precursors followed by polymerization to form PNASI.

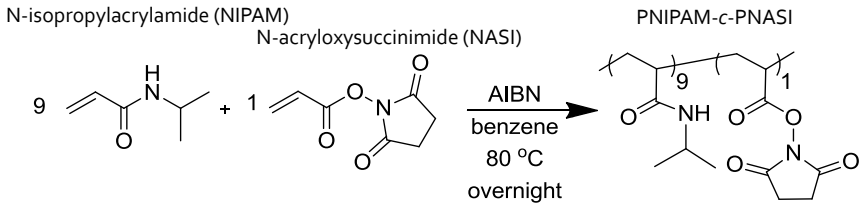

Scheme 3.2. Copolymerization of NIPAM and NASI.

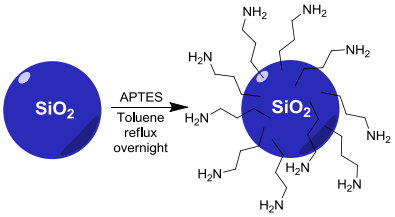

Scheme 3.3. Formation of a self-assembled monolayer of APTES of the surface of a silica nanoparticle.

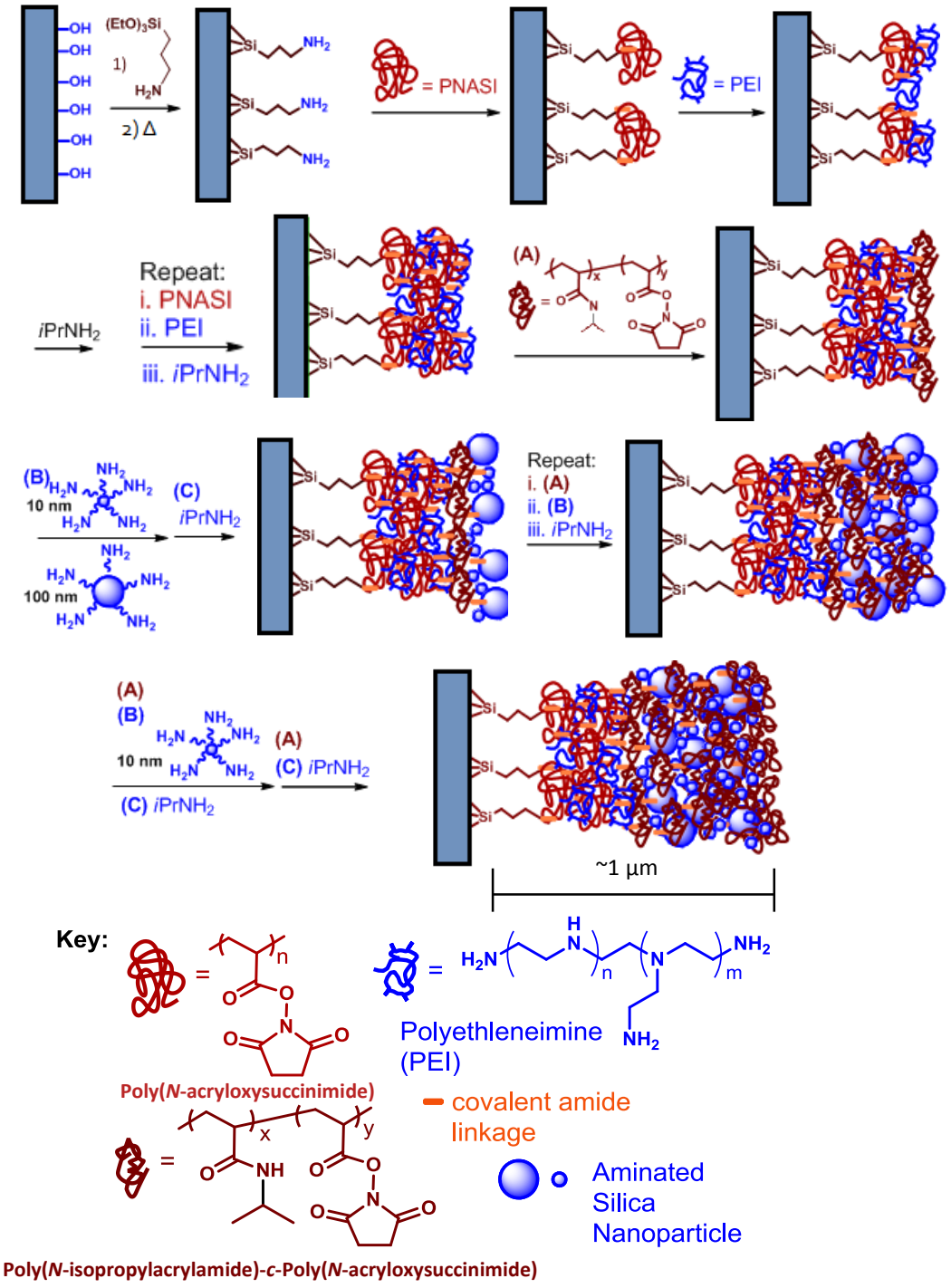

Scheme 3.4. The LbL process in its entirety.

While functionalizing the surface with APTES led to an amine termination, it is desired for the LbL assembly to have a higher density of the reactive nucleophilic groups on the surface. To increase the amine density on the surface two additional reactions were used. The substrate was submerged in a solution of PNASI, rinsed, and then treated with branched polyethylenimine. The PNASI formed covalent linkages with the surface, but due to constraints on the polymer chain multiple electrophilic active ester groups on the polymer were unreacted and exposed to the outer surface. The PEI polymer was then reacted with the exposed active ester groups on the surface forming covalent bonds; now the surface was effectively terminated with amine functional groups. While some of the active ester groups linked to the APTES surface and the PEI, there were still unreacted groups on the PNASI polymer chain. These unreacted groups were quenched with isopropylamine to form N-isopropylamine groups. The side product of this reaction, N-hydroxysuccinimide, was washed away from the surface using rinsing steps. Two of the PNASI/PEI bilayers were deposited on the surface and quenched with the isopropylamine. This assembly process was termed surface priming since it is effectively preparing the surface for the LbL assembly. These bilayers were bound to the surface to yield a denser array of nucleophilic amines for subsequent LbL assembly of the active thermoresponsive polymer and silica nanoparticles.

Covalent Layer-by-Layer Assembly of Silicon/(PNIPAM/SiO_2)$_6$/PNAIPAM Nanocomposite Surfaces

Using the electrophilic PNIPAM-*c*-PNASI polymer and the nucleophilic aminated silica nanoparticles a responsive nanocomposite graft was prepared on the primed silicon wafer using LbL assembly. This assembly process took advantage of PNIPAM's ability to generate a responsive surface with switchable wetting and elastic modulus. The silica nanoparticles were utilized for two primary reasons: to serve as a component of the LbL assembly bilayer pair and to generate roughness on the surface that enhances the responsiveness.

The LbL assembly of the responsive polymer graft continued after the priming procedure using PNIPAM-*c*-PNASI as the polyvalent electrophile. The NASI groups in the copolymer were the groups active in forming covalent bonds with amine terminal groups on the primed surface. As with the PNASI homopolymer, the copolymer is limited by steric constraints when reacting with the surface preventing complete reaction of the active ester groups with the amine terminated surface. A portion of the active ester groups were confined to the outermost layer of the polymer graft producing an electrophilic surface from the previously nucleophilic surface. The exposed active ester groups were available for reaction with the aminated silica nanoparticles. The LbL assembly process continued by submerging the substrate in a solution of the polyvalent nucleophilic aminated 10 and 100 nm silica nanoparticles. The nanoparticles were subsequently bound to the surface by the creation of an amide bond between the APTES monolayer and the

active ester exposed on the surface. Because of the incomplete reaction of the amine groups on the APTES with the active esters, the electrophilic surface once again became nucleophilic. At this point in the surface grafting procedure, there are unreacted NASI within the graft so the surface is treated with a solution containing isopropylamine. This primary amine converts any unreacted NASI groups to the thermoreactive NIPAM groups. This reaction increases the NIPAM concentration in the polymer graft and removes reactive sites which could over time alter the surface of the polymer graft. A total of five bilayers composed of the PNIPAM-*c*-PNASI and 10 and 100 nm silica nanoparticles was grafted to the surface. An additional sixth bilayer was added, but it was composed of the copolymer and exclusively 10 nm silica nanoparticles. This sixth layer was used to decrease the outermost roughness of the graft. The surface was then terminated with a layer of the copolymer which was quenched with isopropylamine. This final step ensured the topmost layer of the polymer grafted surface was covered with the thermoresponsive polymer. The attachment of the responsive polymer and nanoparticles to the surfaces was initially characterized by contact angle measurements using both pure water and 1.0 M Na_2SO_4. This allowed for comparison with previously established values.

Covalent Layer-by-Layer Assembly of Silica Frit/(PNIPAM/SiO_2)$_6$/PNAIPAM PNIPAM Nanocomposite Surfaces

Using the same grafting procedure to as to functionalize the silicon wafer with medium porosity, pore size 10-20 μm, were grafted with the PNIPAM/SiO_2 nanocomposite. Due to the complex geometry of the surface reaction times and rinsing

steps were increased in duration to ensure coverage throughout the frit. Since the porous frit is prone to breakage and chipping during physical shaking the filters were housed in Teflon holders similar to those shown in Figure 3.1. The frits were held in the holder by nylon screws. This arrangement allowed for maximal surface area exposure while protecting the fragile frit from breakage during reaction steps carried out with agitation by a wrist action shaker. The holder was used for all processing steps with the exception of the nylon screws being removed during the initial piranha cleaning step.

Figure 3.1. Teflon holder used for surface grafting porous silica substrate. A frit is inserted into the top positon in this picture.

Experimental Methodologies

Contact Angle Measurements

The most common way to determine the wettability of a surface is by measuring the contact angle. The contact angle is the angle measured where a liquid/vapor interface

meets a solid surface. This measurement gives a quantitative analysis of the wettability of a surface. The interaction of the liquid with the surface can be described simply by the Young's equation as follows:[125-127]

$$0 = \gamma_{SG} - \gamma_{SL} - \gamma_{LG} \cos \theta_C$$

This equation denotes the interfacial energy (γ) between the solid (S), liquid (L), and/or gas (G) and θ_C for the equilibrium or observed contact angle, as seen in Figure 3.2. A low contact angle implies interaction between the liquid and solid; as the contact angle increases there is less interaction between the surface and droplet. The wettability of water on a surface is typically broken into the following four classes based on contact angles: 0-30º is super hydrophilic, 30-90º is hydrophilic, 90-150º is hydrophobic and 150-180º is super hydrophobic.[128, 129] If there is a strong attraction between the solid surface and the liquid molecules, the droplet will completely spread out on the surface, corresponding to a 0º contact angle. One of the highest contact angles reported for a smooth CF_3-terminated surface is 120º.[130] Several factors influence the contact angle including surface terminal groups and overall surface structure.

Due to contact angle hysteresis, which is typical on a rough surface, the observed contact angle falls between the maximum value found by the advancing contact angle and the minimum value from the receding contact angle. The equilibrium contact angle is dependent on the relative strength of the solid as well as liquid and gas molecular interactions in thermodynamic equilibrium. As expressed above, when hysteresis is present on a surface, multiple contact angles can be found.

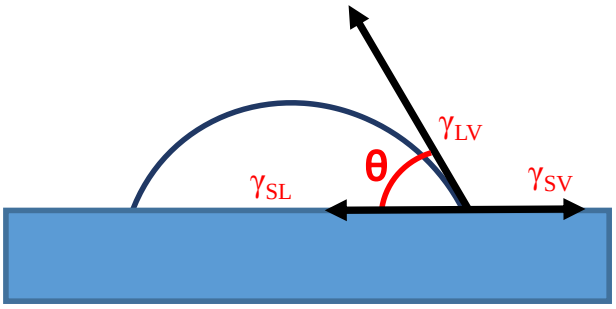

Figure 3.2. Contact angle depiction of a droplet on a hydrophilic surface. The phase boundaries are defined.

The wetting behavior is determined by a force balance of adhesive and cohesive interactions between the three phases involved. Cohesive forces in the liquid cause the drop to be strongly held together and avoid contact with the surface. Adhesive forces cause the liquid to spread along the surface due to attraction. The liquid droplet will completely spread out over the surface resulting in a contact angle near zero if there are strong attractive forces between the liquid and the outermost chemical groups of the surface, such as the case for water droplets on bare metallic or ceramic surfaces. Cases of super hydrophobicity are found on highly rough surfaces due to the presence of air pockets trapped between the liquid and solid interface. There are two major models used to describe wetting behavior on a rough surface which extends beyond the Young equation that assumes a perfectly flat and rigid surface, shown in Figure 3.3. The Wenzel model describes a homogeneous wetting of a textured surface in which the liquid completely wets the surface at the interface.[131, 132] The observed contact angle can be related back to

the Young contact angle by using a roughness ratio (r) to scale to results, as seen in the following equation:

$$\cos\theta^* = r\ \cos\theta$$

In this equation, θ* is the observed contact angle and θ is the Young contact angle. The roughness ratio is defined as the ratio of the true area of the surface to the apparent area. The second model to describe wetting on a rough surface is the Cassie-Baxter Model.[132] When dealing with a heterogeneous surface the Wenzel model is insufficient, therefore the Cassie-Baxter model is employed. The wetting of a heterogeneous surface involving trapping of air at the liquid solid interface can be described using the following model:

$$\cos\theta^* = r_f\ f\ \cos\theta + f - 1$$

In this case, r_f is the roughness ratio of the wet surface area and f is the fraction of the surface area wetted by the liquid. If f=1 and r_f =r the Cassie-Baxter model simplifies to the Wenzel model.

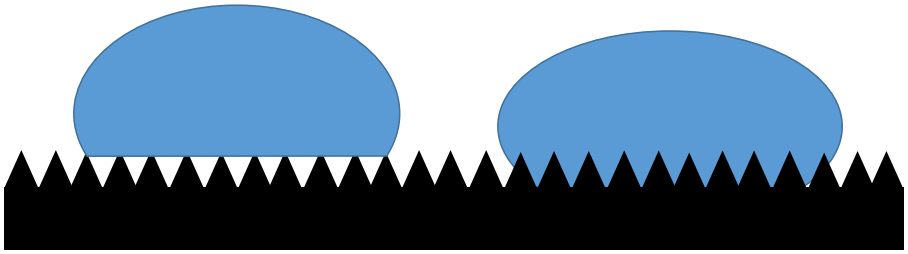

Figure 3.3. Wetting behavior on rough surfaces. The Cassie-Baxter model is shown on the left and the Wenzel model is shown on the right.

A common instrument for measuring contact angles is a goniometer. In this instrument a high resolution and high speed camera is used to capture images of a droplet placed on the surface from a motorized micro syringe. The images are then analyzed using a software program. For the studies contained within this dissertation two types of contact angles, static and advancing, are used. The static contact angle is found when a drop of a predetermined size is gently touched to the surface and allowed to equilibrate. In practice this is the simplest measurement. The advancing contact angle is similar to the static method, except the droplet is continually increased in size by slowly adding volume to the drop on the surface using the syringe and determining the largest contact angle without increasing the solid/liquid interface area. This method produces more consistent contact angles allowing for comparison between surfaces.

In addition to being useful in determining the hydrophobicity of a surface a goniometer can be used to measure the capillary action of a porous surface.[65] If the flat substrate is replaced on the goniometer stage, as seen with the work found in Chapter V, the rate of absorption of a droplet into the porous surface can be determined from the images collected. For a hydrophilic surface in addition to the drop spreading on the surface it will be draw into the pores by capillary action. If the porous surface is hydrophobic the droplet will remain on the surface and maintain a contact angle greater than 90º.

Atomic Force Microscopy

Invented by Binning, Quate and Gerber in 1986, Atomic Force Microscopy (AFM) is a high resolution scanning probe microscope.[133] AFM has an added benefit over Scanning Tunneling Microscopy in that it can scan samples under ambient conditions and the sample does not need to be conductive. The AFM can be used to obtain nanometer scale topographical images and frictional images as well as to measure physical properties (adhesion, elasticity) of a surface. An AFM can be modified in a variety of ways to measure conductivity, thermal properties, or tip-enhance Raman spectroscopy.[134] While an AFM can be modified, the general setup and operations stay the same. The AFM consists of a tip mounted on a piezoelectric material, the sample, a laser, and a photodiode detector (Figure 3.4).

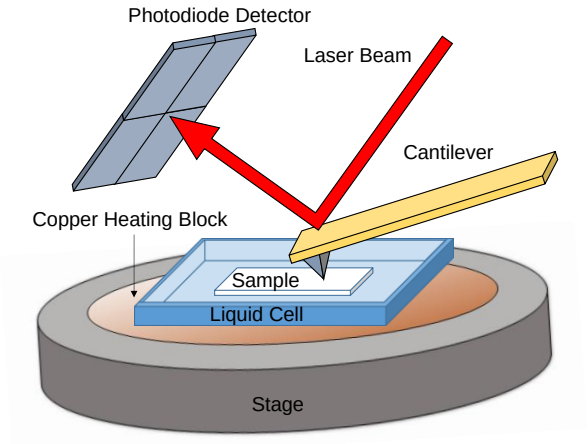

Figure 3.4. Atomic Force Microscope diagram. This setup features two modifications to a traditional set up: a copper heating block and a liquid cell. The cantilever is submerged in liquid to limit laser beam deflection. Image not to scale.

A micron-sized cantilever is attached to a chip typically made of silicon nitride and on the free end of the cantilever is the tip that interacts with the sample. The tip can be manufactured for specific needs. For example, the tips used within this scope of research were conical with a radius around 10-100 nm or a sphere with a radius ranging from nanometers to microns; the second type is commonly classified as a colloidal probe. For imaging purposes the tip is rastered across the surface of the sample in the x-y direction and the deflection of the cantilever is followed by the laser beam reflecting off of the backside of the cantilever onto the photodiode detector. A constant force between the tip and the surface is maintained by the feedback voltages controlled by the software that changes the tip height allowing the force to remain constant. Combining the x-y direction tip movement and tip deflection in the z direction a topographical image of the sample can be generated. This type of imaging is classified as contact mode, in which the tip is in contact with the sample and dragged across to generate the topographic image. A friction image can also be generated from the torsion of the cantilever. The second primary mode in AFM imaging is tapping or non-contact mode. In this mode the tip is not in contact with the surface; instead the cantilever is oscillated slightly above a resonant frequency and rastered along the surface. Long range forces, such as Van der Waals forces, decrease the frequency of the cantilever and this decrease is compensated for by the feedback loop adjusting the tip-sample distance. This mode of imaging is less damaging to the surface than contact mode and is more suitable than contact mode for scanning soft surfaces.

Liquid Cell AFM

An AFM can be operated in a variety of environments; for the research within this dissertation the desired environment is for the sample to be submerged in a liquid. This can be accomplished by mounting a liquid cell to the stage of the AFM and containing the sample and the liquid within the cell. The remainder of the AFM is setup and functions as normal.

Temperature Controlled AFM

From time to time a case arises in which it is desirable to conduct AFM experiments at elevated temperatures. Temperature control can be achieved by trading the normal AFM stage for a heating stage. For this work a high heat stage was used that heats the sample from below via resistive heating a copper block below the sample/liquid cell (Figure 3.4). The temperature of the heating stage was controlled with a LakeShore 321 Autotuning Temperature Controller. This controller has a digital readout of the stage temperature, but since the stage was being used to heat a liquid cell and the contained liquid the system needed calibration. For calibration a thermocouple was placed in the liquid cell on top of a silicon reference sample and the reading from the thermocouple was calibrated against the controller readout. This calibration can be seen in Figure 3.5. The heating of the stage and liquid cell was a relatively slow process that took over 2 hours to reach the desired temperature and stabilize.

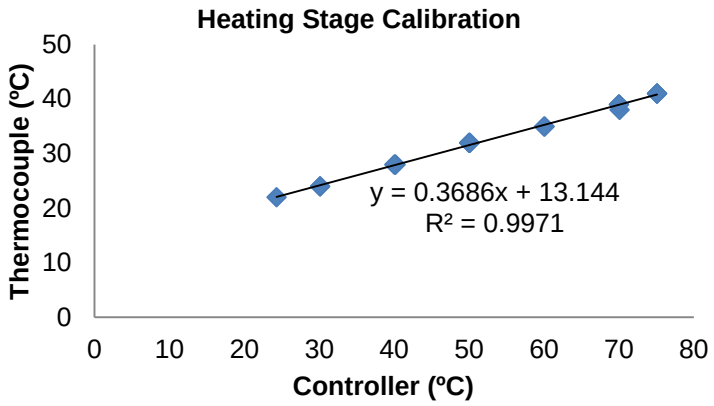

Figure 3.5. Calibration of the heating stage comparing the digital temperature readout from the controller to the thermocouple submerged in the liquid cell.

Nanoindentation

Besides surface imaging AFM can be used for force spectroscopy. In this method the forces between the tip and sample are measured as a function of the tip sample distance resulting in a force-distance (FD) curve. This curve can yield information regarding adhesive interactions and the elastic modulus of the sample. In this method, the AFM tip approaches the surface until a set force or distance traveled and then the tip is withdrawn while the deflection of the tip is tracked via the laser beam movement on the photodiode detector. If the spring constant of the tip and the deflection sensitivity of the detector is known the voltage to distance measurement from the AFM can be converted into a FD curve. A generalized FD curve can be seen in Figure 3.6. While the tip is approaching the surface the tip-sample distance is decreasing. When the tip is far from the sample it feels zero force from the sample, but as the tip nears the surface a "snap in" to the surface

occurs when the attractive forces between the tip and sample are large compared to the stiffness of the cantilever. After the snap in the tip-sample distance continues to decrease and the cantilever bends in response as the tip indents into the surface. Once the maximum force is reached the tip is withdrawn from the sample. The cantilever will continue to bend until the adhesive forces of the sample are overcome and the tip is released from the sample; this give a direct measurement of the adhesive interactions on the surface. Elastic modulus measurements can be calculated from force distance curves obtained with an AFM. Variations in the slope of force-distance (FD) curves yield information regarding the elastic modulus of the surface. The tip did not reach the incompressible substrate at any point during the measurements, which means that the measured indentation was less than the thickness of the polymer graft.

In the following experiments the voltage-distance curves generated by the AFM were averaged together using the Scanning Probe Image Processor software. To allow for averaging 20 curves were stacked together setting the low end of the distance range to zero. This accounts for the heterogeneity of the surface that is reflected in the z-direction measurements. The average curve was then fit by a least means square resulting in an average voltage-distance curve. To convert the voltage-distance curve to a force distance curve the deflection sensitivity of the cantilever and the spring constant were required. The deflection sensitivity of the cantilever was found from taking FD curve on a silicon reference wafer. The assumption was made in this case that the probe was not indenting into the surface and all the deflection was attributed to the bending of the cantilever. The

spring constant was determined using the Sader method.[135] The generated averaged FD curve was then adjusted as needed to where the force is zero when the probe is removed from the surface.

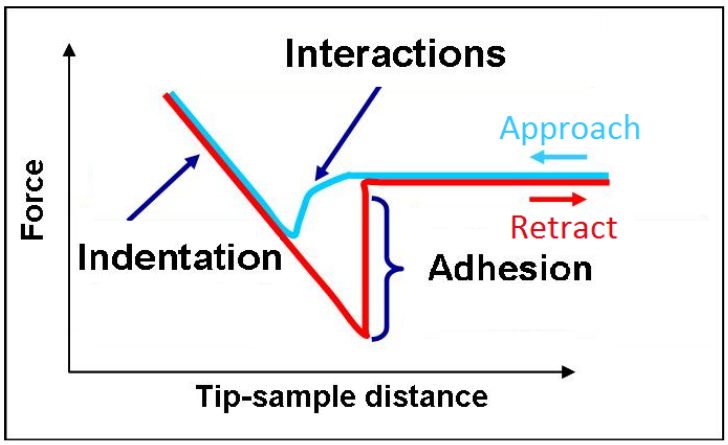

Figure 3.6. A generalized FD curve is depicted along with indications of what information can be gleaned from the individual segments of the curve.

Contact Mechanics

Using the AFM, FD curves can be obtained. The slope of the line after the tip has contacted the surface contains information on the elastic modulus of the sample. The elastic modulus can be qualitatively compared by analysis of the slope, but if quantitative comparison is desired the elastic modulus must be calculated using a contact mechanics

model. There are four main contact mechanics models to choose from and the choice is dictated by the information know about the sample and the tip. A generalized depiction of these four methods can be found in Figure 3.7.

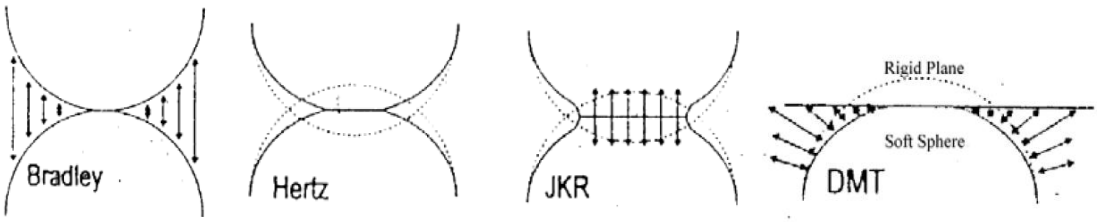

Figure 3.7. Depiction of the four major contact mechanics models.[136]

The one of the simplest contact mechanics model is the Hertz contact model that dates back to 1881. This model relates the contact area of a sphere with a flat substrate to the elastic deformation in the materials. This model neglects surface forces and adhesion. For this model the indentation into the surface at a given load, Poisson ratio and the radius of the tip are needed. The Poisson ratio can be found in the literature or experimentally determined for the materials being used. The other values needed for the Hertz contact model are experimentally determined. In the 1971, the JKR (Johnson, Kendall, Roberts) theory improved the Hertzian theory by adding adhesive interactions to the model. The JKR model is a fully elastic model that includes adhesion in the contact zone but neglects

long-range interactions outside of the contact area. Due to the inclusion of adhesion into the JKR theory, contacts formed during the unloading cycle can model the adhesion of the tip to the sample. The JKR model is best suited for soft samples with high adhesion to the tip. In addition to the variables needed for the Hertz theory, to utilize the JKR model the work of adhesion needs to be known. A third contact model is the DMT (Derjaguin, Muller, Toporov) theory. In this model, inside the contact remains Hertian, but adhesive forces are now allowed outside the contact. This model is applicable to stiff samples with low adhesion. The DMT theory simplifies to the fourth contact mechanics model, Bradley's model, when the two surfaces are separated by purely Van der Waals interactions. The Bradley's model is a non-contact model for two rigid spheres in the attractive regime of the Lennard-Jones potential.

While several contact mechanics models exist, the Hertz model has been chosen to model the contact within this dissertation. This choice was made to allow comparison of results to those in the literature where the Hertz model is utilized. This model is commonly used due to its simplicity. It is an acceptable choice as there is insignificant to no adhesion seen in the experiments discussed within the following chapter.

Colloidal Probe Characterization

Colloidal probes were purchased from AppNano with a 5 μm SiO_2 sphere and backside coated in gold (Fort- SiO_2-A-G-5). The probes were initially cleaned for one minute in a solution of 4:1:1 water, concentrated ammonium hydroxide, and hydrogen peroxide (35% v/v). The spring constant was determined via the Sader

normal spring constant method.[135] The radius of curvature was found by reverse imaging the probe on a TGT001 standard (NT-MDT) as seen in Figure 3.8.[137] Cross sections at the apex were fit using a parabolic curve using obtained with Scanning Probe Imaging Processor software. An average of 15 cross sections were used for the radius of curvature value for elastic modulus calculations. After every day of experimentation the probe was scanned across the standard to check for damage and to see if any polymer had been picked up.

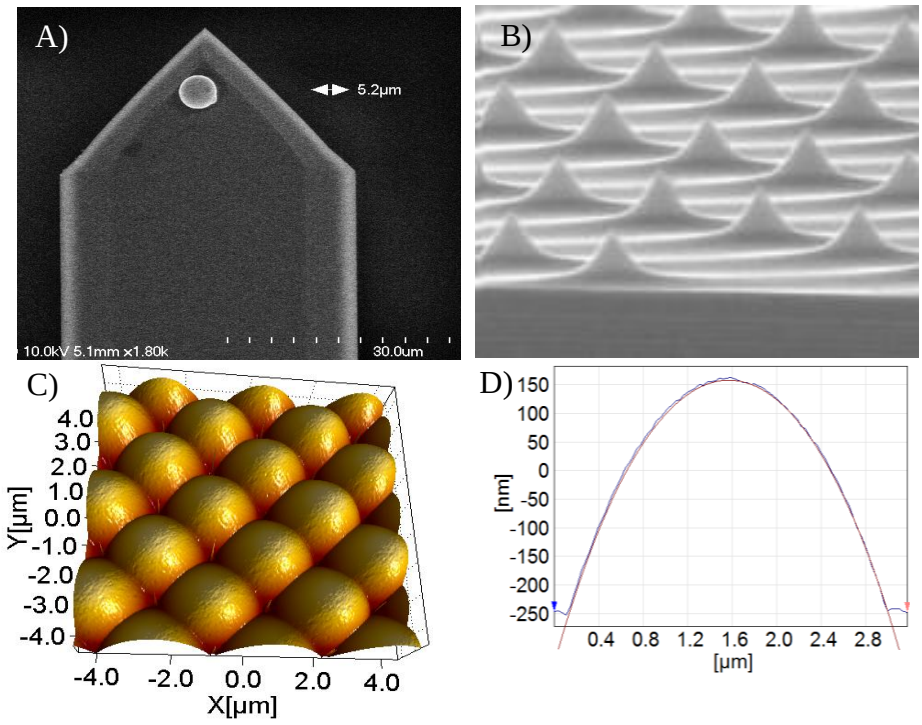

Figure 3.8. Characterization of the colloidal probe. A) FESEM image of a colloidal probe. Image provided by AppNano. B) Image of the TGT-001 standard. C) A 3-D rendering of an 8 x 8 µm contact mode AFM image of the colloidal probe on the TGT-001 standard. D) Cross section from image (C) in blue with the radial fit in red.

CHAPTER IV

TUNABLE ELASTIC MODULUS IN STIMULI RESPONSIVE POLYMER COMPOSITE GRAFTS FORMED BY COVALENT LAYER-BY-LAYER ASSEMBLY

Overview

Thermoresponsive polymers, such as poly(*N*-isopropylacrylamide), exhibit a lower critical solution temperature and a responsive nature when grafted onto a surface. Covalently bound layer-by-layer assemblies containing a stimulus responsive poly(*N*-isopropylacrylamide)-*c*-poly(*N*-acryloxysuccinimide) polymer and aminated silica nanoparticles were grafted onto a silicon wafer. These polymer composite grafts, ~1 μm thick in the dry state, are known to change wettability and topography in response to external stimuli. Here we show variations in the Young's elastic modulus of the polymer composite surface induced by external stimuli. Temperature variation and addition of counter ions to the surrounding solution from the Hofmeister series of salts were both studied to investigate their effect on the polymer composite grafts. Colloidal probe atomic force microscopy was used to measure the elastic modulus of the polymer film. The elastic modulus was found to be in the range of 3 to 189 MPa; dependent on the exposure of the polymer composite to varied temperatures, counter ions and rinsing procedures.

Introduction

A stimulus responsive or "smart" polymer can respond to a myriad of stimuli; including solvents, temperature, counter ions, electrical current, pH, and mechanical pressure.[4-6] A small change in the external environment can produce large changes in the chemical and physical properties of the polymer; such as surface wettability, roughness, adhesion, and hardness.[97, 138, 139] The responsive nature of the polymer has led to it use in microfluidic devices, surface functionalization coatings, cell growth cultures, and drug delivery.[7, 8]

One of the most highly studied stimulus responsive polymers is poly(*N*-isopropylacrylamide) (PNIPAM). It is considered a thermoresponsive polymer due to its lower critical solution temperature (LCST) in aqueous solutions, which occurs around 32^0C.[34, 41] The polymer undergoes a phase change at the LCST, such that it is no longer soluble in aqueous solution. Below the LCST, the polymer is solvated and is in an extended coil configuration. Above the LCST, the polymer becomes hydrophobic and transitions into a globular conformation.[20] The LCST of a polymer can be tailored by controlling copolymerization, molecular weight, and changes in the external environment.[52-54, 62] PNIPAM may be grafted by the synthesis of polymer brushes that are initiated from the surface or by synthesizing the polymer then attaching it to the surface.

Extensive research has been done and continues to determine the mechanism of the coil to globule transition observed at the LCST in solution. In solution, the removal of water from the polymer chain means that PNIPAM is no longer soluble, and the solution

becomes cloudy due to the formation of an insoluble PNIPAM phase. When PNIPAM is attached to the surface and is in contact with aqueous solutions, the phase transition causes the surface to become hydrophobic. How the polymer restructures on a surface has undergone less research than the solution phase restructuring. Using surface plasmon resonance measurements and neutron reflectivity studies indicate that the phase transition of PNIPAM grafted to a surface occurs over a broad temperature range around 32°C.[29] Additionally, studies of the polymer returning to its original conformation revealed that a difference exists in the respective energies involved in the hydration and dehydration of PNIPAM. This supports the idea that surfaces functionalized with the polymer are responsive for the same reason the polymer precipitates out of solution, but recovery times maybe extended. Surface bound polymers can be derived from several different synthetic routes leading to surfaces with polymers in different configurations. These varying configurations implement different constraints on polymer chain collapse. The polymer grafting method used is dependent on the desired application. Changes in the polymer graft structure can result in changes in the polymer's elastic modulus or a substance's resistance to being deformed elastically when a force is applied to it.

The Vancso lab investigated the elastic modulus changes of PNIPAM brushes in water and water/methanol (the co-nonsolvency effect is known to collapse the polymer chains).[69] Their interest lied with studying the impact of the co-nonsolvency effect on the brush height and mechanical properties. They found that when a PNIPAM brush structure is subjected to conditions that collapse the polymer chain, the film thickness decreases and

the polymer film density increases. The study of the co-cononsolvency effect on PNIPAM brushes concluded that the elastic modulus roughly doubles when the chains collapse regardless of grafting density. One key difference between this study and the work present here is the structure of the polymer film. In the brush structure the polymer chains are only constrained by the anchor to the surface and steric hindrance. In the layer-by-layer surfaces studied here, the polymer chains are covalently bound to the surface, to other polymer chains, and to the other layer components; therefore, the films react differently due to the constraints than polymer brush structures.

A detailed synthetic procedure for the covalent layer-by-layer anion responsive surfaces formed on glass, silicon wafers and porous frits has been previously published and can be found in Chapter III.[30, 65, 97] In brief, the surface is synthesized with covalent bonds between alternating layers of electrophilic and nucleophilic species. A copolymer of poly(*N*-isopropylacrylamide)-*c*-poly(*N*-acryloxysuccinimide) (PNIPAM-*c*-PNASI) serves as the electrophilic layer. The NIPAM groups contribute the responsive behavior, while the NASI groups provided a linker for covalent bonding. Synthesized polymers were analyzed using ^{1}H-NMR and compared to known chemical shifts before grafting to the surface. The nucleophilic layer is composed of a mixture of 10 and 100 nm (1:1 w/w) silica nanoparticles, capped with 3-aminopropyltriethoxysilane (APTES). The nanoparticle were used to enhance the roughness of the surface. This assembly method produces a micron thick responsive polymer composite on the silicon substrate. Finally, all polymer grafts used in the following study were checked with contact angle analysis

and atomic force microscopy (AFM) topography. The surfaces were found to be consistent with previously reported characterizations.[30, 65, 97]

Structural changes in polymer composites can be triggered either by changes in temperature or addition of salts to solution. For these covalently bound layer-by-layer (LbL) polymer grafts switchable wetting behavior has been seen.[30, 97] Structural changes in this LbL graft cause the surface to transition from hydrophilic to hydrophobic. The Hofmeister series of salts, known for their ability to salt out proteins and polymers from solution, are used to induce these structural changes in the polymer graft.[70, 140, 141] By subjecting the surface to droplets of pure water or salt solutions containing either kosmotrophic or chaotropic salts from the Hofmeister series the wetting behavior changes (Figure 4.1). When exposed to the kosmotrophic salt the PNIPAM surface restructures; creating a hydrophobic surface with the hydrophobicity being enhanced by the presence of the silica nanoparticle in the PNIPAM creating surface roughness and trapping air between the liquid and solid interface. When chaotropic salt solutions are introduced to the surface, the surface remains hydrophilic. In fact, a slight haloing feature can be seen around the droplet. This is indicative of water entering the polymer film and by capillary action moving out along the surface hydrating the film beyond the area of direct contact.[142]

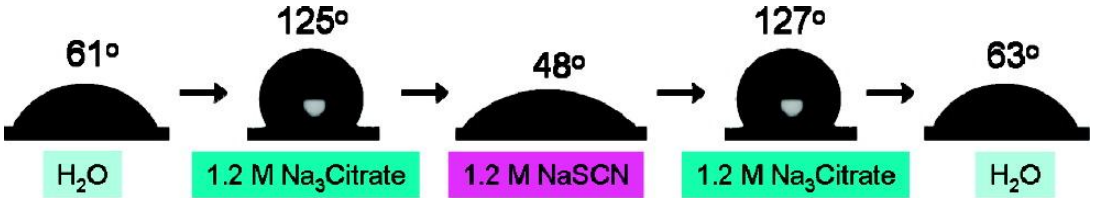

Figure 4.1. Contact angles of various solutions measured on a PNIPAM graft after 3 minutes. Reprinted with permission from Zhang, Y.; Furyk, S.; Bergbreiter, D. E.; Cremer, P. S. *J. Am. Chem. Soc.* 2005, 127, 14505. Copyright (2005) American Chemical Society.[62]

Switchable wetting as detected by contact angle analysis gives information regarding the entire exposed surface area. Using atomic force microscopy (AFM) the surface restructuring can be examined on a smaller scale. Images taken with an AFM give topographical information about the surface in its environment be it air or in solution. The LbL responsive surface used in this study has previously been studied in solution with an AFM, with a minor modification, the substrate was oxidized polyethylene. The surface restructuring can be seen in the topographical images of the polymer surface. While in air the polymer surface has a relatively high roughness factor of 287 nm (Figure 4.2a).[97] Once the polymer graft is submerged in water, the film swells as it absorbs water, leading to a smoothing of the surface (Figure 4.2b). When exposed to a kosmotrophic salt, Na_2SO_4, the PNIPAM has a phase transformation. This restructuring on the surface leads to a hydrophobic surface and the surface increases in roughness (Figure 4.2c). Since chaotropic salts allow for the polymer to remain in the extended coil state at room

temperature, the topography is comparable to the polymer graft in pure water (Figure 4.2d). This restructuring cycle was reproducible over several iterations.

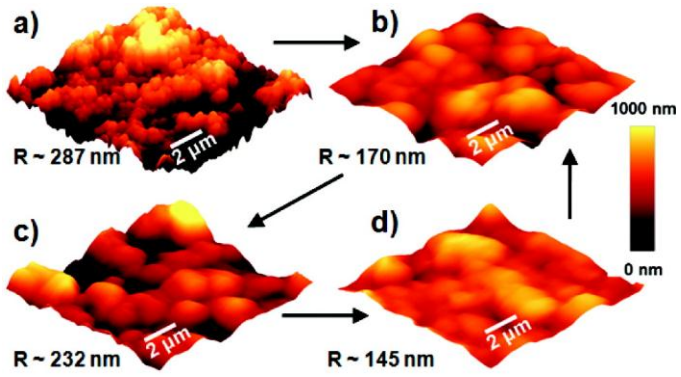

Figure 4.2. Tapping mode AFM images of PEoxid-(PNIPAM-c-PNASI/aminated silica nanoparticles) 6-PNIPAM obtained in (a) air, (b) water, (c) 1.4 M Na2SO4, and (d) 1.2 M NaSCN. Returning the sample to water yields a surface similar to (b). The average rms roughness of the surface in each environment taken from a random series of 2.5 µm × 2.5 µm regions is listed below each figure. Reprinted with permission from Liao, K. S.; Fu, H.; Wan, A.; Batteas, J. D.; Bergbreiter, D. E. Langmuir 2008, 25, 26. Copyright (2008) American Chemical Society.[97]

Temperature changes of PNIPAM brushes have been shown to effect the elastic modulus, the ratio of stress to strain.[31] As the temperature is slowly raised, the polymer transitions to the globular state, losing its water of hydration.[143] This transition increases the elastic modulus of the brush. Since this phase change is driven by the LCST, introducing salts to the system, instead of increasing the temperature, should result in a similar system response. This investigation focuses on changing the polymers' elastic

modulus by varying the temperature or by the addition of salts to the solution. Previous studies of PNIPAM brush structures have shown that the conformation and cross linking the polymer directly influences the Young's elastic modulus.[7, 31, 144] Cross linking the polymer chain in a grafted brush structure was shown to increase the mechanical stress to an applied load.[144] We show that the swelling behavior of the PNIPAM and nanoparticles composite grafts can be used to control the Young's elastic modulus of the surface.

Nanoindentation Method and Analysis

Nanoindentation allows for the measurement of the local hardness and the elastic properties of polymer films with thicknesses in the range of tens to hundreds of nanometers. Nanoindentation is done by taking force-distance (FD) curves and interpreting them using a contact mechanics model. Variations in the slope of force-distance curves yield information regarding the elastic modulus of the surface and, in some cases, changes in the surface chemistry indicated by changes in the adhesive properties. The elastic modulus was calculated using the Hertz contact mechanics model. The Hertz model is a simplistic contact mechanics model that assumes non-adhesive contact and measurements remain within the elastic limit. The Hertz model uses the indention of a probe, into the surface, compared to a reference standard, such as a silicon wafer, to determine the elastic modulus. Despite the simplicity of the Hertz model and its assumptions, it has been successfully used to model contacts between AFM probes and polymer substrates.[31, 69, 116]

Elastic modulus measurements were calculated from force-distance (FD) curves obtained using colloidal probe AFM. A silicon reference and the polymer composite were simultaneously held in a Plexiglas liquid cell, with a total volume of ~4 mL that was mounted to the AFM stage. A heating stage was used for temperature controlled experiments using a LakeShore 321 Autotuning Temperature Controller. All experiments were conducted after the AFM had sufficient time to equilibrate. The probe approach speed was set to 1 μm/s to control viscous drag on the cantilever. FD curves were taken with a range of 250 nm and acquisition of 500 points/curve.

Variations in the slope of force-distance curves yield information regarding the elastic modulus of the surface. The elastic modulus was calculated using the Hertz contact mechanics model.[31, 69, 116] The Hertz model uses the indention of a probe into the surface compared to a reference standard, silicon wafer, to determine the elastic modulus. The indention (δ) is determined at a set load (L) from the FD curves. The indention is related to the combined elastic modulus (K):

$$K = \frac{L}{(8\delta^3 R)^{1/2}}$$

Where R is the radius of curvature of the colloidal AFM probe. The combined elastic modulus is defined as:

$$K = \frac{4}{3}\left(\frac{1-\nu_t^2}{E_t} + \frac{1-\nu_p^2}{E_p}\right)^{-1}$$

Where ν_t and ν_p is the Poisson ratio of the tip and the polymer, respectively, and E_t and E_p are the elastic modulus of the tip and polymer. A value of 0.5 was used for the Poisson ratio of the polymer film. The assumption was made that the elastic modulus of the tip is far greater than that of the sample; therefore, these two equations were simplified to give:

$$E_p = \frac{3L(1-\nu_p^2)}{4(8\delta^3 R)^{1/2}}$$

The resulting elastic modulus values calculated were multiplied by a roughness parameter. The roughness parameter was a ratio determined by comparison of the calculated surface area above a cutoff threshold, determined by indentation depth, to the entire surface area of the AFM image. The roughness parameter accounts for the inhomogeneity of the surface yielding an incomplete contact between the polymer surface and the colloidal probe.

AppNano probes with 5 μm SiO_2 sphere were chosen because they allow for inherent averaging over a larger contact area versus traditional AFM tips. The normal spring constant was determined using the Sader method.[135] The radius of curvature for the colloidal probes was determined via reverse imaging of the probe on a standard TGT001 substrate (NT-MDT).[137] In addition to the inherent averaging by use of the colloidal probes, each force distance curve shown is the average of 20 unique individual measurements taken from various locations on the surface. The error bars for the elastic modulus values were obtained from 20 FD curves, in the same position on the sample, to eliminate error due to structural heterogeneities over the contact area.

Variations in Elastic Modulus Controlled by Temperature Changes

Temperature experiments were initiated at room temperature then raised to 40^0C over the course of an hour. The AFM was allowed to settle at the high temperature for 2 hours before measurements were taken. To cool the system, the stage heater was turned off; the warm water removed and replaced with room temperature water; and allowed to equilibrate for 2 hours.

It is known that PNIPAM films have variable elastic moduli dependent on their external environment.[31] The PNIPAM-*c*-PNASI composites have shown a variation in the elastic modulus from 10 to 100 MPa, when transitioning from room temperature (23^0C) to above the PNIPAM polymers' LCST (40^0C), shown in Figure 4.3. The increase in the elastic modulus is attributed, in part, to the collapse of the polymer matrix creating a denser polymer layer on the surface. It has been previously reported that in polymeric systems on porous frits, the polymer can take several hours to regain its extended coiled configuration after being exposed to temperatures exceeding the LCST.[65] Quartz crystal microbalance data indicates that it could take days or weeks for the polymer chains to return to their original conformation.[145] However, two hours after returning to room temperature the polymer surface has regained the elastic modulus presented below the LCST, indicating that the polymer film has recovered to a large extent within this time frame. These results show that the elastic modulus of the film can be controlled by temperature and this is a reversible process.

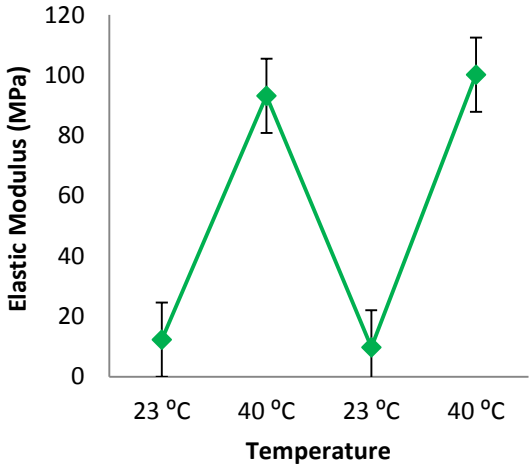

Figure 4.3. Young's elastic modulus values for the polymer composite below and above the LCST. Measurements were taken in the order shown. All measurement were of the same polymer composite.

Variations in Elastic Modulus Utilizing the Hofmeister Salt Series

Restructuring of the polymer film is due to the phase change of the polymer when the LCST is exceeded. When appropriate salts from the Hofmeister series are added to the solution, the LCST is dropped to below room temperature. Therefore when experiments are conducted at room temperature the polymer is in the collapsed state. It can be expected that the elastic modulus changes due to salts in solution will correspond to the changes seen with temperature.

Two experimental procedures were used to monitor the changes in the elastic modulus, based on rinsing procedures used when changing the salt solutions in the liquid cell. In the "THF rinse" cycle, the polymer substrate was rinsed, with 18 MΩ*cm water

for 30 seconds, ~8 mL of tetrahydrofuran (THF), and then dried under a nitrogen stream for 30 seconds, before emersion in the next solution. In the experiment, termed the "unrinsed" cycle, the liquid cell and sample were rinsed three times with the next solution in the series then filled for measurements under that solution.

In the various salt solutions, the slope of the FD curve is shifted in a predictable and reproducible manner, typical averaged retract curves are shown in Figure 4.4. The order of shifts for the averaged curves was consistent between several polymer samples and colloidal probes. Salts used in this investigation were chosen from each end of the Hofmeister series, results from these salts show the extremes in variation expected from using any salt in the series. The elastic modulus was calculated from average curves in water and salt solutions. The shift in the elastic modulus is due, in part, to the loss of water cushioning the probe when the polymer is in the collapsed state. Variations in the elastic modules were measured upon changes in the external solution environment and can be seen in Figure 4.5. Sodium sulfate increases the elastic modulus, compared to the value in pure water, whereas, sodium thiocyanate decreases the value. The highest elastic modulus can be seen with the "THF rinsed" sample in sodium sulfate. It has been shown that PNIPAM has a hysteric effect; by rinsing the surface with an organic solvent, the memory of the polymer can be "reset" as the organic solvent helps remove trapped ions and water from the polymer composite.[31] The elastic modulus change is significantly different between the "unrinsed" and "THF rinse" sample, supporting the claim that the THF rinse aides in removing unwanted ions and water molecules from the polymer

composite. The shifts in elastic modulus are expected, based on literature reporting elastic modulus dependence on temperature and polymers' LCST. An approximately 6-fold increase in the elastic modulus of plasma-polymerized N-isopropylacrylamide has been reported for the collapse of the polymer brush.[31] Our surface shows an order of magnitude increase in elastic modulus as a result of exposure to varying salt solutions. The incorporation of silica nanoparticles into the polymer matrix increases the elastic modulus above those reported in the literature for PNIPAM grafted surfaces.

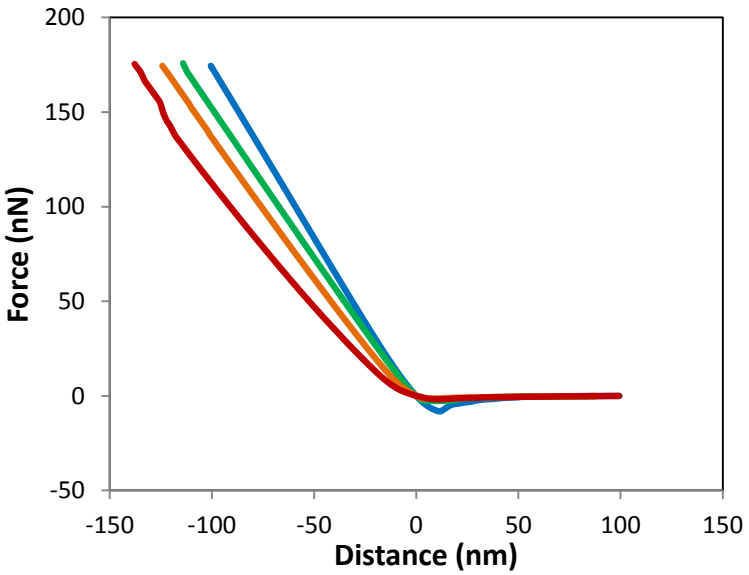

Figure 4.4. Averaged retract FD curves for a 5 µm SiO_2 probe on a Si wafer reference (blue) and the polymer composite in 1.0 M Na2SO4 (green), 1.0 M NaSCN (red), and highly purified water (orange). Curves shown are from a cycle using the THF rinsing procedure.

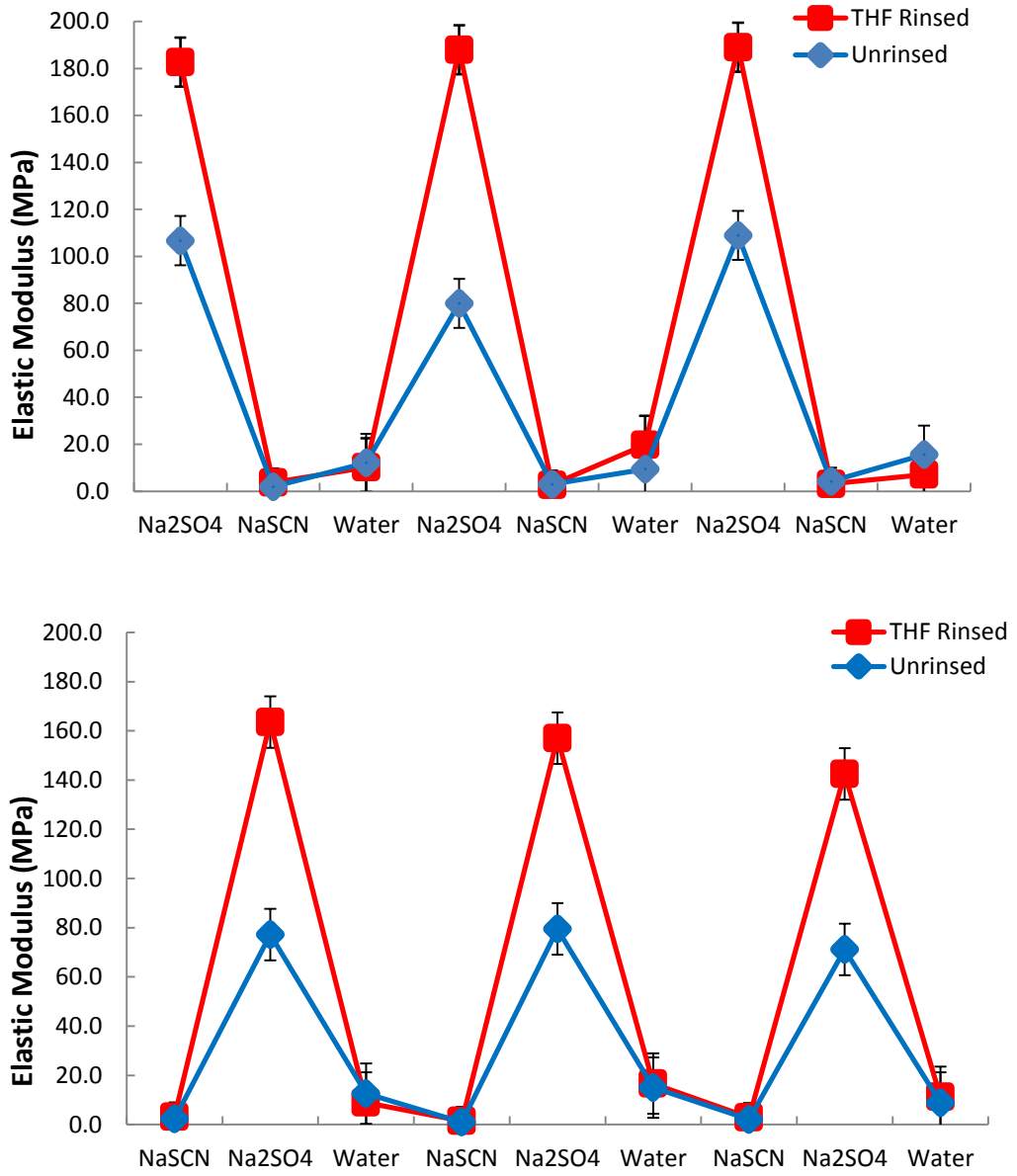

Figure 4.5. Young's elastic modulus calculated from 20 averaged FD curves. The cycle order in the top graph is 1.0 M Na_2SO_4, 1.0 NaSCN, and highly purified water; in bottom the order of the salts is reversed. Measurements were taken in the order shown on the same polymer sample.

Conclusion

Responsive polymers have many attributes that can be useful for modern technology. One of these attributes is the ability to change its elastic modulus via external stimuli. This has been shown for PNIPAM brush coated surfaces that have an elastic modulus change when the temperature of the sample is raised above the LCST.[31] Since this phase change is driven by the LCST, introducing salts to the system, instead of increasing the temperature, results in a similar system response. The higher elastic modulus in our sample compared to those in the literature are attributed to the confinement of the polymer in the layer-by-layer system and the inclusion of silica nanoparticles. We have shown that a layer-by-layer responsive surface composed of PNIPAM exhibits a change in modulus over a range of 180 MPa when immersed in salt solutions.

CHAPTER V

GRAVIMETRIC SEPARATION OF HEXADECANE IN WATER EMULSIONS UTILIZING A "SMART" POLYMER COMPOSITE FUNCTIONALIZED POROUS FILTER

Overview

An oil and water separation filter has been developed incorporating the "smart" polymer poly(*N*-isopropylacrylamide) (PNIPAM). The porous silica frit was functionalized using layer-by-layer assembly with the electrophilic smart polymer PNIPAM and nucleophilic silica nanoparticles. Frits modified with the PNIPAM/SiO_2 composite have recently be utilized for flow rate control due to the swelling behavior of PNIPAM which is sensitive temperature and to the identity and concentrations of solute anions. Here we show that the polymer composite functionalized frit shows superhydrophilicity and oleophobicity extending its applications to oil water separations. In gravity driven separations water is permeable through the frit while the oil phase will remain above the frit. Complete demulsification of water-hexadecane and simulated ocean water-hexadecane emulsions can be achieved in minutes on a milliliter scale.

Introduction

The development of economical and environmentally friendly oil-water separation methods has become an urgent issue.[146, 147] The discharge of oily waste water streams from

industry and frequent oil spills, such as Deep Water Horizon in the Gulf of Mexico, organic pollution of global water sources has emerged, and is negatively affecting ecosystems, human health, and economic growth.[148-150] Twenty-six months after the Deep Water Horizon spill and cleanup efforts, there are detectable levels of the chemical dispersant used found in near-by deep sea coal communities and gulf coast beaches.[151] This dispersant was thought to undergo rapid degradation in the ocean water column; unfortunately this has been shown not to be the case. This experience among other cleanup events has increased the desire for an environmentally friendly and low cost separation methods.

Oil-water separations, especially in the presence of surfactants, have proven to be difficult and better methods are desired for their effective cleanup.[152, 153] Oil in waste water can take several forms defined primarily based on droplet size: free (>150 μm), dispersed (20-150 μm) or emulsified (<20 μm); each form has its own inherent problems for separation.[154] The conventional method for treatment of oily water includes gravity separation, skimming, dissolved air floatation, coagulation and flocculation.[154, 155] While commonly used to treat free oil in water, gravity separators and skimming techniques are incapable of demulsification; the conversion of an emulsion to a free oil in water.[154, 155] Emulsions are commonly pretreated chemically to destabilize them before further processing is completed which can be time intensive and costly. Oil and water separation methods have been further developed in the past several years using a variety of platforms including sequestering nanoparticles, absorbents and membranes.[120, 149, 150, 156-159]

Membrane-based demulsification technology is attractive since it has shown to be energy-efficient, cost-effective and widely applicable.[160]

When designing a filtering membrane, there are several design aspects that must be considered: porosity, permeability, hydrophobicity, oleophobicity, and breakthrough pressure.[146, 147, 153, 155] Separation membranes can be generally divided into the following classes: oil removing, water removing, and smart controlled separation materials.[120, 161-163] Ideally for water removing gravity driven separations the membrane would be hydrophilic and oleophobic; this is desired since water will naturally settle against the membrane due to its higher density. The difficulty in designing these membranes is while in air the membrane may be oleophobic, once submerged in water this property may not be retained.[164, 165] Even if the membrane is oleophobic, it may possess a small breakthrough pressure which will allow the oil phase to be driven through the membrane due to high pressure exerted by the column of fluid above the membrane.[155] Smart controllable separation materials have the added benefit of being controlled either internally or externally by a stimuli; this control can reduce energy consumption, regulate flow rates and aide in material recovery.[157, 158, 166, 167]

Recent years have seen a growth in the development of oil water membrane separation technology, each exhibiting advantages and disadvantages. Lui and coworkers have developed a reversible superhydrophobic-and-superhydrophilic separation mesh by coating a copper mesh with a self-assembled layer of stearic acid.[168] The properties of this switchable surface were controlled by soaking the mesh for 5 minute in a solution of

either stearic acid or tetrahydrofuran. This membrane allows for the user to decide which phase to allow through the membrane by controlling the chemistry of the presoaking solution. While it is useful to control the permeable phase, presoaking requirements are not desirable. Recently the Wei group from Tsinghun University developed a dual-responsive membrane based on the smart polymer poly(dimethylamino ethyl methacrylate).[120] When this polymer was coated onto a stainless steel mesh, controllable separation of a gasoline and water mixture was achieved. Below a set temperature and pH value only water would permeate the mesh; if the temperature or the pH exceeds these values the gasoline will also permeate the mesh. The advantage of this method is the ability to allow the gasoline to controllable permeate the membrane instead of the removal of the separate phase from above the membrane. The two methods discussed thus far have utilized metal meshes as their substrate, but substrates can be composed of other materials such as cellulose and porous silica. A tunable unidirectional flow diode has been developed utilizing Scott paper towels from the Kimberly-Clark Corporation.[169] The separation diode was generated by spray coating one side of the paper towel with a combination of hydrophilic bentonite nanoclay and fluoroacrylic copolymer. Interest lies with generating environmentally friendly separations membranes which are controllable and composed of durable materials. Advances in this have been made using polymer functionalized membranes.[170]

This chapter explores the use of porous silica filters functionalized with the stimuli-responsive poly(*N*-isopropylacrylamide) (PNIPAM) for the gravimetric

separation of oil and water mixtures. Poly(*N*-alkylacrlamide)s are one of the most studied types of stimuli responsive polymers with a range of applications including self-cleaning, sensors, drug-delivery and microfluidics.[7, 47, 171-174] PNIPAM is of particular interest for its lower critical solution temperature (LCST) at 32ºC, when the polymer reversibly transitions from hydrophilic to hydrophobic.[34, 41] At the LCST a polymer exhibits a phase change such that the polymer is no longer soluble. The LCST of PNIPAM can be greatly affected by salts in solution; the effect of these salts is determined by the position of the salt in the Hofmeister series.[23, 32, 60, 62] Salt effects on the LCST temperature can be of great concern when using PNIPAM coated membranes for oil and water separations in marine environments which can have relatively high salt concentrations. Additionally, PNIPAM has been shown to collapse in the presence of oligomers.[175, 176] The collapse of PNIPAM at the water-oil interface is a desirable response for the design of separation membranes utilizing porous silica substrates. Smart polymers grafted to porous materials may be used to control fluid permeability by controlling the surface wettability and pore openings.[170, 177]

A substrate of considerable interest is porous material, with pores in the range of nanometers to microns. Size controlled pores can be etched into poly(ethyleneterephthalate) (PET) membranes and subsequently functionalized with a polymer to generated flow rate controlled membrane.[178] The PET was track-etched functionalized with a PNIPAM polymer brush using both free radical polymerization and atom transfer radical polymerization. It was found for pores larger than 330 nm

permeability was hindered by the hydrated chains occupying space in the pore. In the case of large pores, the membrane was more permeable above the LCST when the chains were collapse therefore occupying less space within the pore cavity; while for small pores on the order of 80 nm the hydrated PNIPAM chains lowered the permeation rate compared to the unfunctionalized surface, but when the temperature was raise the polymer chains collapse and completely obstructed flow through the pore. The temperature controlled obstruction of the pores allowed for switchable flow rates.

Utilizing the ideas of controlling the flow rate through a porous membrane with polymer chains, Allen et. al. developed a surface functionalized porous filter stop light based on the previously described a methodology for the synthesis of covalently bound layer-by-layer assemblies incorporating a stimuli-responsive polymer, PNIPAM, and silica nanoparticles on glass.[30, 65, 83, 97, 179] The medium porosity (10 – 20 μm pores) glass frits were functionalized utilizing LbL assembly to examine the use of LbL on complex substrates. The functionalized frits were then used for controllable flow rate studies. It was shown that frits functionalized with the responsive polymer where hydrophobic when exposed to kosmotropic salts from the Hofmeister series, while they were hydrophilic when exposed to chaotropic salt solutions at room temperature. When the modified frits were subjected to variations in salt concentration the passive permeability had a depression as great as 1000 fold for high concentrations of kosmotropic salts.[65] A combination of the physical response to the polymer occupying space in the pores and the chemical repulsion

of water molecules by the hydrophobic surface controls the flow rate through the functionalized surfaces.[177]

In this work, PNIPAM/nanoparticle grafts have been extended to incorporate studies involving the separation of hexadecane and water solutions. The hydrophilicity and oleophobicity of the grafts were first examined; then separations varying from free oil and water to emulsions using only gravity as a driving force were studied.

Functionalization of Glass Frits by Covalent Layer-by-Layer Assembly.

This functionalization of frits procedure was modified from the surface grafting procedure of polyethylene films and discussed extensively in Chapter III.[30, 65, 97] This method relies on the use of layer-by-layer assemble, a process in which to build up robust surfaces by alternatingly exposing the surface to electrophilic and nucleophilic solutions. Briefly, the cleaned silica frits were first functionalized using 3-aminopropyltriethoxysilane to allow for covalent attachment of the responsive polymer to the surface. After amination of the surface a total of nine bilayers were grafted to the substrate. The first two bilayers were composed of an electrophile, poly(*N*-acryloxysuccinimide) (PNASI), and nucleophilic polyethylenimine (PEI); unreacted active ester groups from the PNASI were quenched with isopropylamine. The following six bilayers incorporated a polymer that gives the surface its responsive nature. These bilayers were grafted by alternating the polyvalent electrophile PNIPAM-*c*-PNASI with a nucleophilic mixture of 10 and 100 nm aminated silica nanoparticles (only 10 nm particles were used for the 6th bilayer) suspended in a solution of dimethylformamide. After

grafting a bilayer unreacted esters were quenched with a primary amine. This was followed by grafting of a capping layer utilizing only the polyvalent electrophile and the primary amine allowing for surface termination with the responsive polymer. The finished functionalized frits were shaken three times in a water bath then fitted into a Teflon chromatography column to tubing adapter (ACE #5838-91) which was secured to a 15 mm i.d. column (ACE #7644-15). Once in the chromatography column, the frits were washed by passing ~50 mL of water and ~30 mL of methanol through the frit and then were dried under flowing nitrogen overnight.

Wettability

It has been previously shown that the incorporation of silica nanoparticles in the responsive polymeric graft grown on a silicon wafer leads to a topographically complex surface which enhances the controlled wettability. Extensive characterizations of the wettability of these polymer nanocomposite grafts including responses to temperature and aqueous solutions have been reported.[30, 65, 97] Wettability properties were assessed by measuring the contact angle of water, salt solutions and hexadecane on a surface. The contact angle can be simply defined in by the Young's equation:

$$0 = \gamma_{SG} - \gamma_{SL} - \gamma_{LG} \cos \theta_C$$

In Young's equation variations in the surface tension (γ) are used to rationalize the contact angle at equilibrium. The surfaces used for this study had similar solute responsive

wettability compared to the previous studies. Of interest for this work is the grafts' responsiveness to oligomers.

A goniometer is used to measure the contact angle between the droplet and the surface. This is accomplished by taking high speed images of the drop. The CAM 200 software defines the edge of the drop by variances in pixel color and graphically solves for the contact angle. In this study a micropipetter was used to deliver droplets of solution to the surface due to the high affinity of hexadecane to the metal needle normally affixed to the goniometer.

Initially probed was the surfaces' responsiveness to salt solutions to test for successful functionalization. A drop of water or 1.0 M Na_2SO_4 was placed on the frit surface; in this case the water is absorbed but the sodium sulfate drop remains above the frit. This confirms the newly synthesized surface was successfully functionalized and complies with previous results for flow regulated surface functionalized frits.[65] For oil-water separation membranes a surface that is hydrophilic and oleophobic is desired. To determine the oleophobicity of the surface, hexadecane was used as a model oil. For the unfunctionalized frit, drops of both water and hexadecane were rapidly absorbed (Figure 5.1 A&D). As expected, when a 10 µL drop of water was delivered to the surface of a functionalized frit, it was absorbed into the porous structure (<10 s), independent of whether the frit was dry or previously wetted with water (Figure 5.1 B&C). When a 10 µL drop of hexadecane was delivered to the surface of the functionalized frit, it remained above the surface, giving a static contact angle of 83.1º (Figure 5.1E) and 102.3º on a

prewetted surface (Figure 5.1F). The lack of hexadecane adsorption into the surface and having a contact angel of above 90º is indicative of an oleophobic surface.

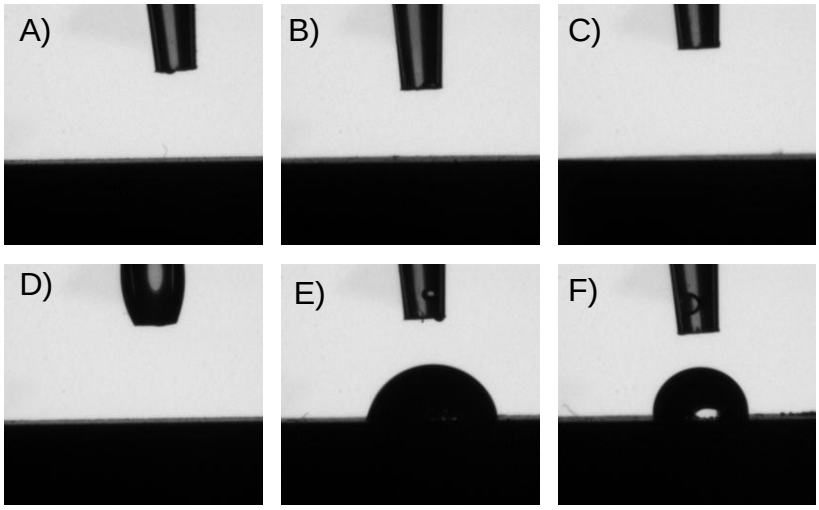

Figure 5.1. Contact angle images shown 20 seconds after 10 µL drop placement. A) Water on an unfunctionalized frit. B) Water on a dry functionalized frit. C) Water on a functionalized frit that was prewetted with water. D) Hexadecane on an unfunctionalized frit. θs is 83.1º. E) Hexadecane on a dry functionalized frit. F) Hexadecane on a prewetted frit. θs is 102.3º.

Flow Rate Measurements

Based on the preliminary studies of droplet behavior using contact angle analysis, I began a study of the oleophobic solute responsive permeability of frits functionalized with the responsive polymer graft. The passive permeability of the modified frit was tested with water, simulated ocean water and the model oil, hexadecane. These tests involved

measuring the volume change of the solution retained above the frit over a period of time. A functionalized frit was inserted into a chromatography column with a tubing adapter affixed to the side for liquid level measurements. The solution of interest was added to the column and allowed to filter through the frit. Initial experiments showed inconsistent results between tests due to poor cleaning of the frits using the previous cleaning procedure developed when using salt solutions to control the flow rate.[65] Changes to the cleaning procedure included initially shaking a ~10 ml aliquot of tetrahydrofuran (THF) in the column assembly followed by an aliquot of ethanol. The setup was then cleaned following a similar procedure as before where ~50 mL of pure water was allowed to filter then ~25 mL of ethanol. The frit was subsequently dried with flowing nitrogen for several hours to overnight. This modified procedure was followed between all tests regardless of whether the test involved hexadecane. Use of this cleaning procedure between tests led to more constant and reproducible results. During the experiment, the volume change at specified times for up to 24 hours was recorded to determine flow rates. The filtrate was captured for additional analysis. After the study was concluded the remaining solution above the frit was discarded. The frits were then washed to remove any oil fouling the system and to return the responsive polymer back to its original configuration. All studies were conducted above 20°C, the freezing temperature of hexadecane. All flow rates reported here were taken from one individual frit to allow for comparison. Slight variations from frit to frit are normal and were attributed to differences in the extent of functionalization and pore distribution.

Neat Solutions

Initial attempts for oil-water separations were carried out with neat solutions. In these experiments the column above the frit was first filled with 10 mL of water then immediately 10 mL of hexadecane and the total volume in the column as well as the phase line was tracked through the duration of the experiment. As shown in Figure 5.2A, the water permeated the filter within ~15 minutes from the introduction time while the oil phase remained above the frit for up to 24 hours. The oleophobic and hydrophilic frit is able to separate the phases with no viable oil being retained in the filtrate. Figure 5.2B shows that when the introduction order is reversed, the frit shows only slight changes in retention time.

In addition to separation of pure water and hexadecane, separations of simulated ocean water and hexadecane were explored. Using the American Society for Testing and Materials procedure D1141; simulated ocean water was produced, excluding the heavy metals which are found to be less than 0.1 ppm. The solution contained the following salts in decreasing concentrations: sodium chloride, magnesium chloride, sodium sulfate, calcium chloride, potassium chloride, boric acid, strontium (II) chloride, and sodium fluoride (Table 5.1). The pH was adjusted to 8.2 using sodium hydroxide. Using the same experimental procedure, the separations of simulated ocean water and hexadecane were comparable to those of pure water (Figure 5.3). The PNIPAM polymer used to functionalize the frit is a stimuli responsive polymer that is known to restructure when exposed to the kosmotropic ions from the Hofmeister series of salts. This restructuring

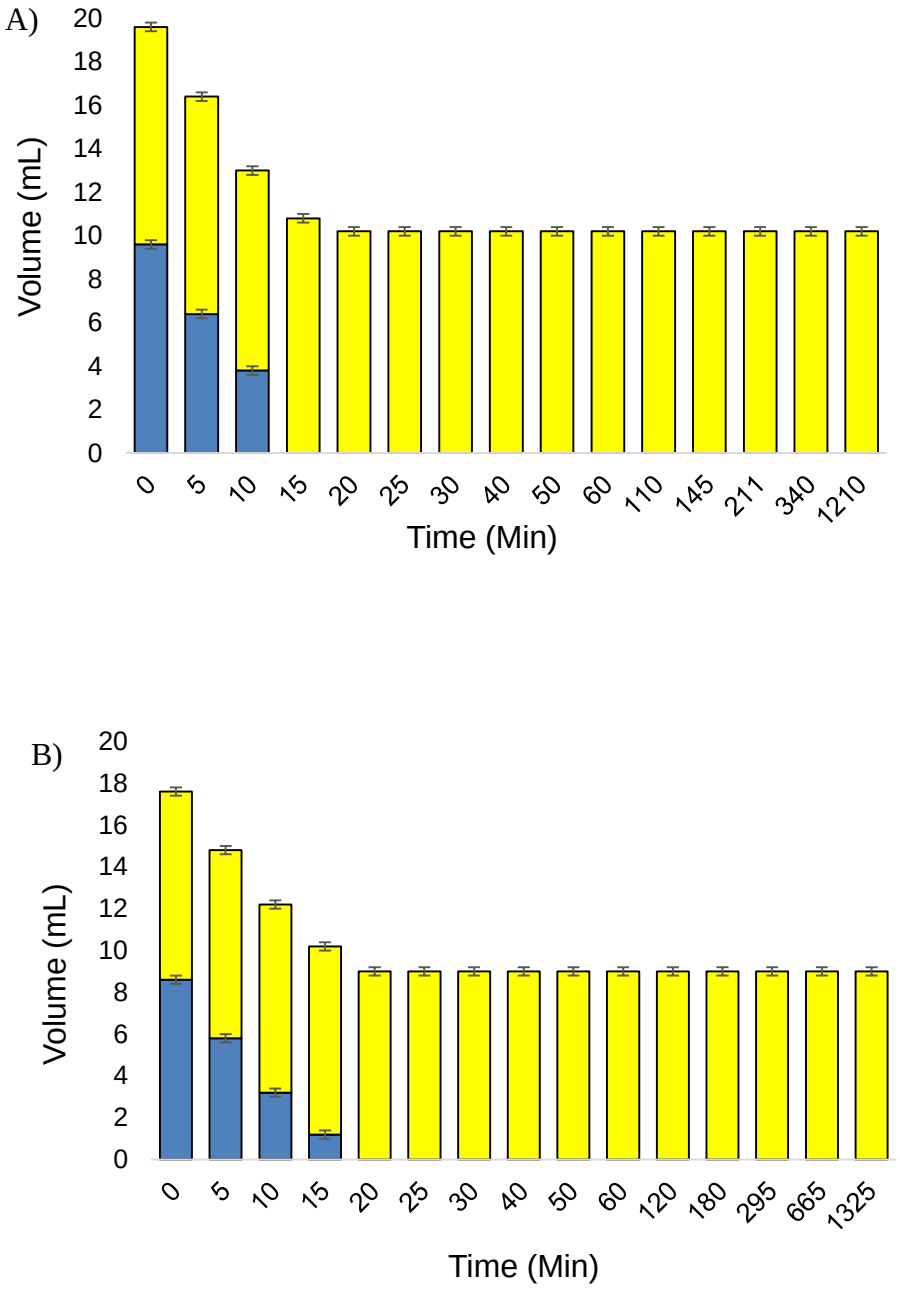

Figure 5.2. Separation of neat pure water and hexadecane samples. The volume of water is shown in blue and hexadecane in yellow. A) Water was added to the system first. B) Hexadecane was added to the system first. Error bars represent volume measurement error.

when using salt solutions is the driving mechanism for the flow rate controlled filters we first reported in 2009.[65] Therefore it was a concern whether these frits would function under simulated marine conditions. This initial study shows that at least for simulated marine environments these frits can be implemented. This could extend their viability from civilian water treatment plants to environmental remediation applications.

Compound	**Concentration (g/L)**
NaCl	24.53
$MgCl_2$	5.a
Na_2SO_4	4.09
$CaCl_2$	1.16
KCl	0.695
$NaHCO_3$	0.201
KBr	0.101
H_3BO_3	0.027
$SrCl_2$	0.025
NaF	0.003

Table 5.1. Salt identity and concentrations used to make simulated ocean water.

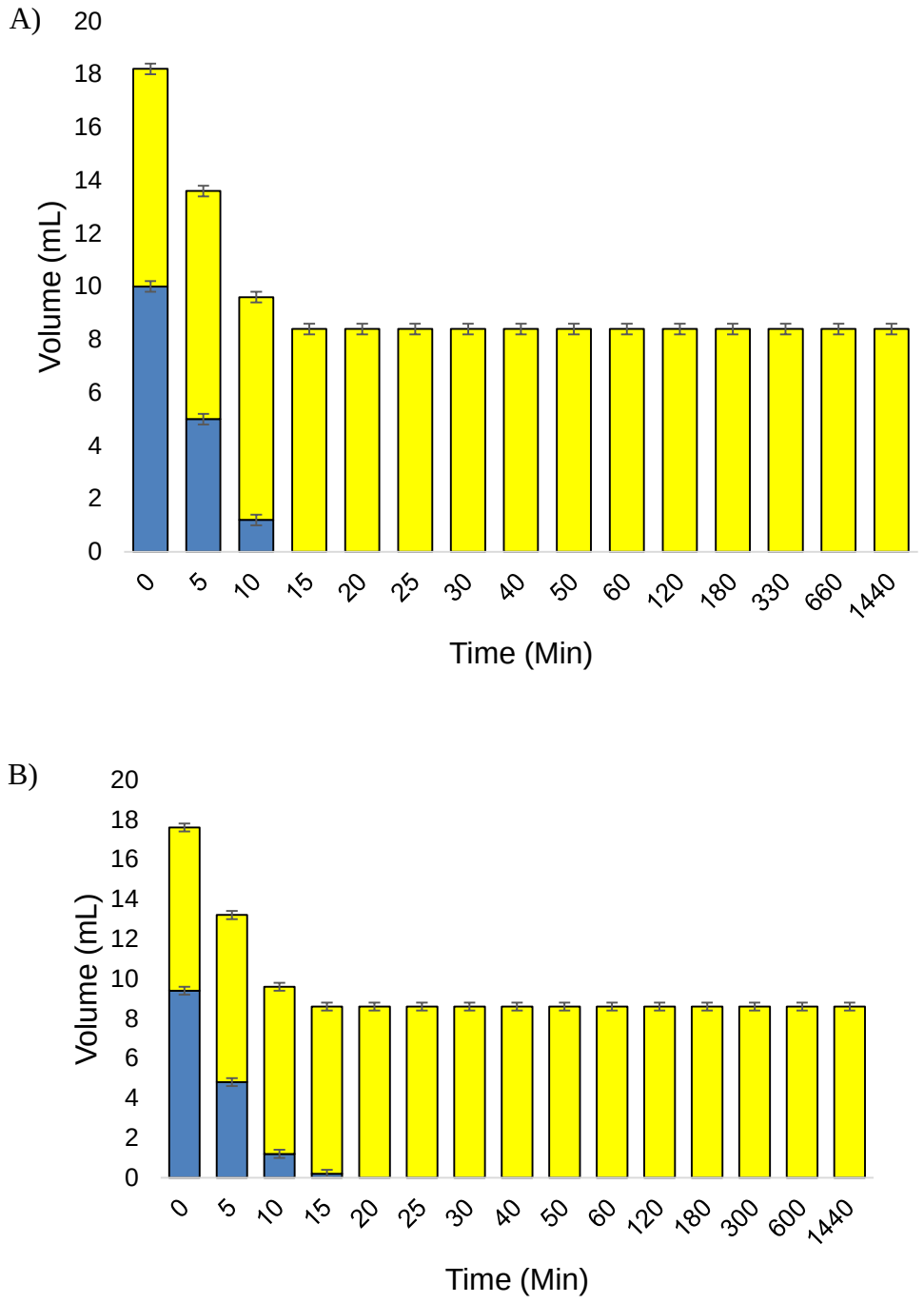

Figure 5.3. Separation of neat simulated ocean water and hexadecane samples. The volume of simulated ocean water is shown in blue and hexadecane in yellow. A) Simulated ocean water was added to the system first. B) Hexadecane was added to the system first. Error bars represent volume measurement error.

Emulsions

While useful, separations of neat solutions are simple compared to separations of stabilized water and oil emulsions. While many membranes have been explored for separations of neat solutions, few have explored separations of emulsions. The separation of emulsions requires a selectively permeable membrane that has non-fouling capabilities. In many emulsion separations the emulsifier can foul and block pores in the membrane preventing further penetration. In this study emulsions of hexadecane and water (or simulated ocean water) were utilized. Using a reported procedure, emulsions of hexadecane and water were made to be 50% (v/v) hexadecane in water with 2.8 mM sodium dodecyl sulfate as the stabilizing surfactant.[155] Emulsions were characterized by optical microscopy. These emulsions were characterized and showed optically visible micelles in the range of 1 μm to 50 μm. An optical image of the stabilized emulsion is shown in Figure 5.4. By dyeing an aliquot of the emulsion with Nile Blue it was found that water is the continuous phase.

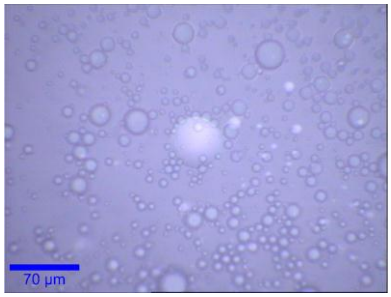

Figure 5.4. Optical image of 50% (v/v) hexadecane in water with 2.8 mM sodium dodecyl sulfate, showing droplets ranging from submicron to 50 μm in diameter.

For separation studies of the emulsions, a fresh emulsion was made the day before and allowed to stir overnight. This was then added to the column above the frit. In this case, unlike the neat solutions, only the total solution volume was tracked since no solution phase line existed (Figure 5.5). The slight separation time difference between the pure water and simulated ocean water emulsions can be attributed to the salts in solution effecting the configuration of the PNIPAM and slowing the flow rate. The sodium chloride concentration in the simulated ocean water is around 0.4 M; which at this concentration has shown to decrease the LCST of solution phase PNIPAM by near 2ºC. It is important to note that the total volume of water recovered was not always 100% of the initial amount. This indicates that some of the water is still trapped in the emulsion above the frit, therefore the oil phase is not pure. While the filtrate has little to no hexadecane, not all of the water has retreated from the oil. For most applications, the recovery of the water phase is the goal; therefore the retention of up to 10% of the initial volume of water in the oil as seen here may not be a problem. If needed there are several methods that can be employed to dry the oil including desiccation or heating.

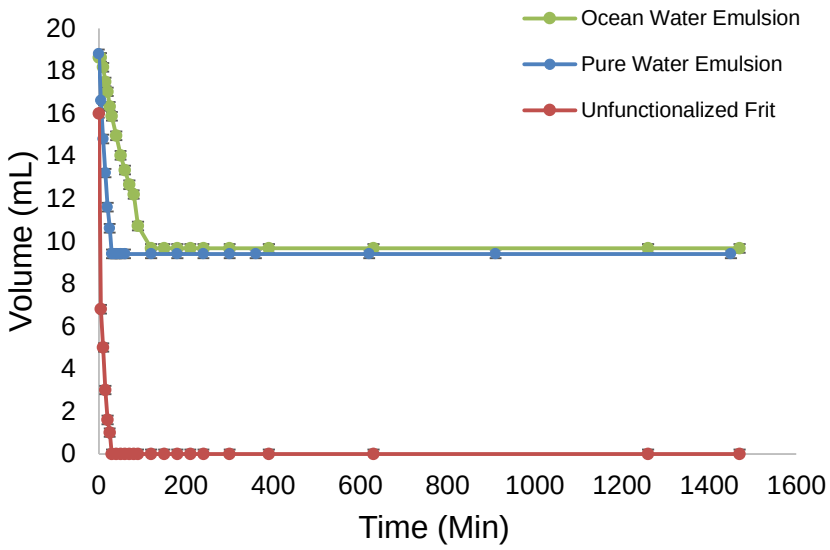

Figure 5.5. Time study for the demulsification of water-hexadecane (blue) and simulated ocean water-hexadecane (green) compared to an unfunctionalized frit (red). Measurement error bars are smaller than the markers shown.

Post Filtration Analysis

As the separation proceeded (water; neat layered mixture of hexadecane and water; 50% (v/v) hexadecane in water emulsion; simulated ocean water and oil mixtures) the filtrate was captured with no visible signs of the oil in the water. Solvent extraction of the filtrate with hexanes was used to sequester any hexadecane in the filtrate. Subsequent analysis of the filtrate by GC-MS shows that trace amounts of hexadecane were contained within the filtrate. Using an internal standard, hexadecane was found to be less than 10 ppt in the filtrate. This is well within the range of hexadecane solubility in water.

Conclusion

Covalent layer-by-layer smart polymer grafts were successfully used to carry out oil-water separations. The functionalized frit shows hydrophilic and oleophobic natures which are desired for gravity driven separations of oil-water mixtures. Demulsification of water-hexadecane and simulated ocean water-hexadecane was achieved in under 120 minutes with no or trace hexadecane permeating the membrane. The separations proceeded with a high selectivity to the water permeate having a purity of greater than 99.9%. In addition, the frits showed no irreversible fouling from the oil phase using the described cleaning procedures. These frits show promise for environmental remediation of oil spills with low energy consumption.

CHAPTER VI

SMART POLYMER GRAFT SUMMARY AND FUTURE OUTLOOK

Summary

Stimuli responsive surfaces functionalized using the layer-by-layer (LbL) assembly method were generated on silicon wafers and porous silica frits. The LbL assembly method relied on alternatively exposing the surface to electrophilic and nucleophilic species to build the surface up one layer at a time. The major electrophile used was the thermoresponsive copolymer, poly(*N*-isopropylacrylamide)-*c*-poly(*N*-acryloxysuccinimide) (PNASI-*c*-PNASI). The NASI groups facilitate the covalent binding of the nucleophilic species to the surface. The NIPAM groups impart responsive behavior to the film. The major nucleophilic component of the system was aminated silica nanoparticles in a mixture of 10 and 100 nm. The silica nanoparticles were used for two main reasons: first as a functional chemical species' nucleophilic counterpart and second to impart roughness into the polymer film. Previous studies have shown that these surfaces have controllable wetting behavior and complex topographical reconstruction when exposed to conditions what alter the polymers' conformation.[30, 65, 83]

At the lower critical solution temperature (LCST) the NIPAM groups dehydrate and the polymer chain becomes insoluble in solution. In solution the LCST for PNIPAM is 32ºC.[101] When the thermoresponsive polymer PNIPAM is grafted to a surface it has

controllable wetting behavior. Adding silica nanoparticles to the graft increases the dynamics of the wetting behavior allowing for a man-made mimic of the naturally occurring lotus leaf.[64] The conformation changes in the surface wetting and topography were well establish. This dissertation probed the tunable Young's elastic modulus of the surface trigger by the polymers restructuring. Nanoindentation was used to measure the Young's elastic modulus of the surfaces submerged in pure water, 1.0 M NaSCN and 1.0 M Na_2SO_4. The elastic modulus was found to exhibit a range of 180 MPa dependent on the surrounding solution and the rinsing steps. To confirm the change in elastic modulus was due to restructuring of the surface induced by the presence of salts effecting the LCST, nanoindentaion measurements in pure water were taken at room temperature and at 40ºC, which is above all reported LCST transitions for supported PNIPAM. The elastic modulus was found to range between 10 and 100 MPa based on temperature changes alone. The change in elastic modulus is attributed to the loss of water hydrating the polymer chains and the restructuring of the surface. The overall hardness of the surface is significantly increased compared to literature values for PNIPAM on the surface due to the incorporation of silica nanoparticles.

When the PNIPAM/SiO_2 nanocomposite is grafted onto porous silica frits it can be utilized for flow rate control as shown previously or for oil and water demulsification. Successful functionalization of the frits was confirmed by comparison of the flow rates of pure water and 1.0 M Na_2SO_4.[65] The flow rate of the sodium sulfate is at least three orders of magnitude lower than the rate for water. This is due to the PNIPAM graft restructuring

preventing fluid flow. Of interest here was the separation of oil and water mixtures. For this study the model oil used was hexadecane. The frits were fitted into the base of a chromatography column and the solution mixture to be separated was added to the column above the frit. At room temperature pure water and simulated ocean water were capable of passing through the porous membrane, but due to PNIPAMs oleophobic nature the hexadecane was sequestered above the frit. Separation of layered and emulsified solutions were investigated. In total for the separation of 20 mL of emulsified simulated ocean water and hexadecane solution took around 2 hours, with this being the slowest case scenario tested.

Outlook

Surfaces grafted with thermoresponsive material have a great propensity for growth. For their continued used the physical and chemical properties and manufacturing techniques need further exploration. For example, while the layer-by-layer polymer systems studied here are chemical robust thanks to the covalent bonding, but they are physically very delicate surfaces. Smart polymer surfaces have potential applications in a verity of fields each with its own unique set of fabrication and functional requirements. The approach for designing responsive drug delivery systems will be vastly different from medical implants even though both of these applications are contained within the medical field.

If the responsive surfaces are to be used as functional coatings, their behavior under applied loads must be understood. As just mentioned these surfaces are physically

delicate. The ability of the surface to withstand frictional wearing forces is directly related to their applicability. The frictional forces are affected by two major factors, the chemistry of the surfaces and the roughness of the contacting surfaces.[180, 181] The effect of roughness change on the frictional response on a small scale can be monitored via lateral force microscopy. For larger scale a tribometer can be used, although it is not expected for the current films of interest to withstand a large sliding force.

Many applications exist for smart surfaces and the more functions the surface has the more applications it lends itself to. PNIPAM surfaces have been shown to have controllable wettability, topography, and elastic modulus that can be triggered by temperature and salt solutions.[30, 31, 97, 179] Additional functionalities can be added using two major routes. The first method involves using different external stimuli to elicit a new response. The second method is by addition of responsive species either to the polymer chain or by exchanging the layer-by-layer components.

Thus far the result presented within this dissertation have utilized temperature, salt solutions, and oligomers to effect the LCST of PNIPAM grafts. Multiple studies in the literature explore the effect of cononsolvency on PNIPAM.[69, 106, 139, 182, 183] The cononsolvency effect occurs when two good solvents are mixed, in a specific ratio, resulting in a poor solvent for the polymer. In some cases, with these cononsolvent mixtures an increase in adhesion is seen.[69] The cononsolvency effect potentially allows for the addition of an adhesive functionality for the responsive surface. Although,

preliminary results indicate that the cononsolvency effect is not effective for the LbL system, this is speculated to be due to high crosslink density in the graft.

Additional graft properties can be added by copolymerizing two separate responsive monomers or by using two responsive species as the alternating components of an LbL system. Additional functionalities could include but are not limited to: color transitions, light responsive, electrical switching, and florescent sensing.[184-186] The combination of temperature and electrical switching could yield great potential in the field of electronic devices. The addition of azobenzene side chains to poly(vinyl alcohol) surface grafts allows for wettability switching when exposed to UV light.[186] The area of the monolayer increases as the azobenzene side chains change from the trans to cis with exposure to UV light.[186] The Theato group has developed a light, temperature, and redox multi-responsive polymer for polymeric information processing applications.[186, 187]

Smart polymer grafted porous material have the propensity for more than fluid control and emulsion separations. Smart polymers are currently being looked at for use in size exclusion chromatography.[188] This has the potential to separate molecules and perhaps ions based on size. At this point in time, only salt solutions containing a single salt have been studied allowing for flow rate control. Of potential interest is the separation of a mixture of chaotropic and kosmotrophic ions in solution, with only the chaotropic ions penetrating the polymer graft. If this should work, it could be used to recover and concentrate high value ions from solutions such as industrial waste or sea water.

For LbL assembly to be a widely accepted and viable manufacturing technique in a large industrial setting the assembly method needs to move from a dip coating process to a more streamlined process. This can be achieved by spray coating each layer component. Spray coating has its own unique challenges for homogeneous layers several factors must be controlled including: distance from the nozzle to the surface, droplet size, polymer concentration, solvent mixture, *etc*.[88, 89, 91, 189, 190] These conditions will change with every polymer system utilized.

CHAPTER VII

USING MODEL CATALYST SYSTEMS TO IMPROVE "REAL WORLD" CATALYST

Introduction

Certain chemical species alter a reaction pathway, without itself being consumed; these are termed catalysts. Pioneering studies on catalysts involving sugar fermentation and oxidation of ethanol began in the early 1800's with the work by Mitscherlic and Berzelius.[191] By the 1840's catalysts began to be heavily studied. With the introduction of Langmuir's checkerboard model of adsorbents on the surface and increase in analytical techniques to probe the surface, the interest in modeling catalyst systems grew.[1, 192] The large growth and development of surface characterization techniques starting in the 1960s resulted in an explosion of research into the complex nature of catalysts. New techniques allowed for the study of the physical and chemical structures of industrial grade catalyst and for catalytic studies on clean single crystal surfaces. This has led to the demand for more high-preforming catalysts that employ multimetallic and supported systems.

There are two major approaches to studying catalyst systems; the study of industrial grade supported catalyst or model supported catalyst systems as depicted in Figure 7.1.[1] Industrial or "real world" catalyst are typically supported on amorphous oxides or carbon; with some level of heterogeneity in structure and size of the supported catalytically active species. These systems can be investigated using a verity of surface

sensitive techniques; but fundamental knowledge of the catalytic mechanism may be hard to extract from this information. This has led to catalytic studies on model systems. In model systems there is precise control of the support layer and the size and concentration of catalytically active species on the surface; however, these studies must be conducted at very low pressures to maintain a clean surface. Surface science investigations of model catalysts allow for systematic surface property reactivity correlations. Strategic use of well-characterized mono- and bimetallic model catalysts have provided atomic-level information on homogeneous catalysis involving transition metals. Using model systems the sequence of steps that occur during catalyzed reactions can be studied; including adsorption, diffusion, chemical rearrangement, and desorption.[1]

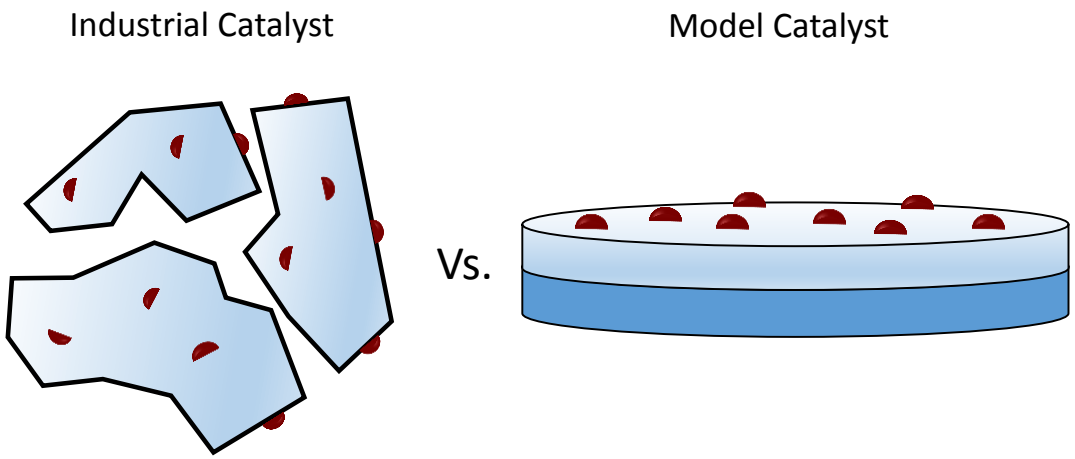

Figure 7.1. Depiction of an oxide supported metal catalyst as seen in industry (left) and the model catalyst system used for catalytic design (right).

The study of model catalytic systems is not without complications. The first is termed the "pressure gap".[193] For many of the analytical surface science techniques pressures below 10^{-6} torr are needed, which is several order of magnitude below industrial operating pressures. The pressure gap can be overcome by either utilizing surface science techniques that can operate at higher pressure or by designing a vacuum chamber with a high pressure reaction cell. The second complication is the "materials gap" which comes from the use of single crystals, wires, and metal foils to model a system as opposed to an industrial grade catalyst. The materials gap can be overcome by slowly increasing the complexity of the model system as more knowledge is obtained. Additional challenges arise when looking at multimetallic systems such as alloys, in which the intended bulk composition of the catalyst is not necessarily reflected in the surface composition.

Herein, two model catalytic systems were studied. The first being a monometallic nano-size clusters supported on an oxide. The second study probes the surface concentration versus the bulk for an alloy, then proceeds to utilize the characterized alloy on an oxide support for catalytic studies. Both of these studies rely heavily on the use of X-ray photoemission spectroscopy (XPS) for the chemical characterization of the surface in ultra-high vacuum conditions (UHV) and gas chromatography (GC) to monitor the reaction kinetics.

Experimental Methods

Ultrahigh Vacuum Chamber with High Pressure Reactor

Experimental work was mainly performed in a multi-technique ultra-high vacuum chamber with a base pressure of 2.0×10^{-10} torr. A vacuum chamber is necessary to study surfaces as it ensures that the surface is free from unwanted contamination over the reaction time frame. When the operation pressure is in the 10^{-10} torr range the surface remains contamination free for at least three hours.[1] The mean free path of subatomic particles in this level of vacuum is large allowing for their use as a probe in surface spectroscopic studies.

The chamber used for these experiments is a commercial PHI 5500 system with a bell-jar analysis chamber that has been modified (Figure 7.2.). The chamber has been modified with the addition of a preparation chamber and a high pressure reactor cell. Each of these separate sections can be isolated by gate valves. The sample can be laterally moved through the chambers using the sample support arm. The analysis section houses the X-ray source with Mg and Al anodes, an Auger gun, differentially pumped ion gun, hemispherical analyzer, monochromotor, ion pump, and a titanium sublimation pump. Connected via a gate valve to the analysis chamber is the preparation chamber section. The preparation chamber is smaller in size than the analysis chamber and is pumped by a turbo-mechanical pump. This section of the chamber is equipped with an E-beam filament, up to five metal dosers, and a leak valve. Separated from the preparation chamber is the high pressure (~1000 torr; 0.2L) reactor that allows for catalytic gas phase reactions

to be carried out without removing the sample from the chamber and exposing it to ambient conditions. The reactor is separated from the bellows by a Teflon sleeve and the bellows are mechanically pumped throughout to remove any reaction gasses leaked into the bellows. The reaction chamber is connected to a double manifold which is pumped by a mechanical pump and a turbo-mechanical pump. The double manifold allows for the premixing and delivery of desired gases into the reaction chamber for catalytic studies. Additionally the double manifold and reaction chamber are connected to the sample loop of a gas chromatograph to allow for the analysis of reaction gases.

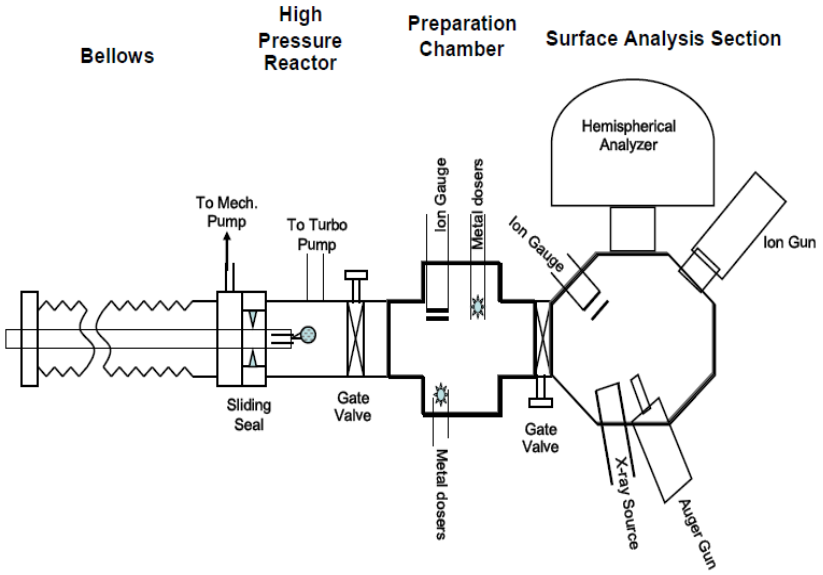

Figure 7.2. Diagram of the UHV chamber.

Sample Preparation

A single-crystal or metal foil was mounted onto the transferable probe using high purity (99.95%) tantalum wires. The sample temperature was measured using a C-type (W-5%: Re/W-26% Re) thermo couple spot-welded to the back of the sample. The sample could be restively heated to 1500K or to 2400K using the E-beam. The sample was cleaned using a combination of Ar^+ sputtering, oxidation (1200K, 5.0 x 10^{-8} torr O_2) and E-beam bombardment on the back side of the sample. Cleaning procedures were repeated until no impurities were detected by XPS analysis.

For metal deposition on the surface metal dosers were employed; where the desired metal is wrapped around a tungsten filament. When adequate current is passed through the filament the desired metal is vaporized and deposited on the sample face. The Co, Pd, and Cu metal dosers were made by wrapping high purity metal wires (>99.5%) around a tungsten wire. The metal dosers were thoroughly degassed for several hours to remove impurities prior to calibration and for 5 minutes for subsequent use in sample preparations. Metal dosers were calibrated using XPS. The intensity of the desired metal peak was ratioed to the substrate peak revealing a break-point at which 1.0 monolayer (ML) was defined. For supported model catalyst studies a SiO_2 layer was deposited using a Si doser which consisted of a 1x1x10 mm^3 Si wafer wrapped with a tungsten wire. The Si was evaporated onto the surface in a background of 1.0 x 10^{-5} torr O_2, followed by annealing at 700K. The thickness of the SiO_2 film was monitored by the attenuation of the substrate signal and the electron escape depth.

X-Ray Photoelectron Spectroscopy

X-ray photoelectron spectroscopy is based on the photoelectric effect and is a highly utilized surface characterization technique. The photoelectric effect is where when a surface is bombarded with electromagnetic waves of sufficient energy electrons can be emitted from the surface. The X-ray photoemission process is illustrated in Figure 7.3. XPS works by irradiating the surface with X-rays which have an energy of hν. The energy of the X-rays is greater than the binding energy of the core electrons. The photon is absorbed by a core-level electron. The core-level electron overcomes the binding energy (E_b) and the work function (Φ) and emerges from the surface with a detectable kinetic energy (E_k). The kinetic energy of the emitted photoelectron is measured by a detector. Using the following equation the binding energy of the surface species can be determined:

$$E_k = h\nu - E_b - \Phi$$

This equation relies on the conservation of energy. The core electrons are characteristic of the individual atom giving each element a unique a distinctive binding energy feature. Each element has an individual fingerprint spectra and binding energy that can be used for identification, oxidative state analysis, and quantification of coverage. Due to the penetration depth of the incident photon and the electron escape depth, XPS give information only from the top most layers of the surface (~3-5 nm).

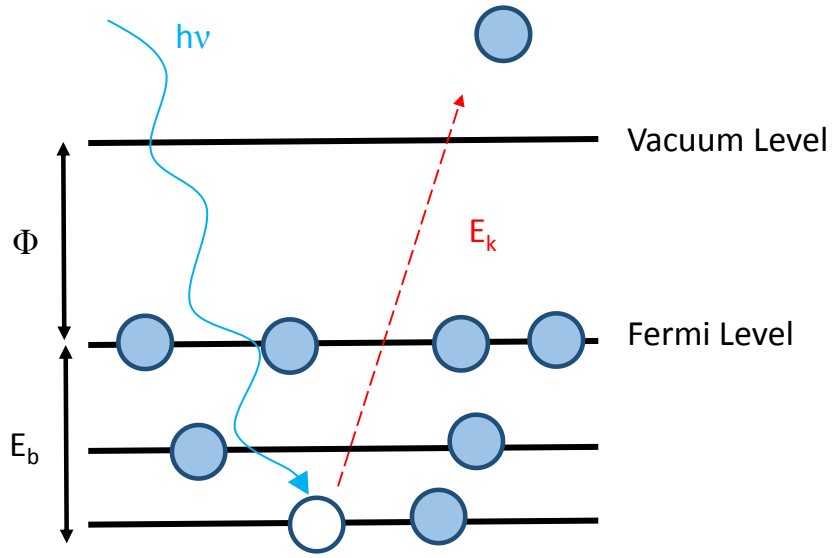

Figure 7.3. Diagram of the photoemission process.

In this work, XPS was used to determine the electronic properties of supported metal catalyst systems. XPS data was collected using a Mg Kα source (Perkin-Elmer). The incident angle was approximately 45° from the surface normal. The photoelectrons were collected and analyzed by a concentric hemispherical analyzer (PHI, SCA 10-360).

Gas Chromatography

To carry out high pressure gas phase reactions, the sample was moved into the reaction cell and the cell was isolated from the preparation chamber by a gate valve. The reaction cell was then filled with the desired gases via the double manifold with the pressure monitored by a baratron gauge and the sample was resistively heated to the

reaction temperature. Before, during, and after the reaction the composition of the gas mixture was monitored using gas chromatography (GC). In GC, the mobile phase is passed through a stationary phase where separation of the analytes occurs. The mobile phase is commonly an inert carrier gas such as hydrogen, helium or nitrogen. The stationary phase is housed inside a column and consist of a microscopic layer of liquid or polymer on an inert solid support. For GC analysis a known volume of gas was introduced via a sample loop and was moved through the column by the carrier gas. The analytes interact with the walls of the column and the support material, based on the strength of this interaction separation occurs. The various components are separated in the column and reach the end of the column at different times; therefore, exhibiting unique retention times. Separations can be controlled by the stationary phase, length and width of the column. A detector is used to monitor the outlet stream from the column and the elution time gives a qualitative identification of the eluted gas. Quantitative measurements are dependent on the peak intensity. The most commonly used detectors are the flame ionization detector (FID) and thermal conductivity detector (TCD); along with coupling GC with mass spectrometry. A TCD detector measures changes in the thermal conductive of a gas passing through a configuration of filaments. When an analyte molecule passes across the filament a decrease in thermal conductivity is detected. Advantages of the TCD are that it is nondestructive and able to identify nearly any chemical changes in the eluting gas. Although, the TCD is capable of detecting a large verity of compound it is lacking in sensitivity at low concentrations. A FID is more sensitive than a TCD, but is used primarily to detect hydrocarbons and is a destructive analysis method. As suggested by

the name, FID work by mixing the eluted gas with hydrogen and dry air then combusting the mixture in a small flame. The flame is located near an electrode and as the sample is pyrolyzed cations and electrons are given off. These species generate a current which is transformed into peaks in a chromatogram. Placing a non-destructive TCD in series before the destructive FID provides complementary detection of the same analytes.

The GC used in this work was the Varian 3400 Cx series which was directly connected to the high pressure reactor cell by a six way valve. Carrier gases were calibrated utilizing a bubble flow meter. The reaction gas sample was introduced into the sample loop, then by switching the positions on the 6-way valve the reaction gas was pushed into the column by the carrier gas. Following separation the eluted gases were first passed through the TCD and secondly analyzed by the FID.

Supported Cobalt Model Catalyst for Particle Size Dependence Determination

Two approaches used for producing substitutes for naturally occurring crude petroleum are to directly convert organics or by converting a mixture of syngas to usable hydrocarbons.[194, 195] The direct liquefaction approach of converting organic materials by heating under high pressure hydrogen had been of the most used until the last half century.[196] In the last half century the indirect liquefaction process of converting syngas, a mixture of CO and H_2, to hydrocarbons over a catalyst has made technological advances.[196] The indirect liquefaction or Fischer-Tropsch (FT) synthesis was first patented in 1926 by two Germans and was notably used to supplement German fuel supplies during World War II.[195]

FT synthesis is commercially catalyzed by a monometallic supported metal composed of either cobalt or iron. The Co catalyst is preferable due to its higher activity, higher chain growth, and lower water-gas shift activity.[197] The downside of using Co as a catalyst is it is approximately 1,000 times more expensive than Fe; therefore, optimal design of the Co catalyst is needed. Decreasing metal particle size is a way to increase the exposed surface area while limiting the mass of Co needed. Unfortunately, some research groups report that particles smaller than 10 nm have a significant decrease in activity[198-201] while others have reported no size dependence.[202-204] Of interest here is elucidating if there is indeed an intrinsic particle size effect.

Commercially available catalyst are commonly produced using wet impregnation methods; therefore, the size of the deposited metal is heterogeneous making size dependent kinetic studies all but impossible. To circumvent the difficulties arising from the catalyst preparation a model catalyst system can be used. Herein, a model catalyst system was produced in the confines of a UHV chamber that combines sample preparatory methods, elemental analysis and a high pressure gas reaction cell. A 10 nm layer of SiO_2 was vapor deposited onto a mounted tantalum foil. Next, Co particles were deposited with the size of the Co particles controlled by the deposition time based on the calibrated dosing rate. Particle sizes in the range of 1.4-10.5 nm were prepared where the particle size and distribution were determined using transmission electron microscopy (TEM).

The prepared model catalyst samples were monitored before and after reaction by XPS analysis. Batch reactions were conducted for 4.5 hours in the high pressure cell at

513K in a mixture of reactant gasses (H_2:CO:N_2 in a volume ratio of 6:3:1; 760 torr). The reaction products were then analyzed using GC. Activity and selectivity were determined based on the GC analysis and the number of exposed active catalyst sites estimated from the TEM analysis. The reaction rate expressed as CO molecules converted per second was significantly higher for particles above 3 nm than below. Relating the reaction rate to the number of active sites the turnover frequency (TOF) was calculated as the number of CO molecules converted per active site per second. The TOF as a function of particle size shows an apparent particle size effect as seen in Figure 7.4. The TOF's for the particles above 3.5 nm are in agreement with reported values for commercially available catalyst.[205, 206]

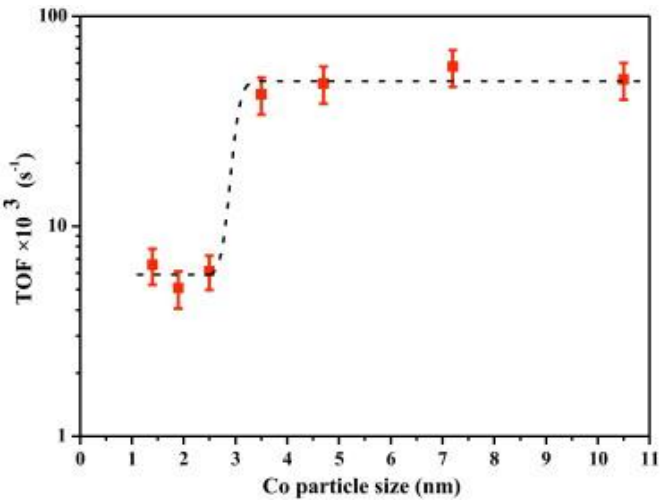

Figure 7.4. TOF as a function of Co particle size. A disjunction is seen around 3 nm. Reprinted with permission from Wang, Z.; Skiles, S.; Yang, F.; Yan, Z.; Goodman, D. W. *Catalysis Today* 2012, 181, 75. Copyright (2012) Elsevier.[207]

Deactivation for FT catalysts has been reported in the literature and is commonly attributed to several factors: sintering of the particles, oxidation, catalyst poisoning due to carbonaceous buildup on the surface.[208] By imaging the particle post reaction by TEM, sintering was eliminated as the deactivation mechanism for the model catalyst system. For all particle sizes examined a distinctive peak showed at 284.6 eV in the C 1s XPS spectra indicative of hydrocarbon products adsorbed onto the surface. XPS analysis of the Co 2p peaks (778.2 and 793.2 eV) pre and post reaction indicate that for particle sizes above 4 nm oxidation does not occur (Figure 7.5). For the 2.5 nm particles oxidation of the Co surface is seen by the two metallic Co peaks decreasing and the growth of four additional features in the spectrum. The Co^{2+} peaks are seen at 782.3 and 797.9 eV and the shake-up satellite peaks for Co^{2+} are at 804.0 and 787.6 eV. It is evident from the XPS data that oxidation occurs for the small particles during the reaction process, in fact it can be seen as quickly as ten minutes into the reaction. A combination of the kinetic data and electronic surface characterization demonstrated that for large Co particles (>4 nm) are not oxidized during reaction where smaller particle are readily and quickly oxidized. The oxidation of the small Co particles leads to a significant decrease in the catalytic activity.

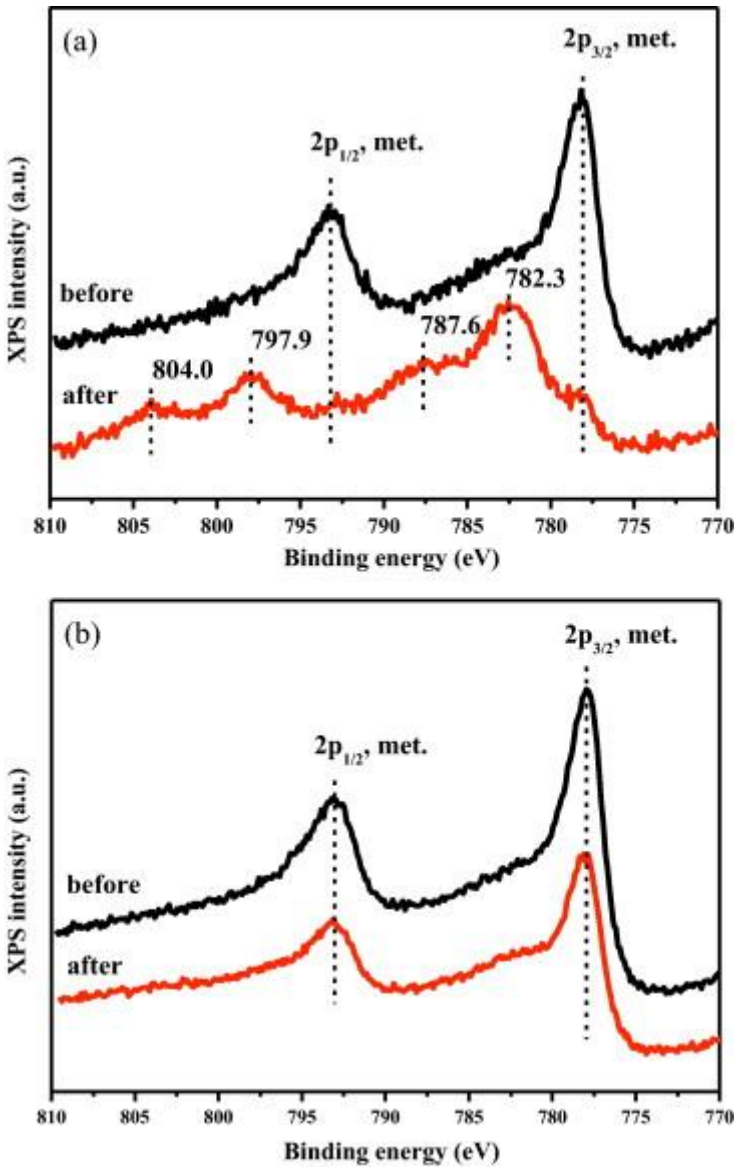

Figure 7.5. XPS spectra of the Co 2p region before and after the FT reaction for the (a) 2.5 nm particles and (b) 4.7 nm particles. Reprinted with permission from Wang, Z.; Skiles, S.; Yang, F.; Yan, Z.; Goodman, D. W. *Catalysis Today* 2012, 181, 75. Copyright (2012) Elsevier.[207]

The review of the literature about the intrinsic Co particle size effect during FT synthesis was inconclusive at best. This is perhaps due to the difficulty in preparing highly reproducible monodispersed Co nanoparticles from cobalt salt precursors. Additional complications in obtaining reliable kinetic data over commercial catalyst arise from support interaction, mass transport, and incomplete reduction of the Co precursor. These issues can be alleviated by studying model catalyst systems careful prepared in UHV conditions.

Palladium-Copper Supported Bimetallic Catalyst

Introduction

Bimetallic catalysts are often deemed superior to their monometallic counterparts due to the synergistic effect from the combination of the two metals. Bimetallic catalyst have been reported to have higher reactivity, selectivity and stability.[1, 191, 209, 210] Plus, bimetallic alloys can be used to catalyze two different reactions occurring in parallel on the individual metallic components of the alloy.[211] The addition of a secondary metal to the system increases the complexity by effecting the geometric surface structure. Catalytic reactions can require certain geometric configurations for activation, therefore, the introduction of a secondary metal can interrupt this geometry and decrease activity.[212, 213] Alloying, surface concentration of metal, and surface restructuring are all of interest when designing an improved bimetallic system opposed to a monometallic system. Two types of bimetallic model catalyst can be utilized: planar bimetallic surfaces and oxide supported bimetallic nano-particles. Due to the high level of complexity of supported bimetallic

catalyst a step-wise approach in designing the model catalyst was used. First the alloying process as a function of heating is investigated, then bimetallic nanoparticles were deposited on a silicon dioxide substrate to catalyze the acetylene hydrogenation reaction. This step-wise approach allows for the systematic increase in complexity of the system with the end goal of developing an optimized "real world" catalyst system.

Bimetallic alloys have had an increase in attention both in academia and industry, due to their usefulness in catalysis, electrochemistry and bio medical applications.[214-217] Palladium-copper catalyst are used for the oxidation of alkenes, hydrogenation of benzene, NO reduction, CO oxidation and acetylene hydrogentation.[214, 215, 218] Pd-Cu alloys have been proposed as a replacement for the 3-way catalyst used in the reduction of car exhaust.[211] The interest in using this alloy as a catalysis has led to many structural, electronic and gas adsorption studies, commonly on well-defined single crystal surfaces.[219] One such study conducted on a Cu/Pd [85:15] surface used multiple surface-sensitive spectroscopic technique to determine the structure and composition of the top-most layers of the alloy.[219] The results of this study indicated an all Cu terminated alloy with significant enrichment of Pd in the second layer was formed. This study did not yield information on any other bulk composition. The use of surface-sensitive techniques to acquire information regarding the surface composition, morphology, and electronic structure of the bimetallic system is essential for the understanding of the role of a second metal (Au, Cu, or Sn) in enhancing the catalytic properties of Pd over a large range of bulk concentrations.

The first part of the work presented here aims to study the alloying of Pd-Cu at the surface for well-defined bulk concentrations. To generate well-defined bulk concentrations a trimetallic system composed of Pd/Cu/Mo was used. These type of systems have been previously used in our laboratory to study alloying when using proper precautions to insure no alloying with the refectory single crystal and with relatively thick (several nm) layers to limit the electronic effects of the support metal.[220] In a trimetallic system the two desired metals are sequentially vapor deposited on a third metallic single crystal substrate of a refractory metal. Care is taken to choose a refectory metal which will not alloy with or have significant electronic interference with the metals of interest. The trimetallic system allows for the precise control of the alloy composition, where as a bimetallic system, depositing one metal on a single crystal of the secondary metal, essentially results in an uncontrollable bulk composition with the single crystal existing in near infinite quantity compared to the deposited metal. The trimetallic system was used to study the effects of annealing temperature on the surface composition of the alloy.

Experimental

The experiments were carried in a multi-technique ultra-high vacuum chamber. The chamber was equipped with X-Ray Photoemission Spectroscopy (XPS) with a mulit-channel detector with a base pressure of 2.0×10^{-10} torr. All XPS experiments were conducted with a Mg Kα source with an approximate angle of incidence of 45˚. A Mo (100) single-crystal sample was supported by high purity tantalum wires on a transferable probe. The sample could be resistively heated to 1500K or e-beam heated to 2400K. All

temperatures were measured using a C-type thermo couple (W-5% Re/W-26%Re) spot-welded to the back of the single crystal. Repeated cycles of Ar^+ sputtering and e-beam heating to 2000K were used to clean the crystal surface. Cleanliness was determined by XPS. Copper and palladium were vapor deposited onto the surface using resistively heated Ta filaments wrapped in the corresponding high-purity wire (99.99%). Dosers were thoroughly degassed to remove impurities before use. Coverage was monitored using XPS and calibrated using the break-point technique.

For surface alloying studies sequential deposition of 5.0 ML Cu followed by 5.0 ML Pd onto the Mo surface were used, denoted as 5.0 ML Pd/5.0 ML Cu/ Mo. The order of deposition was varied to insure alloy formation was not influenced by the deposition order. All XPS spectra were collected at room temperature after annealing for 20 minutes at the desired temperature. For catalytic studies, a silicon dioxide layer was formed on the Mo single crystal using vapor deposition. The Pd and Cu were added to the surface sequentially. After metal deposition the sample was annealed at 500K in vacuum for 20 minutes. Acetylene hydrogenation reactions were carried preformed in the high pressure cell at 300K with an initial pressure of 760 torr. Hydrocarbon analysis was performed with the GC utilizing a Porapak Q column. The surfaces were analyzed pre- and post-reaction with XPS.

Alloying Properties

XPS was used to explore the electronic properties of annealing the Cu-Pd surface. The Pd 3d core level spectra and the Cu 2p were collected following annealing of the

sample. All XPS spectra were corrected for the centroid of the Mo $3d_{5/2}$ peak being at 227.7 eV. For both the 5.0 ML Cu/ 5.0 ML Pd/Mo surface and the 5.0 ML Pd/ 5.0 ML Cu/ Mo surface, a stable value but with a +0.2 eV shift from the bulk value was seen for the centroid of the Pd $3d_{3/2}$ peak in the range of 400K-700K, as show in Figure 7.6. A positive core- level binding energy (CLBE) shift was observed with temperatures higher than 700 K. The stable value that was +0.2 from the bulk is an indication of perturbation of the Pd core level properties due to Pd-Cu alloying in this temperature range. Further increase in the CLBE above 700K can be attributed to variations in the surface morphology. This was confirmed by the increased intensity of the Mo peak, indicating changes in the surface morphology. To monitor the Cu-Pd alloying process, the Pd $3d_{3/2}$ peak area was plotted in Figure 7.7 as a function of annealing temperature. There are small changes in the intensity seen in the temperature range of 300 to 800 K due to the alloying process. There is a continual decrease in the peak area beginning after annealing to 800K, indicating attenuation of this peak by alloying and surface segregation of the Cu. The decrease above this temperate is suspected to be due to changes in surface morphology.

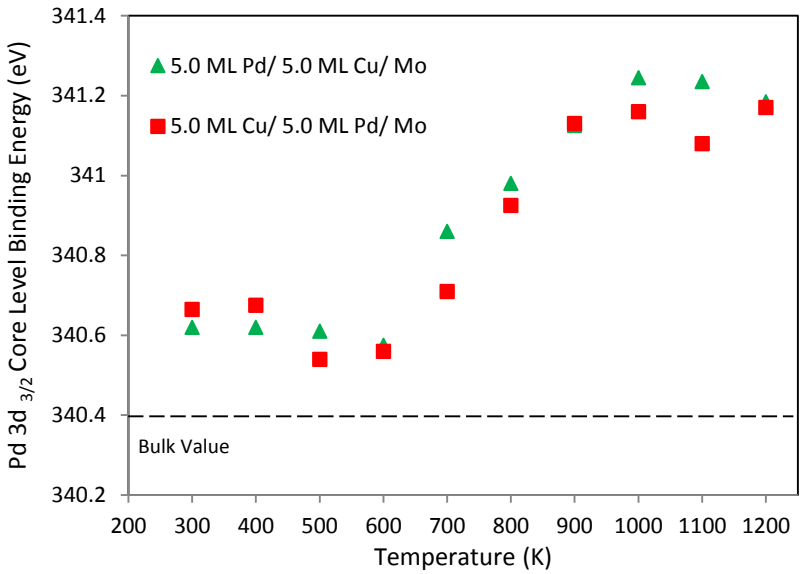

Figure 7.6. The centroids of Pd $3d_{3/2}$ position plotted as a function of annealing temperature.

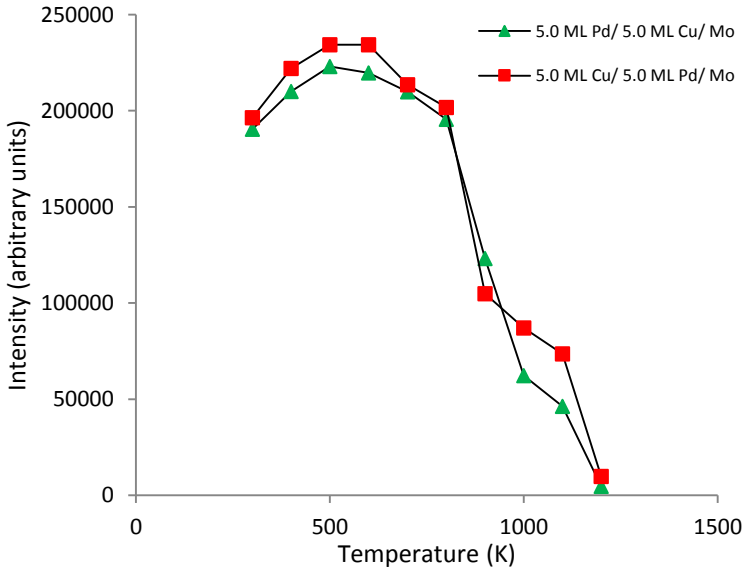

Figure 7.7. The Pd $3d_{3/2}$ peak area as a function of annealing temperature.

The Cu 2p peak spectra are shown in Figure 7.8. The CLBE for the Cu $2p_{1/2}$ peak in the 5.0 ML Cu/ 5.0 ML Pd/ Mo is stable at the various annealing temperatures and shifted 0.6 eV from the bulk. This sample shows a slow decrease in Cu peak area from 300K to 600K during alloy formation, then a more rapid decrease above 600K as morphologic changes in the surface occur and Cu begins to desorb. For 5.0 ML Pd/ 5.0 ML Cu/ Mo there was an initial decrease in the CLBE from 300K to 600K, strongly indicating alloy formation in this range. Further supporting alloy formation in the range of 400K to 600K is the large increase in area of the Cu followed by a decrease as Cu desorbs. It should be noted that the Mo 3d peaks were monitored for all samples. There was no shift in the centroid, indicating there was not perturbation of the core level electronic properties due to alloying of the Pd or Cu with the Mo single crystal. This experimentation was repeated on a Mo (100) surface to determine if the different overlayer growth structure influenced alloy formation. The results were in agreement with those reported above. The XPS results confirm alloying of the metals in the bulk material.

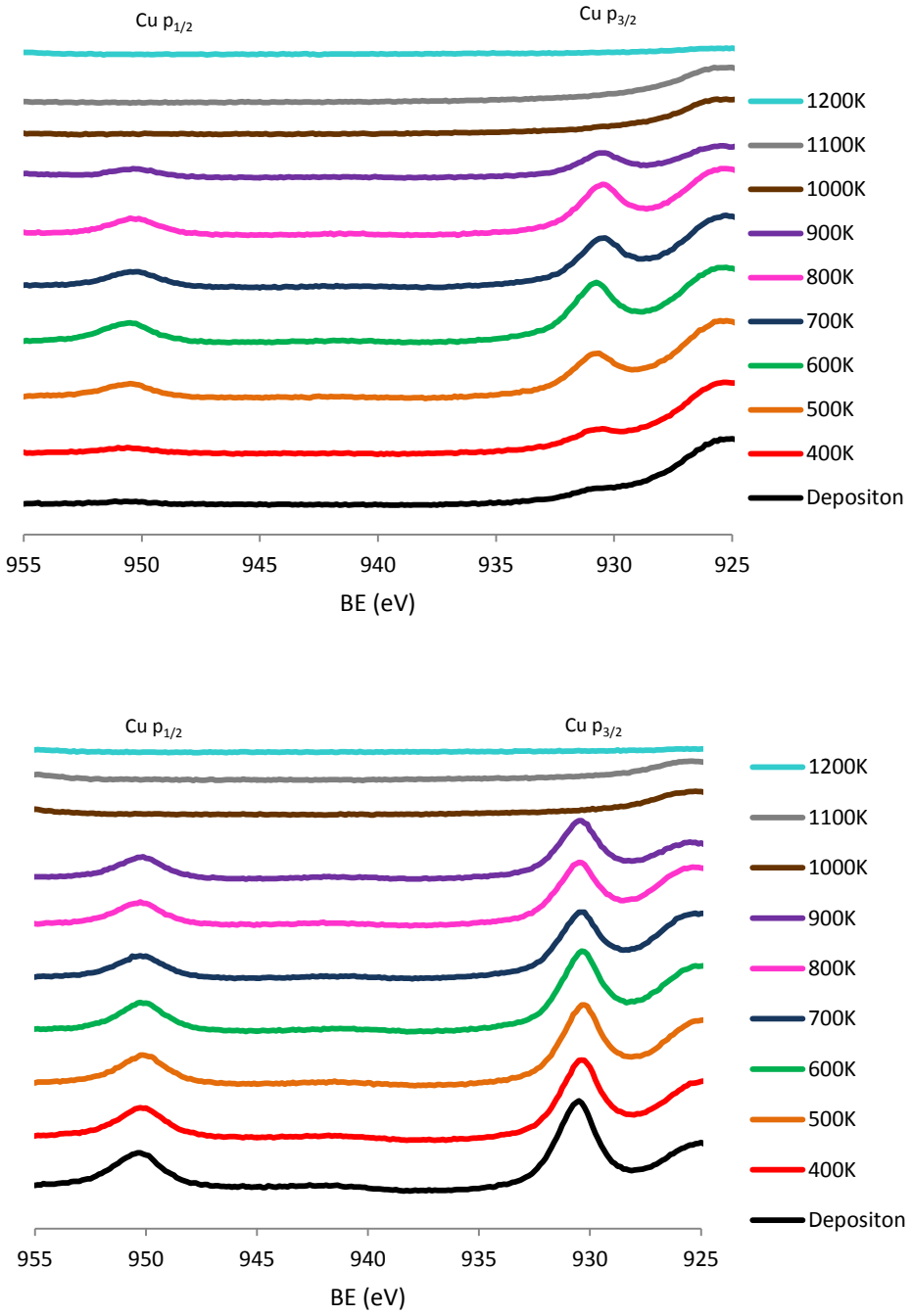

Figure 7.8. Cu 2p spectra of 5.0 ML Cu/ 5.0 ML Pd/ Mo (top) and 5.0 ML Pd/ 5.0 ML Cu/ Mo (bottom) after annealing to different temperatures.

X-rays penetrate into the near surface region of the alloy sample; therefore, while capable of monitoring alloying during annealing, it is unable to give definitive information on only the outer most layer. The surface concentration and alloying of Pd/Cu/Mo trimetallic systems is supported by low energy ion scattering spectroscopy (LEIS) conducted in the Goodman lab by Dr. Kai Luo.[221] LEIS is an analytical method for the chemical characterization of a solid surface, yielding information about the atomic composition of the outermost layer. In LEIS the surface is bombarded with a beam of gas ions. When the ion collides with a surface atom, moment and energy are conserved and the ion is back scattered. The energy of the backscattered particles can be used to identify the mass of the surface atom it interacted with. From this information the surface concentration was calculated. The surface composition was found to vary between 300K and 500K for the two deposition orders, indicating this is the temperature range in which alloying takes place. A stable surface concentration between 500K and 700K that is independent of deposition sequence shows the alloy is stable in this range, with the surface composition being 70% Cu. The Pd surface composition reached near 100% after the desorption of Cu at 1100K. By varying the bulk concentrations a surface versus bulk composition phase diagram was created as shown in Figure 7.9.

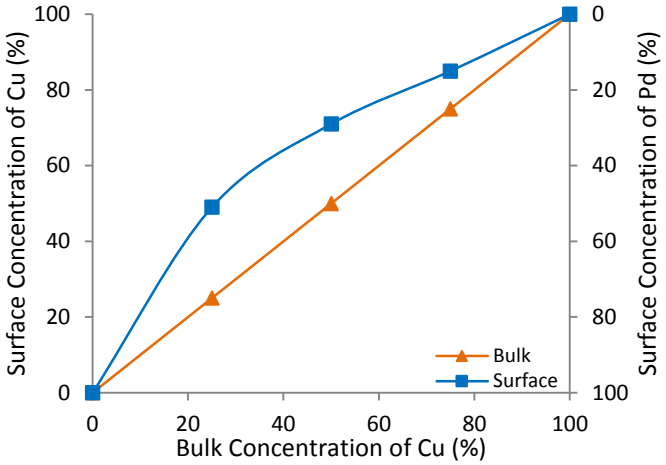

Figure 7.9. Surface verse bulk concentration phase diagram obtained from the LEIS analysis. Copper is seen to segregate to the surface.

Pd-Cu bimetallic alloys were prepared and studied using surface sensitive techniques. It was determined from LEIS and XPS results that a stable surface alloy was formed in the range of 500K and 700K. In a 1:1 Pd-Cu alloy the surface composition after annealing to 600K was 71% Cu, and found to be independent of metal deposition order. This lies in agreement with previous modeling studies based on surface free energy arguments.[222, 223] After an understanding of the surface alloying of the trimetallic system was achieved, the complexity of the model catalyst system can be increased to include an oxide layer. The oxide layer allows for modeling of the bimetallic system as supported nanoparticles.

Catalytic Testing

For the development and testing of the model system a catalytic reaction is employed. The acetylene hydrogenation reaction is essential in the processing of ethylene streams before ethylene polymerization.[216] Ethylene obtained from thermal cracking contains small amounts of acetylene. The acetylene is known to poison the ethylene polymerization catalyst when present in even small amounts; therefore, it is desirable to remove the acetylene prior to introduction of the ethylene polymerization catalyst. The acetylene hydrogenation reaction occurs in a series from acetylene to ethylene to ethane.[216] The desired product is an intermediate in the series; therefore, it can be easily overshot if the catalyst does not have high selectivity to the desired product. Monometallic Pd catalysts have high activity for removing acetylene, but have poor selectivity. The addition of a promoter metals is known to improve the catalyst performance of Pd.[224-228]

Initial studies of acetylene hydrogenation were conducted on supported bimetallic model catalyst systems. A monometallic model system was generated by depositing 0.5 ML Pd on a SiO_2/ Mo substrate. The bimetallic system was generated by vapor depositing 0.5 ML Pd followed by 0.5 ML Cu on the substrate and annealing for 20 minutes at 500K. The acetylene hydrogenation reaction was carried out in a batch reaction and monitored every 15 minutes by GC. To simulate ethylene streams produced by thermal cracking, the starting gas mixture was ~2.2% acetylene with the balance being ethylene. The time studies of the mono- and bi- metallic systems can be seen in Figure 7.10. The acetylene conversion for the monometallic system was 5.9%, while the conversion for the bimetallic

was only 1.6%. In each case the over conversion to ethane is limited to percent concentration less than 0.06%. It should be noted that these were singular, non-repeated, reaction studies due to unforeseen time constraints. Several explanations for these results can be postulated. Such as, while copper is a known premotor of this reaction, the concentration of copper is high. Since copper has been shown to segregate to surface, the number of Pd reaction sites could be limited. Optimization of the metal ratios is needed. Premotor metals are typically used in smaller concentrations than this initial study. A second explanation for the observed results is that these are anomalous results. Both of these explanations are highly speculative and without further investigation neither can be validated.

Conclusion

Monometallic and bimetallic model catalyst systems have been utilized in characterizing the fundamental processes that occur during catalytic reactions. A monometallic oxide supported Co system was used to investigate the intrinsic particle size effect for FT synthesis. It was determined utilizing XPS that particles smaller than 3 nm were easily oxidized during reaction and deactivated. XPS was also utilized in studying the electronic effect of alloying Pd/Cu surfaces. Combining the XPS results along with previous LEIS studies concludes that Cu preferentially segregates to the surface. The limited supported bimetallic Pd/Cu/SiO_2 catalyzed reactions were inconclusive on the promoting effect of the Cu on reaction activity.

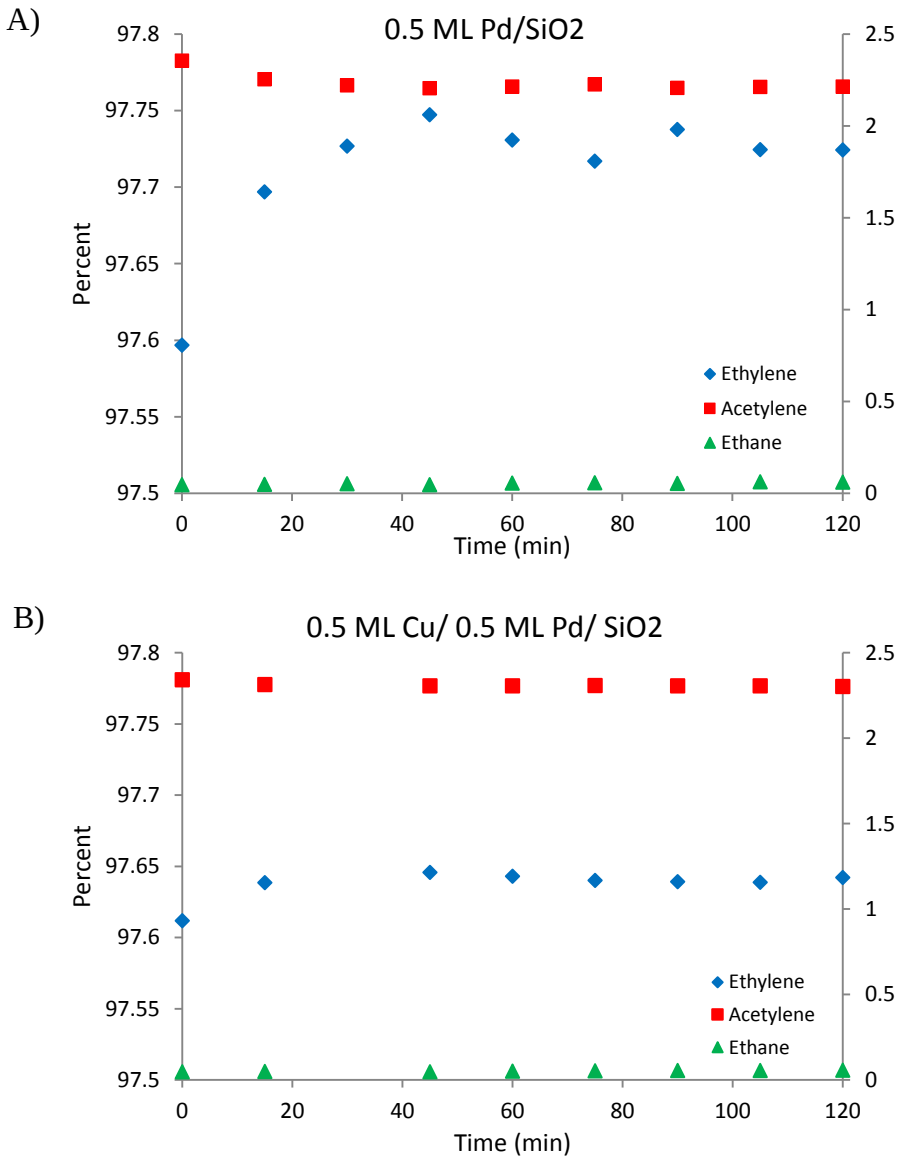

Figure 7.10. Time traces of the acetylene hydrogenation reaction over A) 0.5 ML Pd / SiO_2 and B) 0.5 ML Cu/ 0.5 ML Pd/ SiO_2.

CHAPTER VIII

CONCLUSION

The work in this dissertation takes advantage of surface science techniques to explore complex surfaces and their properties. Surfaces span the range from precisely controlled systems with every atom in its place to complex random samples. This dissertation examined systems near each one of these extremes. The poly(*N*-isopropylacrylamide) and silica nanoparticle surface was formed in a systematic manor, yet lack the precise control afforded by the preparation of the model catalyst systems in ultra-high vacuum.

A stimulus responsive or smart polymer respond to stimuli such as solvents, temperature, counter ions, electrical current, pH, or mechanical pressure.[4-6] One of the most studied stimulus responsive polymers is poly(*N*-isopropylacrylamide) (PNIPAM) due to its potential uses in surface coatings, microfluidics, and drug delivery.[7-9] PNIPAM, a thermoresponsive polymer, exhibits a lower critical solution temperature (LCST) in aqueous solutions. Covalently-bound composite polymer grafts of poly(*N*-isopropylacrylamide)-*c*-poly(*N*-acryloxysuccinimide) (PNIPAM-*c*-PNASI) and aminated silica nanoparticles were deposited onto a silicon wafer using covalent layer-by-layer assembly. It is known that when grafted to a surface, these polymers' response to external stimuli causes measureable changes in the surface topography and wettability.[30, 97, 179] In similar polymeric systems, the restructuring of the surface in response to external stimuli is known to affect the Young's elastic modulus.[69] It has been shown that the elastic

modulus of the polymer graft can be switched by varying the temperature or by the addition of counter ions to solution. Using colloidal probe microscopy the mechanical properties of the films were investigated. The Hertz contact mechanics model was used to extract the Young's elastic modulus from a series of force distance curves. The elastic modulus was shown to nearly double when the temperature of the polymer composite graft was raised above the LCST in water. The elastic modulus was found to be responsive to variations in exposure for a range of temperatures and counter ions. The elastic modulus could be controlled by introducing salts to the polymers environment form the Hofmeister series of salts. These salts effect the polymer's LCST, therefore effecting the polymers configuration at room temperature. The elastic modulus was found to span over an order of magnitude depending on the current environment and cleaning procedures.

Based on the same polymeric system, an oil and water separation filter was developed. A porous silica filter was functionalized utilized the covalent layer-by-layer assembly method.[65] These functionalized frit have controllable flow rate depending on the salts in solution.[65] Additionally due to PNIPAMs oleophobicity, separation of oil and water emulsions was shown within this dissertation. The demulsification process leds to a filtrate that was nearly free of contaminating oil without the addition of harmful chemical demulsifiers currently used in oil spill remediation. When extended from pure water to simulated ocean water, the demulsification process is slowed by the presence of salts in solution, but still succeeds in generating a free from oil water filtrate.

While catalytic studies have been around for centuries, the development of ultra-high vacuum environment and surface sensitive techniques have largely impacted catalytic studies. Two model catalyst systems were developed to gather insight into the catalytic processes on the metal surface. A monometallic cobalt system was developed for Fisher-Tropsch (FT) reaction. The effect of cobalt particle size was studied on Co/SiO_2 model catalysts that were prepared and characterized in an ultrahigh vacuum chamber. The catalyst were prepared with various metal particle sizes from 1.4 – 10.5 nm, as determined by TEM analysis. Small cobalt particles (1.4 – 2.5 nm) showed a lower catalytic activity. This was attributed to the cobalt surface being readily oxidized by the water vapor produced during the reaction. This oxidation was confirmed by post-reaction X-ray photoelectron spectroscopy (XPS) analysis. Larger cobalt particles did not show oxidation, resulting in relatively constant catalytic reactivity and selectivity. The lack of particle size effects for the larger particles is consistent with the reported structure insensitivity for FT synthesis.[198-204] A second model system was also investigated. In this study low energy ion scattering spectroscopy and XPS were used to study the effects of annealing temperature on the surface compositions of Pd-Cu alloys. A stable surface alloy was formed between 500K and 700K, with surface enrichment of copper. Initial acetylene hydrogenation studies over an oxide supported bimetallic Pd-Cu model catalyst gave inconclusive result for the use of Cu as a promoter metal for the reaction.

Advances in surface science over the last half century have opened up whole new areas of study. These techniques allow for the study of the surface at a level not possible

centuries ago. These advances have led to innovations on many technological fronts and will continue to do so.

REFERENCES

1. Somorjai, G. A.; Li, Y., *Introduction to Surface Chemistry and Catalysis*. 2 ed.; John Wiley & Sons: Hoboken, NJ, **2010**.

2. Kurt, K., *Surface Science: Foundations of Catalysis and Nanoscience* 2nd ed.; John Wiley & Sons: West Sussex, UK, **2009**.

3. Nagel, M., *J. Chem. Educ.* **1980,** *57* (11), 811.

4. Chen, T.; Ferris, R.; Zhang, J.; Ducker, R.; Zauscher, S., *Prog. Polym. Sci.* **2010,** *35* (1–2), 94-112.

5. Myrat, C. D.; Rowlinson, J. S., *Polymer* **1965,** *6* (12), 645-651.

6. Sun, S.; Wu, P., *Macromolecules* **2010,** *43* (22), 9501-9510.

7. Schmidt, S.; Zeiser, M.; Hellweg, T.; Duschl, C.; Fery, A.; Möhwald, H., *Adv. Funct. Mater.* **2010,** *20* (19), 3235-3243.

8. Hernández, R.; Sacristán, J.; Asín, L.; Torres, T. E.; Ibarra, M. R.; Goya, G. F.; Mijangos, C., *J. Phys. Chem. B* **2010,** *114* (37), 12002-12007.

9. Akimoto, J.; Nakayama, M.; Sakai, K.; Okano, T., *Biomacromolecules* **2009,** *10* (6), 1331-1336.

10. de Villiers, M. M.; Otto, D. P.; Strydom, S. J.; Lvov, Y. M., *Adv. Drug Del. Rev.* **2011,** *63* (9), 701-715.

11. Hoare, T. R.; Kohane, D. S., *Polymer* **2008,** *49* (8), 1993-2007.

12. Oh, J. K.; Drumright, R.; Siegwart, D. J.; Matyjaszewski, K., *Prog. Polym. Sci.* **2008,** *33* (4), 448-477.

13. Rapoport, N., *Prog. Polym. Sci.* **2007,** *32* (8–9), 962-990.

14. Schmaljohann, D., *Adv. Drug Del. Rev.* **2006,** *58* (15), 1655-1670.

15. Bae, Y.; Fukushima, S.; Harada, A.; Kataoka, K., *Angew. Chem. Int. Ed.* **2003,** *42* (38), 4640-4643.

16. Bajpai, A. K.; Shukla, S. K.; Bhanu, S.; Kankane, S., *Prog. Polym. Sci.* **2008,** *33* (11), 1088-1118.

17. Chilkoti, A.; Dreher, M. R.; Meyer, D. E.; Raucher, D., *Adv. Drug Del. Rev.* **2002,** *54* (5), 613-630.

18. Chung, J. E.; Yokoyama, M.; Yamato, M.; Aoyagi, T.; Sakurai, Y.; Okano, T., *J. Controlled Release* **1999,** *62* (1–2), 115-127.

19. Soppimath, K. S.; Tan, D. C. W.; Yang, Y. Y., *Adv. Mater.* **2005,** *17* (3), 318-323.

20. Dimitrov, I.; Trzebicka, B.; Müller, A. H. E.; Dworak, A.; Tsvetanov, C. B., *Prog. Polym. Sci.* **2007,** *32* (11), 1275-1343.

21. Li, S.; Su, Y.; Dan, M.; Zhang, W., *Polym. Chem.* **2014,** *5* (4), 1219-1228.

22. Minko, S., *J. Macromol. Sci., Part C* **2006,** *46* (4), 397-420.

23. Hofmeister, F., *Naunyn-Schmiedeberg's Arch. Pharmacol.* **1888,** *24* (4), 247-260.

24. Maeda, Y.; Nakamura, T.; Ikeda, I., *Macromolecules* **2001,** *35* (1), 217-222.

25. Schild, H. G.; Tirrell, D. A., *J. Phys. Chem.* **1990,** *94* (10), 4352-4356.

26. Cowie, J. M. G.; McEwen, I. J., *J. Polym. Sci., Polym. Phys. Ed.* **1974,** *12* (2), 441-443.

27. Pfohl, O.; Hino, T.; Prausnitz, J. M., *Polymer* **1995,** *36* (10), 2065-2073.

28. Everett, D. H.; Stageman, J. F., *Colloid. Polym. Sci.* **1977,** *255* (3), 293-294.

29. Annaka, M.; Yahiro, C.; Nagase, K.; Kikuchi, A.; Okano, T., *Polymer* **2007,** *48* (19), 5713-5720.

30. Fu, H.; Hong, X.; Wan, A.; Batteas, J. D.; Bergbreiter, D. E., *ACS Appl. Mater. Interfaces* **2010,** *2* (2), 452-458.

31. Cheng, X.; Canavan, H. E.; Stein, M. J.; Hull, J. R.; Kweskin, S. J.; Wagner, M. S.; Somorjai, G. A.; Castner, D. G.; Ratner, B. D., *Langmuir* **2005,** *21* (17), 7833-7841.

32. Zhang, Y.; Furyk, S.; Sagle, L. B.; Cho, Y.; Bergbreiter, D. E.; Cremer, P. S., *J. Phys. Chem. C* **2007,** *111* (25), 8916-8924.

33. Kubota, K.; Fujishige, S.; Ando, I., *J. Phys. Chem.* **1990,** *94* (12), 5154-5158.

34. Wu, C.; Wang, X., *Phys. Rev. Lett.* **1998,** *80* (18), 4092-4094.

35. Elliott, L. C. C.; Barhoum, M.; Harris, J. M.; Bohn, P. W., *Langmuir* **2011,** *27* (17), 11037-11043.

36. Yang, Q.; Zhao, J., *Langmuir* **2011,** *27* (19), 11757-11760.

37. Popa, A. M.; Angeloni, S.; Bürgi, T.; Hubbell, J. A.; Heinzelmann, H.; Pugin, R. l., *Langmuir* **2010,** *26* (19), 15356-15365.

38. Meewes, M.; Ricka, J.; De Silva, M.; Nyffenegger, R.; Binkert, T., *Macromolecules* **1991,** *24* (21), 5811-5816.

39. Mao, H.; Li, C.; Zhang, Y.; Bergbreiter, D. E.; Cremer, P. S., *J. Am. Chem. Soc.* **2003,** *125* (10), 2850-2851.

40. Bergbreiter, D. E.; Fu, H., *J. Polym. Sci., Part A: Polym. Chem.* **2008,** *46* (1), 186-193.

41. Gao, J.; Wu, C., *Macromolecules* **1997,** *30* (22), 6873-6876.

42. Wohlfarth, C., pVT data of poly(N-ethyl-N-methylacrylamide) in water and 2-propanol. In *Polym. Sol.*, Lechner, M. D.; Arndt, K. F., Eds. Springer Berlin Heidelberg: New York, NY, **2013;** pp 204-204.

43. Mikheeva, L. M.; Grinberg, N. V.; Mashkevich, A. Y.; Grinberg, V. Y.; Thanh, L. T. M.; Makhaeva, E. E.; Khokhlov, A. R., *Macromolecules* **1997,** *30* (9), 2693-2699.

44. Etika, K. C.; Jochum, F. D.; Theato, P.; Grunlan, J. C., *J. Am. Chem. Soc.* **2009,** *131* (38), 13598-13599.

45. Zhou, Y.; Yan, D.; Dong, W.; Tian, Y., *J. Phys. Chem. B* **2007,** *111* (6), 1262-1270.

46. Schmidt, P.; Dybal, J.; Rodriguez-Cabello, J. C.; Reboto, V., *Biomacromolecules* **2005,** *6* (2), 697-706.

47. Fullbrandt, M.; von Klitzing, R.; Schonhals, A., *Soft Matter* **2012,** *8*, 12116-12123.

48. Kuznetsov, Y. A.; Timoshenko, E. G.; Dawson, K. A., *J. Chem. Phys.* **1996,** *104* (9), 3338-3347.

49. Wu, C., *Polymer* **1998,** *39* (19), 4609-4619.

50. Zhu, P. W.; Napper, D. H., *J. Phys. Chem. B* **1997,** *101* (16), 3155-3160.

51. Zhou, K.; Lu, Y.; Li, J.; Shen, L.; Zhang, G.; Xie, Z.; Wu, C., *Macromolecules* **2008,** *41* (22), 8927-8931.

52. Jia, Z.; Chen, H.; Zhu, X.; Yan, D., *J. Am. Chem. Soc.* **2006,** *128* (25), 8144-8145.

53. Lee, S. B.; Song, S.-C.; Jin, J.-I.; Sohn, Y. S., *J. Am. Chem. Soc.* **2000,** *122* (34), 8315-8316.

54. Dalkas, G.; Pagonis, K.; Bokias, G., *Polymer* **2006,** *47* (1), 243-248.

55. Furyk, S.; Zhang, Y.; Ortiz-Acosta, D.; Cremer, P. S.; Bergbreiter, D. E., *J. Polym. Sci., Part A: Polym. Chem.* **2006,** *44* (4), 1492-1501.

56. Zhang, Y.; Yarin, A. L., *J. Mater. Chem.* **2009,** *19* (27), 4732-4739.

57. Omta, A. W.; Kropman, M. F.; Woutersen, S.; Bakker, H. J., *Science* **2003,** *301* (5631), 347-349.

58. Zhang, Y.; Cremer, P. S., *Curr. Opin. Chem. Biol.* **2006,** *10* (6), 658-663.

59. Cho, Y.; Zhang, Y.; Christensen, T.; Sagle, L. B.; Chilkoti, A.; Cremer, P. S., *J. Phys. Chem. B* **2008,** *112* (44), 13765-13771.

60. Gurau, M. C.; Lim, S.-M.; Castellana, E. T.; Albertorio, F.; Kataoka, S.; Cremer, P. S., *J. Am. Chem. Soc.* **2004,** *126* (34), 10522-10523.

61. Bloksma, M. M.; Bakker, D. J.; Weber, C.; Hoogenboom, R.; Schubert, U. S., *Macromol. Rapid Commun.* **2010,** *31* (8), 724-728.

62. Zhang, Y.; Furyk, S.; Bergbreiter, D. E.; Cremer, P. S., *J. Am. Chem. Soc.* **2005,** *127* (41), 14505-14510.

63. Stuart, M. A. C.; Huck, W. T. S.; Genzer, J.; Muller, M.; Ober, C.; Stamm, M.; Sukhorukov, G. B.; Szleifer, I.; Tsukruk, V. V.; Urban, M.; Winnik, F.; Zauscher, S.; Luzinov, I.; Minko, S., *Nat. Mater.* **2010,** *9* (2), 101-113.

64. Xiang, M.; Wilhelm, A.; Luo, C., *Langmuir* **2013,** *29* (25), 7715-7725.

65. Allen, A. L.; Tan, K. J.; Fu, H.; Batteas, J. D.; Bergbreiter, D. E., *Langmuir* **2012,** *28* (11), 5237-5242.

66. van den Brom, C. R.; Anac, I.; Roskamp, R. F.; Retsch, M.; Jonas, U.; Menges, B.; Preece, J. A., *J. Mater. Chem.* **2010,** *20* (23), 4827-4839.

67. MacKay, J. A.; Callahan, D. J.; FitzGerald, K. N.; Chilkoti, A., *Biomacromolecules* **2010,** *11* (11), 2873-2879.

68. Jiang, Y.; Wang, Z.; Yu, X.; Shi, F.; Xu, H.; Zhang, X.; Smet, M.; Dehaen, W., *Langmuir* **2005,** *21* (5), 1986-1990.

69. Sui, X.; Chen, Q.; Hempenius, M. A.; Vancso, G. J., *Small* **2011,** *7* (10), 1440-1447.

70. Laurent, P.; Souharce, G.; Duchet-Rumeau, J.; Portinha, D.; Charlot, A., *Soft Matter* **2012,** *8* (3), 715-725.

71. Edmondson, S.; Nguyen, N. T.; Lewis, A. L.; Armes, S. P., *Langmuir* **2010,** *26* (10), 7216-7226.

72. Edmondson, S.; Osborne, V. L.; Huck, W. T. S., *Chem. Soc. Rev.* **2004,** *33* (1), 14-22.

73. Jordan, R.; Ulman, A.; Kang, J. F.; Rafailovich, M. H.; Sokolov, J., *J. Am. Chem. Soc.* **1999,** *121* (5), 1016-1022.

74. Zhao, B.; Zhu, L., *Macromolecules* **2009,** *42* (24), 9369-9383.

75. Li, Y.; Liu, F.; Sun, J., *Chem. Commun.* **2009,** *19* (19), 2730-2732.

76. Li, Y.; Wang, X.; Sun, J., *Chem. Soc. Rev.* **2012,** *41* (18), 5998-6009.

77. Hirata, I.; Okazaki, M.; Iwata, H., *Polymer* **2004,** *45* (16), 5569-5578.

78. Gil, E. S.; Park, S.-H.; Tien, L. W.; Trimmer, B.; Hudson, S. M.; Kaplan, D. L., *Langmuir* **2010,** *26* (19), 15614-15624.

79. Snyder, D. M., *J. Chem. Educ.* **1989,** *66* (12), 977.

80. Kim, D. W.; Blumstein, A.; Kumar, J.; Samuelson, L. A.; Kang, B.; Sung, C., *Chem. Mater.* **2002,** *14* (9), 3925-3929.

81. Chang, Y. L.; West, M. A.; Fowler, F. W.; Lauher, J. W., *J. Am. Chem. Soc.* **1993,** *115* (14), 5991-6000.

82. Ali, M.; Yameen, B.; Cervera, J.; Ramírez, P.; Neumann, R.; Ensinger, W.; Knoll, W.; Azzaroni, O., *J. Am. Chem. Soc.* **2010,** *132* (24), 8338-8348.

83. Bergbreiter, D. E.; Liao, K.-S., *Soft Matter* **2009,** *5* (1), 23-28.

84. Tasuku, O.; Bin, D.; Yuji, S.; Seimei, S., *Nanotechnology* **2007,** *18* (16), 165607-165615.

85. Laufer, G.; Kirkland, C.; Cain, A. A.; Grunlan, J. C., *ACS Appl. Mater. Interfaces* **2012,** *4* (3), 1643-1649.

86. Liu, Y.; Liu, Y.; Feng, H.; Wu, Y.; Joshi, L.; Zeng, X.; Li, J., *Biosens. Bioelectron.* **2012,** *35* (1), 63-68.

87. Lefort, M.; Jierry, L.; Boulmedais, F.; Benmlih, K.; Lavalle, P.; Senger, B.; Voegel, J.-C.; Hemmerlé, J.; Ponche, A.; Schaaf, P., *Langmuir* **2013,** *29* (47), 14536-14544.

88. Izquierdo, A.; Ono, S. S.; Voegel, J. C.; Schaaf, P.; Decher, G., *Langmuir* **2005,** *21* (16), 7558-7567.

89. Sung, C.; Hearn, K.; Reid, D. K.; Vidyasagar, A.; Lutkenhaus, J. L., *Langmuir* **2013,** *29* (28), 8907-8913.

90. Krogman, K. C.; Zacharia, N. S.; Schroeder, S.; Hammond, P. T., *Langmuir* **2007,** *23* (6), 3137-3141.

91. Bose, S.; Keller, S. S.; Alstrøm, T. S.; Boisen, A.; Almdal, K., *Langmuir* **2013,** *29* (23), 6911-6919.

92. Zhang, X.; Wu, T.; Sun, J.; Shen, J., *Colloids Surf. Physicochem. Eng. Aspects* **2002,** *198* (0), 439-442.

93. Kim, D. W.; Kumar, J.; Blumstein, A., *Appl. Clay Sci.* **2005,** *30* (2), 134-140.

94. Cheung, J. H.; Stockton, W. B.; Rubner, M. F., *Macromolecules* **1997,** *30* (9), 2712-2716.

95. Hollman, A. M.; Bhattacharyya, D., *Langmuir* **2004,** *20* (13), 5418-5424.

96. Zhai, L.; Cebeci, F. Ç.; Cohen, R. E.; Rubner, M. F., *Nano Lett.* **2004,** *4* (7), 1349-1353.

97. Liao, K. S.; Fu, H.; Wan, A.; Batteas, J. D.; Bergbreiter, D. E., *Langmuir* **2008,** *25* (1), 26-28.

98. Garrett, T. R.; Bhakoo, M.; Zhang, Z., *Prog. Nat. Sci.* **2008,** *18* (9), 1049-1056.

99. Renner, L. D.; Weibel, D. B., *MRS Bull.* **2011,** *36* (05), 347-355.

100. Lee, E. L.; von Recum, H. A., *Journal of Biomedical Materials Research* **2010,** *93* (2), 411-418.

101. Schild, H. G., *Prog. Polym. Sci.* **1992,** *17* (2), 163-249.

102. Chiantore, O.; Guaita, M.; Trossarelli, L., *Die Makromolekulare Chemie* **1979,** *180* (4), 969-973.

103. Cole, C.-A.; Schreiner Sigrid, M.; Priest John, H.; Monji, N.; Hoffman Allan, S., N-Isopropylacrylamide and N-Acryloxysuccinimide Copolymer. In *Reversible Polymeric Gels and Related Systems*, American Chemical Society: Seattle, WA, **1987;** Vol. 350, pp 245-254.

104. Inomata, H.; Goto, S.; Saito, S., *Macromolecules* **1990,** *23* (22), 4887-4888.

105. Scarpa, J. S.; Mueller, D. D.; Klotz, I. M., *J. Am. Chem. Soc.* **1967,** *89* (24), 6024-6030.

106. Heskins, M.; Guillet, J. E., *J. Macromol. Sci., Part A: Pure Appl. Chem.* **1968,** *2* (8), 1441-1455.

107. Wang, J.; Wen, Y.; Feng, X.; Song, Y.; Jiang, L., *Macromol. Rapid Commun.* **2006,** *27* (3), 188-192.

108. Feng, X.; Zhai, J.; Jiang, L., *Angew. Chem. Int. Ed.* **2005,** *44* (32), 5115-5118.

109. Lim, H. S.; Kwak, D.; Lee, D. Y.; Lee, S. G.; Cho, K., *J. Am. Chem. Soc.* **2007,** *129* (14), 4128-4129.

110. Lim, H. S.; Han, J. T.; Kwak, D.; Jin, M.; Cho, K., *J. Am. Chem. Soc.* **2006,** *128* (45), 14458-14459.

111. Feng, L.; Song, Y.; Zhai, J.; Liu, B.; Xu, J.; Jiang, L.; Zhu, D., *Angew. Chem. Int. Ed.* **2003,** *42* (7), 800-802.

112. Abdelsalam, M. E.; Bartlett, P. N.; Kelf, T.; Baumberg, J., *Langmuir* **2005,** *21* (5), 1753-1757.

113. Han, J. T.; Xu; Cho, K., *Langmuir* **2005,** *21* (15), 6662-6665.

114. Papon, A.; Montes, H.; Lequeux, F.; Oberdisse, J.; Saalwachter, K.; Guy, L., *Soft Matter* **2012,** *8* (15), 4090-4096.

115. Kutnyanszky, E.; Vancso, G. J., *Eur. Polym. J.* **2012,** *48* (1), 8-15.

116. Melzak, K. A.; Mateescu, A.; Toca-Herrera, J. L.; Jonas, U., *Langmuir* **2012,** *28* (35), 12871-12878.

117. Li, A.; Ramakrishna, S. N.; Schwarz, T.; Benetti, E. M.; Spencer, N. D., *ACS Appl. Mater. Interfaces* **2013,** *5* (11), 4913-4920.

118. Li, D.; Sheng, X.; Zhao, B., *J. Am. Chem. Soc.* **2005,** *127* (17), 6248-6256.

119. Nath, N.; Chilkoti, A., *J. Am. Chem. Soc.* **2001,** *123* (34), 8197-8202.

120. Cao, Y.; Liu, N.; Fu, C.; Li, K.; Tao, L.; Feng, L.; Wei, Y., *ACS Appl. Mater. Interfaces* **2014,** *6* (3), 2026-2030.

121. Gao, S. J.; Shi, Z.; Zhang, W. B.; Zhang, F.; Jin, J., *ACS Nano* **2014,** *8* (6), 6344-6352.

122. Svetushkina, E.; Puretskiy, N.; Ionov, L.; Stamm, M.; Synytska, A., *Soft Matter* **2011,** *7* (12), 5691-5696.

123. Wang, W.; Vaughn, M. W., *Scanning* **2008,** *30* (2), 65-77.

124. White, L. D.; Tripp, C. P., *J. Colloid Interface Sci.* **2000,** *232* (2), 400-407.

125. Tadmor, R., *Langmuir* **2004,** *20* (18), 7659-7664.

126. Young, T., *Philos. Trans. R. Soc. London* **1805,** *95*, 65-87.

127. Extrand, C. W., *Langmuir* **2002,** *18* (21), 7991-7999.

128. Sun, T.; Wang, G.; Feng, L.; Liu, B.; Ma, Y.; Jiang, L.; Zhu, D., *Angew. Chem. Int. Ed.* **2004,** *43* (3), 357-360.

129. Blanco-Gomez, G.; Flendrig, L. M.; Cooper, J. M., *Langmuir* **2010,** *26* (10), 7248-7253.

130. Erbil, H. Y.; Demirel, A. L.; Avcı, Y.; Mert, O., *Science* **2003,** *299* (5611), 1377-1380.

131. Wolansky, G.; Marmur, A., *Colloids Surf. Physicochem. Eng. Aspects* **1999,** *156* (1–3), 381-388.

132. de Gennes, P. G., *Rev. Mod. Phys.* **1985,** *57* (3), 827-863.

133. Binnig, G.; Quate, C. F.; Gerber, C., *Phys. Rev. Lett.* **1986,** *56* (9), 930-933.

134. Bakshi, M. S.; Kaura, A.; Miller, J. D.; Paruchuri, V. K., *J. Colloid Interface Sci.* **2004,** *278* (2), 472-477.

135. Green, C. P.; Lioe, H.; Cleveland, J. P.; Proksch, R.; Mulvaney, P.; Sader, J. E., *Rev. Sci. Instrum.* **2004,** *75* (6), 1988-1996.

136. Reifenberger, R. Introduction to Contact Mechanics. <http://nanohub.org/resources/9820/download/> (accessed 9/30/2014).

137. Neto, C.; Craig, V. S. J., *Langmuir* **2001,** *17* (7), 2097-2099.

138. Zhu, D.; Li, X.; Zhang, G.; Zhang, X.; Zhang, X.; Wang, T.; Yang, B., *Langmuir* **2010,** *26* (17), 14276-14283.

139. Li, A.; Ramakrishna, S. N.; Kooij, E. S.; Espinosa-Marzal, R. M.; Spencer, N. D., *Soft Matter* **2012,** *8* (35), 9092-9100.

140. Cho, E. C.; Kim, Y. D.; Cho, K., *Polymer* **2004,** *45* (10), 3195-3204.

141. Ishida, N.; Biggs, S., *Macromolecules* **2007,** *40* (25), 9045-9052.

142. Murakami, D.; Kobayashi, M.; Moriwaki, T.; Ikemoto, Y.; Jinnai, H.; Takahara, A., *Langmuir* **2013,** *29* (4), 1148-1151.

143. Lee, S. G.; Pascal, T. A.; Koh, W.; Brunello, G. F.; Goddard, W. A.; Jang, S. S., *J. Phys. Chem. C* **2012,** *116* (30), 15974-15985.

144. Li, A.; Benetti, E. M.; Tranchida, D.; Clasohm, J. N.; Schönherr, H.; Spencer, N. D., *Macromolecules* **2011,** *44* (13), 5344-5351.

145. Liu, G.; Zhang, G., *J. Phys. Chem. B* **2004,** *109* (2), 743-747.

146. Shannon, M. A.; Bohn, P. W.; Elimelech, M.; Georgiadis, J. G.; Marinas, B. J.; Mayes, A. M., *Nature* **2008,** *452* (7185), 301-310.

147. Gao, C.; Sun, Z.; Li, K.; Chen, Y.; Cao, Y.; Zhang, S.; Feng, L., *Energy Environ. Sci.* **2013,** *6* (4), 1147-1151.

148. Nguyen, D. D.; Tai, N.-H.; Lee, S.-B.; Kuo, W.-S., *Energy Environ. Sci.* **2012,** *5* (7), 7908-7912.

149. Gao, Y.; Zhou, Y. S.; Xiong, W.; Wang, M.; Fan, L.; Rabiee-Golgir, H.; Jiang, L.; Hou, W.; Huang, X.; Jiang, L.; Silvain, J.-F.; Lu, Y. F., *ACS Appl. Mater. Interfaces* **2014,** *6* (8), 5924-5929.

150. Bi, H.; Xie, X.; Yin, K.; Zhou, Y.; Wan, S.; He, L.; Xu, F.; Banhart, F.; Sun, L.; Ruoff, R. S., *Adv. Funct. Mater.* **2012,** *22* (21), 4421-4425.

151. White, H. K.; Lyons, S. L.; Harrison, S. J.; Findley, D. M.; Liu, Y.; Kujawinski, E. B., *Environ. Sci. Technol.* **2014,** *1* (7), 295-299.

152. Dong, Y.; Li, J.; Shi, L.; Wang, X.; Guo, Z.; Liu, W., *Chem. Commun.* **2014,** *50* (42), 5586-5589.

153. Feng, L.; Zhang, Z.; Mai, Z.; Ma, Y.; Liu, B.; Jiang, L.; Zhu, D., *Angew. Chem.* **2004,** *116* (15), 2046-2048.

154. Cheryan, M.; Rajagopalan, N., *J. Membr. Sci.* **1998,** *151* (1), 13-28.

155. Kota, A. K.; Kwon, G.; Choi, W.; Mabry, J. M.; Tuteja, A., *Nat. Commun.* **2012,** *3*, 1-8.

156. Zhu, Q.; Tao, F.; Pan, Q., *ACS Appl. Mater. Interfaces* **2010,** *2* (11), 3141-3146.

157. Zhang, L. B.; Zhang, Z. H.; Wang, P., *NPG Asia Mater.* **2012,** *4*, 8.

158. Brugger, B.; Richtering, W., *Adv. Mater.* **2007,** *19* (19), 2973-2978.

159. Li, A.; Sun, H.-X.; Tan, D.-Z.; Fan, W.-J.; Wen, S.-H.; Qing, X.-J.; Li, G.-X.; Li, S.-Y.; Deng, W.-Q., *Energy Environ. Sci.* **2011,** *4* (6), 2062-2065.

160. Hlavacek, M., *J. Membr. Sci.* **1995,** *102* (0), 1-7.

161. Xue, Z.; Wang, S.; Lin, L.; Chen, L.; Liu, M.; Feng, L.; Jiang, L., *Adv. Mater.* **2011,** *23* (37), 4270-4273.

162. Crick, C. R.; Gibbins, J. A.; Parkin, I. P., *J. Mater. Chem.* **2013,** *1* (19), 5943-5948.

163. Zhou, X.; Zhang, Z.; Xu, X.; Guo, F.; Zhu, X.; Men, X.; Ge, B., *ACS Appl. Mater. Interfaces* **2013,** *5* (15), 7208-7214.

164. Lin, L.; Liu, M.; Chen, L.; Chen, P.; Ma, J.; Han, D.; Jiang, L., *Adv. Mater.* **2010,** *22* (43), 4826-4830.

165. Jung, Y. C.; Bhushan, B., *Langmuir* **2009,** *25* (24), 14165-14173.

166. Kwon, G.; Kota, A. K.; Li, Y.; Sohani, A.; Mabry, J. M.; Tuteja, A., *Adv. Mater.* **2012,** *24* (27), 3666-3671.

167. Zhang, S.; Lu, F.; Tao, L.; Liu, N.; Gao, C.; Feng, L.; Wei, Y., *ACS Appl. Mater. Interfaces* **2013,** *5* (22), 11971-11976.

168. Liu, N.; Cao, Y.; Lin, X.; Chen, Y.; Feng, L.; Wei, Y., *ACS Appl. Mater. Interfaces* **2014,** *6* (15), 12821–12826.

169. Mates, J. E.; Schutzius, T. M.; Qin, J.; Waldroup, D. E.; Megaridis, C. M., *ACS Appl. Mater. Interfaces* **2014,** *6* (15), 12837–12843.

170. Ebara, M.; Hoffman, J. M.; Hoffman, A. S.; Stayton, P. S.; Lai, J. J., *Langmuir* **2013,** *29* (18), 5388-5393.

171. Cole, M. A.; Voelcker, N. H.; Thissen, H.; Horn, R. G.; Griesser, H. J., *Soft Matter* **2010,** *6* (12), 2657-2667.

172. Riskin, M.; Tel-Vered, R.; Willner, I., *Adv. Funct. Mater.* **2009,** *19* (15), 2474-2480.

173. Rubio-Retama, J.; Zafeiropoulos, N. E.; Serafinelli, C.; Rojas-Reyna, R.; Voit, B.; Lopez Cabarcos, E.; Stamm, M., *Langmuir* **2007,** *23* (20), 10280-10285.

174. Zhao, X.; Ding, X.; Deng, Z.; Zheng, Z.; Peng, Y.; Tian, C.; Long, X., *New J. Chem.* **2006,** *30* (6), 915-920.

175. Li, Z.; Geisel, K.; Richtering, W.; Ngai, T., *Soft Matter* **2013,** *9* (41), 9939-9946.

176. Li, Z.; Richtering, W.; Ngai, T., *Soft Matter* **2014,** *10*, 6182-6191.

177. Schepelina, O.; Zharov, I., *Langmuir* **2007,** *23* (25), 12704-12709.

178. Alem, H.; Duwez, A.-S.; Lussis, P.; Lipnik, P.; Jonas, A. M.; Demoustier-Champagne, S., *J. Membr. Sci.* **2008,** *308* (1–2), 75-86.

179. Liao, K.-S.; Wan, A.; Batteas, J. D.; Bergbreiter, D. E., *Langmuir* **2008,** *24* (8), 4245-4253.

180. Brady, M. A.; Limpoco, F. T.; Perry, S. S., *Langmuir* **2009,** *25* (13), 7443-7449.

181. Tsujii, Y.; Nomura, A.; Okayasu, K.; Gao, W.; Ohno, K.; Fukuda, T., *J. Phys.: Conf. Ser.* **2009,** *184* (1), 012031-012037.

182. Mukae, K.; Sakurai, M.; Sawamura, S.; Makino, K.; Kim, S. W.; Ueda, I.; Shirahama, K., *J. Phys. Chem.* **1993,** *97* (3), 737-741.

183. Zhu, P. W.; Napper, D. H., *J. Colloid Interface Sci.* **1996,** *177* (2), 343-352.

184. Fu, H.; Policarpio, D. M.; Batteas, J. D.; Bergbreiter, D. E., *Polym. Chem.* **2010,** *1* (5), 631-633.

185. Jochum, F. D.; Theato, P., *Chem. Soc. Rev.* **2013,** *42*, 7468-7483.

186. Schattling, P.; Jochum, F. D.; Theato, P., *Chem. Commun.* **2011,** *47* (31), 8859-8861.

187. Schattling, P.; Jochum, F. D.; Theato, P., *Polym. Chem.* **2014,** *5* (1), 25-36.

188. Maharjan, P.; Woonton, B. W.; Bennett, L. E.; Smithers, G. W.; DeSilva, K.; Hearn, M. T. W., *Innov. Food Sci. Emerg. Technol.* **2008,** *9* (2), 232-242.

189. Dierendonck, M.; De Koker, S.; De Rycke, R.; De Geest, B. G., *Soft Matter* **2014,** *10* (6), 804-807.

190. Li, J.; Jing, Z.; Zha, F.; Yang, Y.; Wang, Q.; Lei, Z., *ACS Appl. Mater. Interfaces* **2014,** *6* (11), 8868–8877.

191. *Handbook of Heterogeneous Catalysis*. 2 ed.; Wiley: Hoboken, NJ, **2008**.

192. Langmuir, I., *J. Am. Chem. Soc.* **1918,** *40* (9), 1361-1403.

193. Freund, H. J.; Kuhlenbeck, H.; Libuda, J.; Rupprechter, G.; Bäumer, M.; Hamann, H., *Top. Catal.* **2001,** *15* (2-4), 201-209.

194. Davis, B., *Top. Catal.* **2005,** *32* (3-4), 143-168.

195. Stranges, A. N., *Stud. Surf. Sci. Catal.* **2007,** *163*, 1-27.

196. Van Der Laan, G. P.; Beenackers, A. A. C. M., *Cat. Rev.* **1999,** *41* (3-4), 255-318.

197. Steynberg, A. P.; Dry, M. E.; Davis, B. H.; Breman, B. B., Chapter 2 - Fischer-Tropsch Reactors. In *Stud. Surf. Sci. Catal.*, André, S.; Mark, D., Eds. Elsevier: Philadelphia, PA, **2004;** Vol. 152, pp 64-195.

198. Reuel, R. C.; Bartholomew, C. H., *J. Catal.* **1984,** *85* (1), 78-88.

199. Barbier, A.; Tuel, A.; Arcon, I.; Kodre, A.; Martin, G. A., *J. Catal.* **2001,** *200* (1), 106-116.

200. Bezemer, G. L.; Bitter, J. H.; Kuipers, H. P. C. E.; Oosterbeek, H.; Holewijn, J. E.; Xu, X.; Kapteijn, F.; Van Diilen, A. J.; De Jong, K. P., *J. Am. Chem. Soc.* **2006,** *128* (12), 3956-3964.

201. Borg, Ø.; Dietzel, P. D. C.; Spjelkavik, A. I.; Tveten, E. Z.; Walmsley, J. C.; Diplas, S.; Eri, S.; Holmen, A.; Rytter, E., *J. Catal.* **2008,** *259* (2), 161-164.

202. Ho, S. W.; Houalla, M.; Hercules, D. M., *J. Phys. Chem.* **1990,** *94* (16), 6396-6399.

203. Khodakov, A. Y.; Griboval-Constant, A.; Bechara, R.; Zholobenko, V. L., *J. Catal.* **2002,** *206* (2), 230-241.

204. Moreno-Castilla, C.; Carrasco-Marin, F., *J. Chem. Soc., Faraday Trans.* **1995,** *91* (19), 3519-3524.

205. Ribeiro, F. H.; Schach Von Wittenau, A. E.; Bartholomew, C. H.; Somorjai, G. A., *Cat. Rev.* **1997,** *39* (1-2), 49-76.

206. Khodakov, A. Y.; Chu, W.; Fongarland, P., *Chem. Rev.* **2007,** *107* (5), 1692-1744.

207. Wang, Z.; Skiles, S.; Yang, F.; Yan, Z.; Goodman, D. W., *Catal. Today* **2012,** *181* (1), 75-81.

208. Bechara, R.; Balloy, D.; Vanhove, D., *Appl. Catal., A* **2001,** *207* (1–2), 343-353.

209. Campbell, C. T., *Annu. Rev. Phys. Chem.* **1990,** *41* (1), 775-837.

210. Lambert, S.; Ferauche, F.; Brasseur, A.; Pirard, J.-P.; Heinrichs, B., *Catal. Today* **2005,** *100* (3-4), 283-289.

211. Lopez, N.; Nørskov, J. K., *Surf. Sci.* **2001,** *477* (1), 59-75.

212. Zhao, H.; Koel, B. E., *J. Catal.* **2005,** *234* (1), 24-32.

213. Marković, N. M.; Schmidt, T. J.; Stamenković, V.; Ross, P. N., *Fuel Cells* **2001,** *1* (2), 105-116.

214. Anderson, J. A.; Fernández-García, M.; Haller, G. L., *J. Catal.* **1996,** *164* (2), 477-483.

215. Choi, K. I.; Vannice, M. A., *J. Catal.* **1991,** *131* (1), 36-50.

216. Choudhary, T. V.; Sivadinarayana, C.; Datye, A. K.; Kumar, D.; Goodman, D. W., *Catal. Lett.* **2003,** *86* (1-3), 1-8.

217. Crathorne, E. A.; Macgowan, D.; Morris, S. R.; Rawlinson, A. P., *J. Catal.* **1994,** *149* (2), 254-267.

218. Illas, F.; López, N.; Ricart, J. M.; Clotet, A.; Conesa, J. C.; Fernández-García, M., *J. Phys. Chem. B* **1998,** *102* (41), 8017-8023.

219. Newton, M. A.; Francis, S. M.; Li, Y.; Law, D.; Bowker, M., *Surf. Sci.* **1991,** *259* (1-2), 45-55.

220. Rainer, D.; Corneille, J. S.; Goodman, D. W., *J. Vac. Sci. Technol.* **1995,** *13*, 1595-1599.

221. Luo, K. Dissertation, Texas A&M University, **2006**.

222. Overbury, S. H.; Bertrand, P. A.; Somorjai, G. A., *Chem. Rev.* **1975,** *75* (5), 547-560.

223. Mezey, L. Z.; Giber, J., *Jpn. J. Appl. Phys.* **1982,** *21* (11), 1569-1571.

224. Park, Y. H.; Price, G. L., *Ind. Eng. Chem. Res.* **1992,** *31* (2), 469-474.

225. Phillips, J.; Auroux, A.; Bergeret, G.; Massardier, J.; Renouprez, A., *J. Phys. Chem.* **1993,** *97* (14), 3565-3570.

226. Zhang, Q.; Li, J.; Liu, X.; Zhu, Q., *Appl. Catal., A* **2000,** *197* (2), 221-228.

227. Studt, F.; Abild-Pedersen, F.; Bligaard, T.; Sørensen, R. Z.; Christensen, C. H.; Nørskov, J. K., *Science* **2008,** *320* (5881), 1320-1322.

228. Kim, S. K.; Lee, J. H.; Ahn, I. Y.; Kim, W.-J.; Moon, S. H., *Appl. Catal., A* **2011,** *401* (1–2), 12-19.

229. Liao, K.-S.; Fu, H.; Wan, A.; Batteas, J. D.; Bergbreiter, D. E., *Langmuir* **2008,** *25* (1), 26-28.

230. Bergbreiter, D. E.; Simanek, E. E.; Owsik, I., *J. Polym. Sci., Part A: Polym. Chem.* **2005,** *43* (19), 4654-4665.

APPENDIX

Experimental Procedures

Materials

N-isopropylacrylamide was purchased from Sigma-Aldrich and recrystallized from 9:1 hexanes/benzene. 3-Aminopropyltriethoxysilane was obtained from Alfa Aesar and used as received. Polyethylenimine (PEI, branched, Mw = 25000), isopropylamine, 10 nm silica nanoparticles, and hexadecane were purchased from Sigma-Aldrich and used as received. The 100 nm silica nanoparticles were obtained from Fiber Optic Center Inc. Medium porosity (pore size 10-20 μm) glass frits were obtained from ACE Glass (ACE # 5848-33). Using reported procedures poly(*N*-acryloxysuccinimide) (PNASI) and poly(*N*-isopropylacrylamide)-*c*-poly(*N*-acryloxysuccinimide) (PNIPAM-*c*-PNASI) used for surface grafting were prepared from *N*-acryloxysuccinimide and *N*-isopropylacrylamide.[30, 65, 229] A Barnstead Nanopure Diamond water purification system was used to obtain high-purity water with low conductivity (18.2 MΩ•cm). All salts used for the simulated ocean water were ACS grade or higher and were used as received.

Synthesis of N-acryloxysuccinimide (NASI)

A solution of *N*-hydroxysuccinimide (10.0g, 87 mmol), dichloromethane (130 mL), and triethylamine (12 mL, 90 mmol) was prepared at 0°C. To this solution acryloyl chloride (7.5 mL, 92 mmol) was added drop wise over a 20 min time period then stirred

at room temperature for an additional 60 minutes. The resulting salt was removed by filtration. The filtrate was washed with cold water (160 mL) and cold brine (160 mL) then concentrated under reduced pressure. The concentrate was cooled to 0°C overnight. The monomer was precipitated in a solution of hexanes and ethyl acetate (6:1). The monomer was then captured by filtration and dried under vacuum overnight to yield a white powder. ^{1}H NMR ($CDCl_3$, 300 MHz) δ 1.60 (s, 2H), 2.87 (s, 4H), 6.18 (d, J=17 Hz, 1H), 6.33 (m, 1H), 6.71 (d, J=17 Hz, 1H).

Synthesis of poly(N-acryloxysuccinimide) (PNASI)

NASI (10.0g, 59 mmol) and 2,2'-azoisobutyronitrile (AIBN) (25 mg, 0.15 mmol) was dissolved in benzene (300 mL) stirring under N_2. The solution was degassed by two cycles of freeze-pump-thaw. The resulting solution was refluxed in an oil bath at 80°C for 12 h. The polymer was collected by filtration and dried overnight under vacuum yielding a white powder. ^{1}H NMR (DMSO-d_6, 300 MHz) δ 2.05 (bs, 2H), 2.80 (bs, 4H), 3.13 (bs, 1H).

Synthesis of poly(N-isopropylacrylamide-c-N-acryloxysuccinimide) (PNIPAM-c-PNASI)

N-isopropylacrylamide (NIPAM, 3.6g, 32 mmol), NASI (0.6g, 3.5 mmol), and AIBN (26.2 mg, 1.6 mmol) were dissolved in benzene (200 mL). The solution was degassed by two cycles of freeze-pump-thaw. The resulting solution was refluxed at 80°C for 12 h. The solution was concentrated under reduced pressure, then dissolved in tetrahydrofuran (THF). The polymer was precipitated by dropwise addition to stirring

ethyl ether and collected by filtration. The polymer was dried overnight under vacuum yielding a white powder. The product was analyzed by ^{1}H NMR spectroscopy to determine the ratio of PNIPAM-*c*-PNASI to be 9:1.

Synthesis of aminated nanoparticles

The 10 or 100 nm silica nanoparticles (2.5g) were cleaned by shaking overnight in a 5% hydrochloric acid solution (50 mL). The suspension was centrifuged and the supernatant was decanted to recover the nanoparticles. The particles were rinsed twice by suspending (once in water and once in methanol), centrifuged, and collected. The cleaned nanoparticles were dried overnight under vacuum. A published procedure was used to aminate the silica nanoparticles.[230] A solution of 3-aminopropyltriethoxysilane (APTES, 10 mL, 47 mmol) in toluene (100 mL) was prepared to which the cleaned dried silica nanoparticles were added. The solution was refluxed overnight at 120ºC. The nanoparticles were recovered from the cooled solution via centrifugation. The particles were washed twice by suspension in methanol then centrifugation. The recovered particles were dried overnight under vacuum.

Titration of aminated silica nanoparticles

The amine loading of the functionalized silica nanoparticles was determined by reaction of the amine with hydrochloric acid then back titration with sodium hydroxide. The aminated silica nanoparticles (100 mg) were shaken in 10 mL of standardized 0.01 M

HCl for 3 hours. After centrifugation an aliquot of the supernatant was titrated with standardized 0.01 M NaOH until the phenolphthalein endpoint was reached.

Functionalization by Covalent Layer-by-Layer Assembly

The functionalization of the silica wafer and glass frits was completed following a pre-established procedure.[30, 65, 229] The polymer solutions used for the layer-by-layer assembly were all made in DMF and dissolved using a wrist action shaker. The following solutions were made: 0.5% wt. PEI, 16% wt. PNASI, and 20% wt. PNIPAM-*c*-PNASI. The suspension of aminated silica nanoparticles (1 % wt) included triethylamine (0.5% vol) in DMF. The nanoparticle suspension was sonicated for at least 30 minutes before the first use and a minimum of 5 minutes before each subsequent use. To begin functionalization the silica wafer was first cleaned by sonication for 5 minutes in the following series of solvents: hexanes, ethanol, acetone, and purified water. The wafer was further cleaned in an acid piranha solution (3:1 v/v, 96% H_2SO_4: 30% H_2O_2) for 4 hours at room temperature. After the piranha treatment, the wafer was copiously rinsed with purified water and ethanol, then added to a solution of APTES (25 µL, 0.1 mmol) in ethanol and shaken overnight. The wafer was then dried in vacuum at 120°C for 3 hours. The APTES functionalized wafer was then submerged in the PNASI polymer solution and shaken overnight. After each functionalization step the wafer was removed from a solution and it was washed 3 times by shaking in DMF for approximately 3 minutes. The washed wafer was then submerged in the PEI solution and shaken for 30 minutes. After rinsing the wafer was placed in a solution of isopropylamine (2.5% vol, in DMF) for 30

minutes. This cycle involving the three solutions PNASI, PEI, and isopropylamine was then repeated with the PNASI time reduced to 30 minutes. The next cycle included these three solutions, PNIPAM-*c*-PNASI, silica nanoparticles, and isopropylamine. This cycle was repeated 7 times with only slight modifications; for the first 5 cycles the nanoparticle solution contained both the 10 and 100 nm particles, for the sixth cycle the nanoparticle solution contained only 10 nm particles, and for the final cycle the nanoparticle solution was omitted. Upon completion of the assembly process the silica wafer was copiously washed with pure water and methanol, then dried with nitrogen gas.

The functionalization of the glass frits followed the same procedure with a few slight modifications. For the entire process following the acid piranha step the frits were housed in a Teflon holder to allow for functionalization of both sides and to prevent chipping of the frit. The initial reaction time with PNASI was increased to 24 hours. Each washing step between solutions was increased to three rinses of 10 minutes each in DMF. The functionalized frits were shaken three times in a water bath then fitted into a Teflon chromatography column to tubing adapter (ACE #5838-91) which was secured to a 15 mm i.d. column (ACE #7644-15). Once in the chromatography column, the frits were washed by passing ~50 mL of water and ~30 mL of methanol through the frit and then were dried under flowing nitrogen overnight.